Investigations of Nanoscale Variations in Spin and Charge Transport in Manganites and Organic Semiconductors using Spin Polarized Scanning Tunneling Spectroscopy

Thesis by

Cameron Richard Hughes

In Partial Fulfillment of the Requirements

for the Degree of

Doctor of Philosophy

California Institute of Technology

Pasadena, California

2010

(Defended January 29th, 2010)

To friends and family.

Acknowledgements

It will come to no surprise to anyone who has finished a Ph. D. thesis that I owe much of my success to the friends, mentors, and family members that have nurtured me scientifically and supported me as a person. Let me humbley begin by regretting that I will inevitably leave out many without which this thesis would have been impossible. First and foremost, I must thank Professor Nai-Chang Yeh, who provided much more that just the laboratory space and equipment to perform my experiments. Her high standards of excellence for all stages of the research process, from the initial proposal to final presentation of results to the research community, have been a great source of learning, and have given me an example that I hope to carry with me through the rest of my career. She has also shown tremendous patience and acceptance of the occasional failures without casting blame while retaining the perspective and optimism necessary to carry out such challenging research. I also have always been impressed with her as a person for the caring she shows for the well-being and honorable treatment of not just members of her lab group, but the greater scientific community as well.

My fellow co-workers also deserve thanks for teaching me so many of my research skills and also for providing diversion and perspective when I took the inevitable failures too hard. I entered the Yeh group with Andrew Beyer, and though our initial collaborations were not as successful as we hoped, I always appreciated his unflappable devotion to making the experiment a success and understated sense of humor, particularily during some trying trips to the National Magnet Lab in Tallahassee. I wish he and his wife Meredith the best of luck in the future with their now growing family. Ching-tzu Chen was my initial graduate student mentor, who showed me the essential skill of how to diagnose and troubleshoot research problems in a logical and scientific manner. I also cherished finding a kindred spirit with an intellectual curiosity in all things, and a ready acceptor of

my baked goods. Slobodan Mitrovic's time as a postdoctoral researcher in our group was important in teaching me to keep perspective in the research process, to not focus on conquering experimental difficulties at the expense of overall progress in the project, to simplify and elucidate my message when presenting my research, and to keep the future in mind. In addition, he was an able pastry critic and baker in his own right. Finally, I regret that I only really began to know Marcus Teague late in my graduate career, as I found his technical excellence and detail-oriented nature a great help in the spin-polarized tunneling experiments in particular. His dark sense of humor, ready opinions on all matters whether requested or not, and similar realistic outlook on life were also a huge comfort. I wish them all great success and happiness in the future.

Many people at Caltech played smaller but no less critical roles in helping me. Nils Asplund was a tremendous help in machining and designing all manner of instruments, and was good company in morning in the the almost empty labs. Matt Dicken, William Chueh, and Imogen Pryce were all very professional and a joy to work with in sharing the maintainance of the Pulsed Laser Deposition system in Professor Harry Atwater's and KNI's labs. Bruce Brunschwig abley maintained the equipment at the MMRC, and was always ready to help in case of crisis. Terry Scott showed me how to run a lathe and milling machine without hurting myself, and he and Isaac, Ramon, Jose, Mark, Bovan, and Rick at the Physics Machine Shop were able teachers and great company during the 3 months I spent there crafting the components for my STM head. Hsin-Ying Chiu, Hareem Maune, and Jinseung Heo were extremely helpful and knowledgeable about carbon nanotubes, deposition techniques, and AFM in my brief time working with them in Professor Marc Bockrath's lab. Jing Shi was my first official summer undergradute graduate, and she impressed me with her work ethic and excellent questions. Finally, my thanks to Professor Harry Atwater and Professor Marc Bockrath for allowing me to use their equipment and lab space.

The friends I have made at Caltech over my 7 years at Caltech have brought me tremendous joy, and have helped make my life outside the lab worth living. These include Andrew and Meredith Beyer, Christie Canaria, Brad Cenko, Ching-Tzu Chen, Hsin-Ying Chiu, Ted Corcovolis, Matt Eichenfield, Nima Ghaderi, James and Keiko Maloney, Hareem Maune, Thomas Miller the 3rd and

Nicola Wilkins-Miller, Slobodan Mitrovic, April and Evan Neildholt, Marie-Helene Rousseau, Jack and Lindsay Sayers, Robert Ward, and Alan and all the good folks at Le Petit Vendome wine bar.

Special thanks to my family; my mother Noreen, my father Richard, and my brother Graham. They comforted me during my most trying times in graduate school, and I will love them always.

Abstract

Spintronics is a new class of spin-dependent electronics with great potential for nonvolatile memory and logic technology. Additionally, spintronics may be combined with optoelectronic applications to achieve higher efficiency and novel capabilities. All of these developments require growth and characterization of new materials to polarize and transport electron spin currents. In this context, spin-polarized and non spin-polarized spatially resolved conductance measurements performed by scanning tunneling microscopy (STM) are effective means to investigate the spin and charge quantum transport in magnetic and organic systems, particularly for systems that are prone to phase separations and complex magnetic properties, such as the colossal magnetoresistive (CMR) manganites $La_{1-x}Ca_xMnO_3$ (LCMO) that are known to exhibit intrinsic electronic heterogeneity due to strong electronic correlation and competing orders in the ground state. Additionally, STM measurements can provide direct information about the band structure and mobility of the organic semiconductor 8-hydroxyquinoline aluminum (Alq_3) in the Alq_3/LCMO heterostructures to further understand their performance in spintronic devices.

The manganite compound $La_{1-x}Ca_xMnO_3$ (LCMO) with a bulk doping level x = 0.3 is a ferromagnetic metal with a relatively high Curie temperature T_c = 270K. This system is promising for spintronic device applications, and may be used as a spin current injector because of the gapped band structure for minority spins, a property known as half-metallicity. On the other hand, even in this bulk ferromagnetic metallic phase, inherent electronic inhomogeneity at microscopic scales is expected. To further study this effect, we have investigated x = 0.3 LCMO thin films using scanning tunneling microscopy in spectroscopic mode under varied temperature, magnetic field and spin polarization of the tunneling current. Spatially resolved maps of tunneling conductance taken

with non polarized Pt/Ir tip show variations on the scale of a few hundred nanometers in size in the bulk ferromagnetic state, which are believed to be the result of intrinsic inhomogeneity of the manganites due to their tendency toward phase separation. Maps of tunneling conductance taken with spin-polarized Cr coated tips are consistent with the convolution of the LCMO and Cr density of states, and below the T_c of LCMO the spin-polarized tunnel junction can be described as a spin valve configuration. The electronic homogeneity in the material increases above the magnetic ordering temperature, or with application of magnetic field in the bulk ferromagnetic state. We identified gaps in the conductance at two separate characteristic energies. The first gap of energy approximately 0.6 eV is believed to arise from a ferromagnetic insulator (FI) surface phase due to its disappearance above the Curie temperature (T_c) and the dependence of gap energy on relative tip and sample magnetic orientation. The surface phase may be stabilized by Ca deficiency at the LCMO surface, corroborated by x-ray photoemission spectroscopy (XPS). Second, we observe a nearly temperature independent and spatially varying gap of approximately 0.4 eV for all zero-field tunneling spectra, which is believed to be associated with the psuedogap (PG) phenomena in the manganites. Application of a magnetic field converts the regions of PG phenomena to FI, in conjunction with an increase in the homogeneity of the film conductance. These findings suggest that the PG phenomena arise from electronic inhomogeneity in the manganite film, in agreement with theoretical investigations, and that the vertical and lateral electronic inhomogeneity, along with its dependence on temperature and applied magnetic field, has important implications for use of these materials in high-density nanoscale spintronic devices.

We have also successfully deposited and investigated Alq_3/LCMO heterostructures of varying thicknesses to investigate charge transport in Alq_3. Bulk Alq_3 structural properties are preserved down to 10 nm in thickness with a -0.3 eV offset in band energies. The lack of band bending between LCMO and Alq_3 is suggestive of a shift in the preferred isomer from meridinial to facial at the interface. The absence of polaron states from our STM studies implies the relative unimportance of polarons in Alq_3 for this heterostructure. In addition, the measured mobilities on the order of $10^{-5}\text{cm}^2(\text{Vs})^{-1}$ for electrons and holes in Alq_3 films deposited on heated LCMO substrates

more closely resemble values of the intrinsic mobility estimated from the muon spin relaxation measurements than those from studies of the bulk LED structures, suggesting that superior film conductivity close to the fundamental limit is possible with a heated substrate during sublimation.

Contents

List of Figures

Chapter 1

Introduction

Semiconductor technology has shown remarkedly consistent progress in miniaturizing the device size in electronic circuits since the industry's inception. Intel founder Gordon Moore first quantified this trend in 1965 [1], eventually predicting a doubling of device density every 20 months, which has held remarkedly constant over more than 40 years. These advances have been driven by improvements in lithographic techniques allowing patterning of smaller scale structures in silicon, with IBM in 2006 demonstrating 29.9 nm wide circuitry using deep ultraviolet optical lithography [2]. Unfortunately, Moore's law will not hold indefinitely with silicon as the base technology, due to the finite limitation in lithographic device patterning and the additional consideration of exponentially increasing power consumption.

To continue the current rate of progress, new technologies are necessary either to integrate with silicon and extend the horizon of technological performance, or replace the material completely. Spintronics, or electronics that manipulates and reads electron spins to store information, is particularily advantageous for memory storage due to fast read and write times, high endurance switching, and non-volatility, as well as the ease with which it can integrate with existing silicon devices [3]. The fundamental change from information stored in the electron charge to electron spin necessitates a new class of materials that can adequately inject, transport, and detect electron-spin orientation. A ferromagnetic semiconductor would be the ideal material as it would greatly simplify generation of a spin-polarized current, as well as integration with other semiconducting materials. Unfortunately, no suitable canidates have surfaced with a temperature of onset of ferromagnestism (Curie

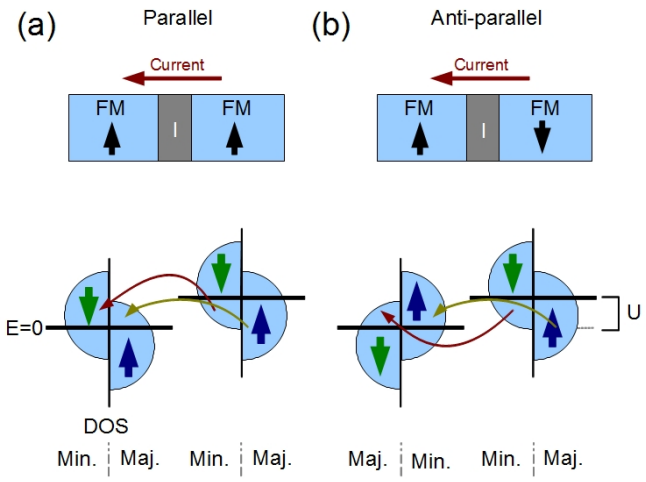

Figure 1.1: Density of states (DOS) vs energy of two Stoner ferromagnetic layers separated by a semiconducting barrier in a spin valve device in the parallel orientation (a) and antiparallel (b). The net current between the two upon application of a constant bias voltage is lower in the antiparallel case due to mismatch of the spin density of states, and results in a higher resistance of the structure.

temperature T_c) comparable to ambient temperature, with diluted magnetic semiconductors such as $Ga_{1-x}Mn_xAs$ among the most promising with T_c of 110K and higher [4].

An alternative strategy is to use ferromagnetic metals to inject or detect a spin-polarized current into a semiconducting transport layer, and considerable effort has focused on developing these structures. The principle component in this approach to spintronics consists of two ferromagnetic layers separated by an insulating or semiconducting spacer layer, labeled a magnetic tunnel junction (MTJ) in the first case and a spin valve in the second. The operation of each device is similar, in that due to the unequal population of electrons in the spin up and spin down orientation in each of the ferromagnets, the electrical resistance between the two is dependent on the relative magnetic orientation of both materials (Figure 1.1). The layers are engineered with differing magnetic fields necessary to align the magnetic domains in order to use an applied magnetic field to independently control the magnetic orientation of each layer. This allows switching the relative orientation of the two magnetic domains between parallel and antiparallel to represent the 1 and 0 of a computer memory bit. Integral to the efficiency of the spin valve and MTJ devices is a high degree of spin polarization in the magnetic electrodes, as the change in device resistance is dependent on the difference between the spin-up and spin-down density of states. The ideal material in this respect is

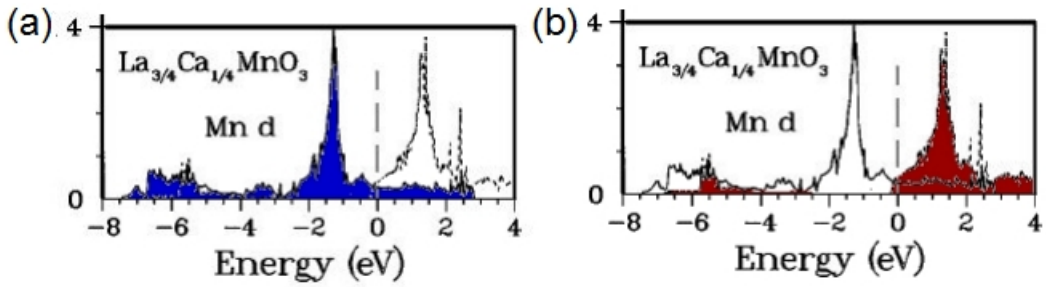

Figure 1.2: Band structure of LCMO with x=0.25 doping, showing the density of states as a function of energy. Figure (a) highlights the available states electrons with spin majority in blue, while (b) shows the spin minority states in red. Note the gap in spin minority states for negatives energies, rendering the manganite nearly 100% spin polarized. Figure reprinted and adapted with permission from Pickett and Singh [5].

a so called half-metal which is nearly 100% spin-polarized, or metallic at the fermi surface for one spin orientation but gapped for the opposing spin.

Pervoskite manganites are one class of materials that exhibit half-metallicity (Figure 1.2), in addition to the important criteria for any application of magnetically ordering near room temperature. First discovered in 1950 [6], manganites received renewed interest in the 1990's for their large decrease in resistance with applied magnetic field, or colossal magnetoresistance. Values of negative magnetoresistance up to 127,000% [7] have been reported in manganite films, where the magnitude of magnetoresistance is defined as the ratio of the resistance difference between those in zero- and finite fields relative to the smaller resistance in finite fields. For a more conventional definition of magnetoresistance that refers to the ratio of resistance difference relative to the larger resistance in zero field, the magnitude of the aforementioned negative magnetoresistance is comparable to 99.92%. These large values of negative magnetoresistance associated with the manganites are additional favorable characteristics for potential applications.. Half-metallicity in the manganites has been predicted by band structure calculations [8], and was experimentally supported by spin resolved photoemission [9], point contact Andreev reflection [10], and scanning tunneling microscopy [11] measurements. The Curie temperature for certain manganite compounds such as $La_{1-x}Sr_xMnO_3$ can be as high as 330K [12], allowing their implementation in devices at ambient temperature. Manganites films can be incorporated into nanoscale devices because of a variety of

successful thin film growth techniques for the material [13], as well as their compatibility with lithographic patterning [14]. Physical integration of manganites films and silicon are possible with a suitable buffer layer between the two systems, such as $Bi_4Ti_3O_{12}/CeO_2$/yttrium-stabilized zirconia [14].

In short, manganites show promise for spintronic devices, but unresolved issues regarding phase separation in manganites, principally involving competing phases of ferromagnetic metallic and antiferromagnetic [15], charge or orbitally ordered [16], or ferromagnetic insulator phases [17], complicates their eventual use in devices. As the sizes of devices shrink to the nanometer scale, electronic film inhomogeneity due to the presence of multiple phases will begin to hinder device reproducibility. Important issues related to the existence of competing orders in various members of the perovskite manganites have been discussed in a comprehensive review article by Dagotto et al. [12] Effort in the research community has focused on $La_{1-x}Ca_xMnO_3$ (LCMO) and $La_{1-x}Sr_xMnO_3$ (LSMO) due to their metallic behavior at appropriate doping and temperature, relatively high Curie temperatures of 260K-330K, and colossal magnetoresistance of up to 127,000% [7]. In this work, we have chosen to focus on $La_{0.7}Ca_{0.3}MnO_3$, as this system has a diverse phase diagram (Figure 1.3), and is an intermediate bandwidth compound prone to phase separation. At the x = 0.3 doping, nominally well within the bulk ferromagnetic metal phase, previous neutron diffraction [18], NMR [19], and scanning tunneling microscopy (STM) [20] measurements have suggested the presence of inhomogeneous phases on the nanometer scale. By investigating phase separation in this model manganite system, we hope to gain insight into physics universal to the manganite family as a whole.

Generation of highly spin-polarized current from ferromagnetic electrodes is only one component to the spintronic devices discussed earlier, as the polarized current must be transported between electrodes with minimal disturbance of the polarization. In this context, organic semiconductors are particularily suited to use as semiconducting spacer layer in spin valves due to the their large spin diffusion lengths [21], leading to reported spin diffusion lengths comparable to the typical layer thickness (45 nm [22]). Organic semiconductors (OSEs) were discovered in 1976, with the doping of polyacetylene with dopant such as arsenic pentafluoride (AsF_5) and halogens allowing tunability

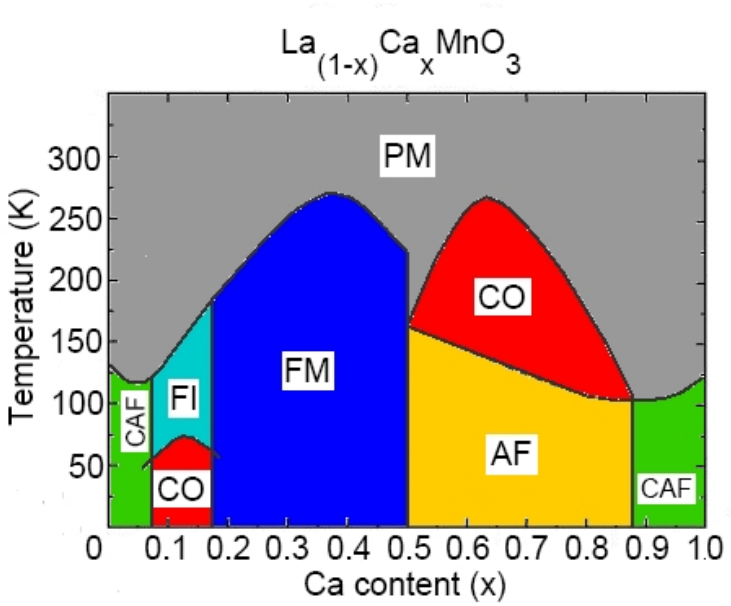

Figure 1.3: Phase diagram of $La_{1-x}Ca_xMnO_3$, plotted with respect to Ca content (x) and temperature. PM signifies paramangetic state, FM ferromagnetic, FI ferromagnetic insulator, AF antiferromagnetic, CAF canted antiferromagnetic, and CO charge ordering. Figure adapted with permission from Dagotto et al. [12]

of the polymer conductivity over 7 orders of magnitude [23]. This work lead to the Nobel prize in Chemistry for Alan Heeger [23] and colleagues in 2000. Additional advantages for using OSEs in applications are the low cost and ease of processing; deposition generally requires suspension of the semiconductor into a solvent, and subsequent evaporation of the solvent on the desired substrate (spin casting), possible at room temperature and pressure, or sublimation of the semiconductor at temperatures in the range of 200°C-300°C as compared to 600°C for conventional semiconducting polycrystalline silicon. In tandem with their semiconducting band gap, electroluminescient properities are present in many organic materials, and were first discovered in anthracene single crystals in the 1960s [24]. Electroluminescence, where electrons and holes combine in the semiconductor to radiate photons, opens up application of organic semiconductors in organic light emitting diode (OLED) applications. OLED with spin-polarized electrodes can show particularly high device efficiency due to the restriction of radiation to spin singlet combinations of electrons and holes as a result of conservation of angular momentum. Sony has recently implemented the organic semiconducting

material in their OLED television [25].

Alq_3 was one of the first organic semiconductors used in a thin film geometry for the purpose of a light emitting diode [26], and it is still employed in LED structures as the electroluminscient layer [27] due to various superior characteristics. For instance, instrinic mobility estimations of Alq_3, crucial to efficient devices, report values comparable to the highest mobility among organic semiconductors [28], confirming the viability of the material for application. The multitude of possible crystalline structure for the material, and the resultant changes in optical properties such as the wavelength of emitted light and the band gap and electronic conductivity, give flexibility in its possible applications.

In order to optimize Alq_3 for use as either a spin transport or electroluminescient layer in nanodevices, understanding of the details of the microscopic conduction in Alq_3 thin films is necessary. A prerequisite to understanding spin transport is understanding charge transport, as the two are intertwined in the spin-polarzied carriers. In spite of significant development of research in the application of organic semiconductors, many details of the microscopic conduction mechanisms in thin film structures are still unknown because most studies are based on bulk measurement techniques that are strongly dependent on properties associated with the grain boundaries. Moreover, bulk measurements of multilayer devices involving Alq3 generally contain convoluted information of different materials, rendering direct extraction of the characteristics of Alq3 difficult. Additionally, Alq_3 film properties appear to be highly dependent on the growth conditions and electrode materials, as some researchers have suggested that the conduction in Alq_3 thin films is sufficiently uniform to be accountable by space charge methods [29], while others propose the parameters controlling conduction are the energy distribution and the number of traps associated with defects or impurities [30], or the injection rate of charges from the electrodes [31].

Scanning tunneling microscopy (STM), and in particular spin-polarized (SP) STM, provides a unique tool to study both the phase separation in manganites and the intrinsic electronic conduction in organic semiconductors. STM uses an atomically sharp tip brought within nanometers of a sample, with an applied bias voltage between the two inducing either electrons or holes to tunnel across the

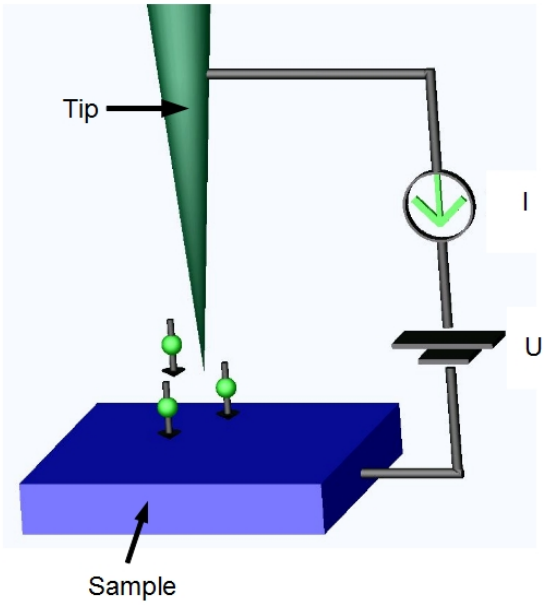

Figure 1.4: STM fundamentally consists of a tip at a bias U with respect to a sample surface, separated by a gap on the order of angstroms. The bias voltage induces a current I between the tip and sample that can serve as a sensitive probe of surface height or electronic properties.

vacuum barrier, as depicted in Figure 1.4. It is capable of spectroscopic measurements with 0.1 angstrom lateral resolution, making it ideally suited to studying nanoscale variations in conduction like those observed in the manganites. Spin-polarized STM also provides added sensitivity of the tunneling current to magnetic orders in the sample, particularly useful for the studies of LCMO with a complex magnetic phase diagram. The operation of SP-STM involves the selection of an appropriate tip material and proper preparation to give a net spin polarization to the tunneling current, which enables the identification of different magnetic domains or orders observed in the system.

STM is also a superior tool for investigating microscopic conduction in organic semiconductors such as Alq_3 due to the simplification of the resulting device structures. Instead of the multimaterial, multilayers devices used in bulk measurements, STM investigations of Alq_3 involve the organic film deposited on a substrate (an LCMO eptaxial film in this work), with varied film thickness allowing separate characterization of the organic semiconducting film and its interface. The absence of a top metallic electrode also circumvents the issue of band bending at the interface of metallic electrode and organic semiconductor and eliminates the complication of electrode material penetrating the

organic semiconductor and dominating the device structure [22], thereby allowing investigations of organic films with sufficiently small thicknesses, closer to the expected ballistic electron length. Eventual SP-STM studies can characterize spin transport in the organic film once charge transport is understood.

Although conventional STM allows extensive study of electronic transport in materials, optically active samples such as organic semiconductors would also benefit from simultaneous optical investgation operating in conjuction with the STM capabilities. For this reason, a portion of this thesis was devoted to designing and building a cryogenic, ultrahigh vacuum, magnetic field compatible STM with additional near- and far-field optical probes for both spatially averaged and spatially resolved photonic detection operating in conjuction with the tunneling current from the STM tip.

1.1 Overview

The thesis is structured as follows. We first describe basics of the STM technique and instrumentation (chapter 2) and the methods of deposting and characterizing LCMO and Alq_3 thin films (chapter 3). In chapter 4, we review the physics of manganites, with special focus on the nominal ferromagnetic metal phase of LCMO, and the experimental and theoretical evidences for phase separation into ferromagnetic metal and other orders on the nanoscale. We then proceed to unpolarized and spin-polarized STM studies of LCMO (chapter 5) under varying temperature, magnetic field, and tip material. The high energy spectral features are consistent with bulk ferromagnetism in LCMO for data taken with both SP and unpolarized STM. We investigate further two types of low energy gaps believed to be associated with a non-stoichiometric ferromagnetic insulator phase and a psuedogap.

The second portion of the thesis begins with a discussion of the mechanism for electron conduction in and the semiconducting characteristics of Alq_3. Some specifics to STM investigation of organic semiconductors are also introduced in chapter 6. We then report on STM studies of the Alq_3/LCMO heterostructures of varying Alq_3 film thicknesses (chapter 7). In addition to identifying changes in the energy levels of the Alq_3 with film thickness, we observe a large increase in the mobility of the

Alq_3 film grown with heating of the substrate during deposition. The mobility values approach experimental estimates of intrinsic mobility limit in the material, implying potentially large effects on the efficiency of devices using Alq_3.

We conclude in chapter 8 with the overall implications of the results and discuss future possible topics to pursue. In appendix A, we include a design for an integrated STM/NSOM (NSOM: near-field scanning optical microscopy) capable of simulataneous optical and electrical characterization of samples at $\sim$10K under ultrahigh vacuum with the option of applied magnetic field.

Chapter 2

Scanning Tunneling Microscopy

Scanning tunneling microscopy (STM) is a flexible technique for non-contact localized spectroscopic measurements with excellent spatial resolution of 0.1 angstroms. It is particularily useful for studying spintronic materials such as manganites and organic semiconductors, as, with an appropriate choice of the STM tip, spin-polarized tunneling current may be injected into the sample, allowing investigations of local magnetic ordering in the sample. Additional advantages include high energy resolution ($\sim$0.1 meV at liquid helium temperatures), and the ability to operate in ultrahigh vacuum to maintain sample quality and at cryogenics temperatures to access a range of phase space of the sample.

2.1 Theory and Principles

STM was first demonstrated by Binnig et al. in 1981 [32]. Electron tunneling is a quantum mechanical process, and in the case of STM, is highly dependent on the bias voltage, tip-sample separation, and density of states (DOS) for the tip and sample. The technique consists of an atomically sharp tip brought within nanometers of a sample, with an applied bias voltage between the two to induce electron tunneling across the vacuum gap. The typical tunnel currents are the range of microamps to femptoamps, and the STM tip is controlled by piezoelectric material to enable atomic-scale resolution for both lateral and vertical directions. The physical priniciple of tunneling is similar to planar tunnel junction experiments [33] consisting of two layered materials separated by a thin oxide barrier with an applied bias, but with the replacement of one layered material with a piezoelectrically

controlled atomically sharp STM tip.

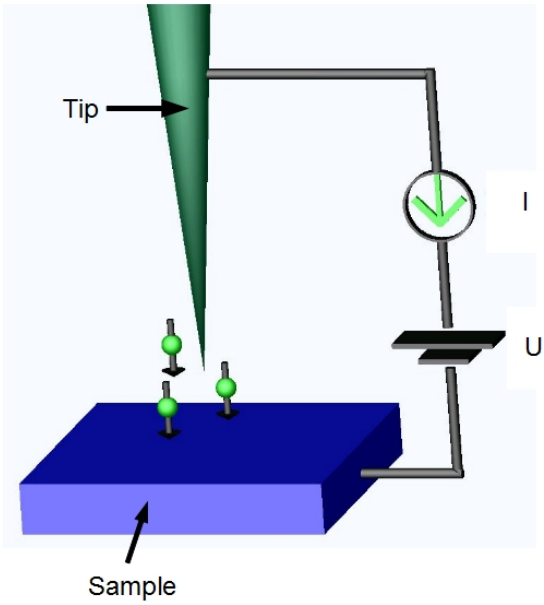

Figure 2.1: Schematics of the basic priniciple of STM operation, showing an atomically sharp tip in the quantum tunneling range above a sample. The tip may be bias at a voltage U with respect to a sample surface for spectroscopic studies.

Wiesendanger uses first-order perturbation theory to calculate the dependence of the tunneling current on voltage and the density of states (DOS) of the tip and sample [34], which yields

$$I \propto \int T(\epsilon, eU) N_t(\epsilon) N_s(\epsilon + eU) d\epsilon, \tag{2.1}$$

with I the current, $N_{t,s}$ the density of states of the tip (t) or sample (s), U the bias voltage between tip and sample, and T the tunneling matrix. In the absence of spin dependence, the tunnel matrix may be approxiamated by the following expression:

$$T(\epsilon, eU) = e^{(-2(s+r)(\frac{2m}{\hbar^2}(\frac{\phi_t+\phi_s}{2}+\frac{eU}{2}-\epsilon))^{1/2})}, \tag{2.2}$$

with ϕ_s and ϕ_t being the work function of the tip or sample, respectively, s the tip/sample separation distance, and r the radius of the tip. The tunneling current is then a function of the joint density of states of the sample and tip weighted by the tunneling matrix. A graphical depiction of the tunneling conductance (dI/dU), expressed by equation (2.1) to be elaborated on later in

this chapter, is shown in Figure 2.2. One characterization of the tunnel junction is the bias voltage divided by the tunneling current, and refered to as the junction resistance. Typical values fot the junction resistance in this work are 100M-1G.

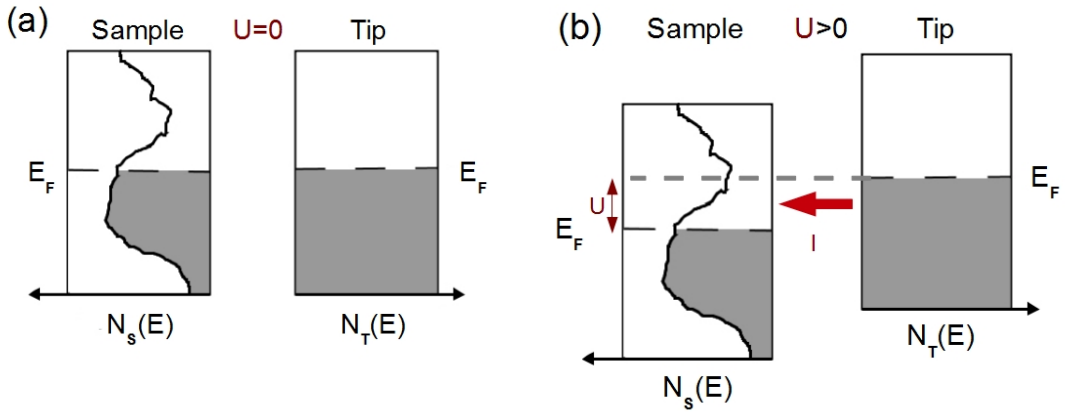

Figure 2.2: Filled states (grey) and unfilled states (white) in tip (N_T) and sample (N_S), with tunneling electrons identified by the red arrow. (a) and (b) indicate zero bias and positive bias to the sample respectively, with electrons at the tip energy of -E tunneling into sample states with energy (eU-E) for 0<E<eU. A negative bias voltage will induce electrons to tunnel from sample to tip, effectively injecting holes into the sample.

2.1.1 Operational Modes

In this work, STM is employed in three possible modes of operation: constant current topographic maps, tip sample separation vs bias voltage scans, and spectroscopic conductance maps. The tunnel matrix T discussed in the previous section (equation (2.2)) leads to an exponential dependence of the tunneling current on the tip/sample separation s. Then, with a bias voltage U applied to the sample, if a feedback loop is set up to control the difference between the measured current and a chosen current set point that determines the height of the STM tip above the surface, the exponential change in the tunnel current with tip displacement allows a very sensitive and accurate method to maintain a constant tip-sample separation. This approach proves useful if the STM tip is rastered across the sample surface, as, assuming the sample density of states for the energy range from 0 to U is reasonably constant for the area studied, the map of the STM tip height with x and y displacement will correspond to the sample surface topography. This mode of operation is referred to as a constant current topograph. The exponential separation dependence of the tunnel

current makes excellent spatial resolution in the z-direction of 0.1 angstroms easily obtainable, with the corollary that STM will only detect elements of the surface which conduct in the energy range from 0 to U. Figure2.3 depicts a topography scan of one $La_{0.7}Ca_{0.3}MnO_3$ epitaxial film fabricated and studied in this work as an example.

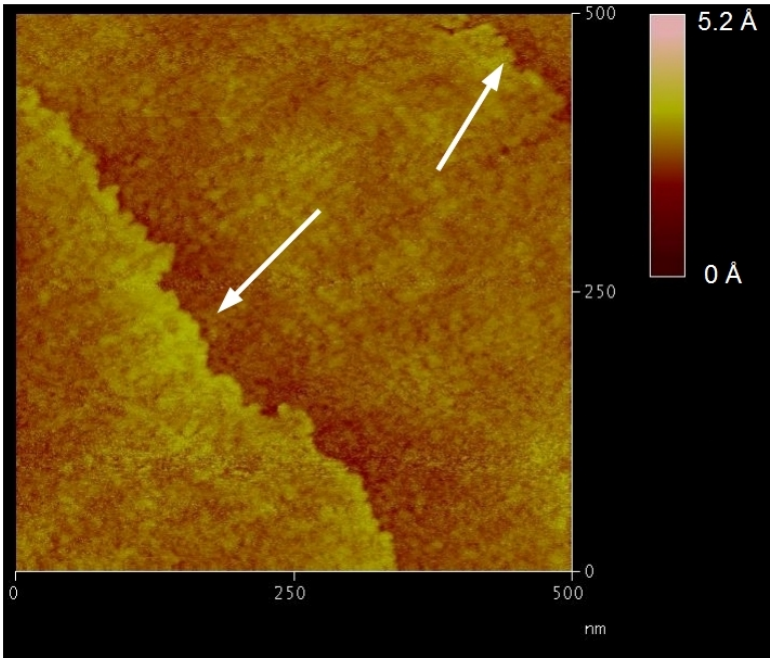

Figure 2.3: Topographic image of as grown LCMO film. Highlighted in the figure are terraces of one c-axis lattice constant (∼3.86 angstroms). The scale is 5000 angstroms by 5000 angstroms by 5.2 angstroms.

A related technique of tip separation vs bias voltage scans utilizes the same feedback loop as the topography scans, except instead of rastering the physical location of the tip, the bias voltage is ramped with the tip height changed to maintain a constant current. If employed on a metallic (i.e., gapless) film, the tip displacement should vary on the order of angstroms, as predicted by Eq. 2.2. For a traditional semiconductoring film such as Si, the behavior of the tip should be similar until the bias voltage reaches below that of the energy gap, when the tip will crash into the sample due to the lack of available conducting states. This mode of operation proves useful to study organic semiconducting films deposited on a metallic substrate because (1) the underlying metallic films prevents a tip crash at bias voltages within the semiconductor gap, only leading to penetration into the semiconducting film until a tunnel junction can form with the metal, and (2) organic

semiconducting films are sufficiently soft that they do not damage the STM greately when plunged. This technique can provide useful information about the mobility of the organic semiconducting sample, as discussed in chapter 7.

While topographic scans show the surface topology of conducting features of the sample studied over a spatial range on the scale of microns down to angstroms, they give no information concerning the electronic density of states of the sample. To this end, STMs may be employed in the mode of scanning tunneling spectroscopy (STS), where the feedback loop between the tunneling current and the tip position is disabled, and the bias voltage is changed while observing the evolution of the tunneling current. If we differentiate I (equation 2.1) with repect to the bias voltage, and assume that the density of states of the tip is reasonably constant in the voltage range we study ($dN_t/dU \sim 0$), a frequent assumption for unpolarized Pt/Ir tips used in this work, we obtain

$$\frac{dI}{dU}(U) \propto T(eU, eU, s)N_t(0)N_s(eU) + \int_0^{eU} \frac{dT(\epsilon, eU, s)}{dU} N_t(\epsilon)N_s(\epsilon + eU)d\epsilon, \tag{2.3}$$

Although T is exponentially dependent on U, in general it is smooth and monotonic so that we can discount the second term and attribute any structure observed in dI/dU to a term proportional to N_s(eU) (the density of states of the sample at the bias voltage) [34].

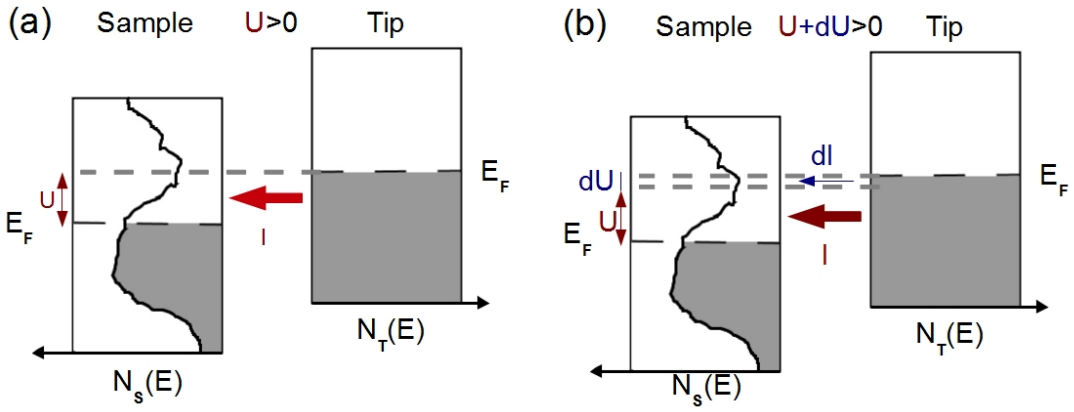

Figure 2.4: DOS between tip and sample and induced tunneling current at bias voltages of U (a) and U+dU (b). The nominal current I at bias U are labeled in red, while the differential conductance dI due to the additional bias dU are both labeled in blue.

$$\frac{dI}{dU}(U) \propto T(eU, eU, s)N_t(0)N_s(eU), \tag{2.4}$$

The differential conductance is depicted graphically in Figure 2.4. As the differential conductance at bias U can then be related to sample density of states, and the remaining terms do not change with bias U, the differential conductance measured for a range of energies is effectively a measurement of the sample density of states. This makes the differential conductance a sensitive probe of the sample's electronic structure. It is important to note that in the case spin-polarized STM tips, we can not make the assumption that the tip density of states is constant with energy, and must turn to modeling the measured conductance through simulation of the tunneling process(section 2.1.3). Feenstra and Stroscio [35] showed the normalized conductance of (dI/dU)/(I/U) is proportional to the electronic density of states while minimizing the dependence on the tip sample separation of the tunneling matrix T. For these reasons, the majority of spectroscopic data in this work focuses on the normalized conductance, which will be referred to as $\bar{G}$. In practice, a differential conductance measurements is performed by fixing the tip position, disabling the current-tip height feedback loop, and scanning the bias voltage between tip and sample while monitoring the tunnel current. Postmeasurement analysis of the data is performed by custom Matlab programs.

A conductance map is a method to combine the spatial resolution of topographic scans with the detailed spectroscopic information in normalized conductance measurements, and is valuable in its ability to investigate inhomogeneity in the spectral characteristics of the electronic density of states. In this mode, over a chosen scan area, a series of conductance measurements are performed in a grid pattern, with each intersection of grid lines a location for the conductance measurement. The tip is initially located in a corner of the grid, the current-tip height feedback loop is disabled, and a spectroscopic scan is performed. After the spectroscopic scan, the STM current feedback loop is reengaged, the tip is translated to the next location on the grid, the feedback is disengaged, and a conductance measurement is performed again. For example, a condutance map over a 500 nm by 500 nm area with 128 pixel by 128 pixel resolution will consist of conductance measurements separated spatially by 3.91 nm in both the x- and the y-direction. This method is ideal to observe

variations in film conductance over the scan area, and is particularily valuable to determine the statistial distribution of features in the tunneling conductance.

2.1.2 Spin Polarized STM

Spin polarized STM is a measurement technique that uses an STM tip with an imbalance of spin majority and spin minority electrons (or holes) to create a spin-polarized tunneling current. The injection of a spin-polarized current of electrons or holes makes SP-STM a particularily sensitive technique to detect magnetically polarized phases in the sample, as the differential conductance is sensitive to the unequal spin majority and spin minority electron density of states in these phases. Recent example of this technique include recording magnetization curves and low energy magnetic interactions of individual Co adatoms on Pt(111) surfaces [36] and investigating spin frustration and asymmetric ordering in spiral staircases in Cr(001) films [37].

GaAs STM tips pumped with circularily polarized light [38] was one of the first techniques to achieve this asymmetry in the spin population, but complications such as focusing the laser light for adequate coupling with the GaAs and excitations induced in the sample by laser made implementation difficult. A more common approach now is the uses of ferromagnetic or antiferromagnetic materials, either in bulk for the STM tip or used as a film coating over a non-magnetic tip. Professor Roland Wiesendanger of the University of Hamburg has been particularily active in spin-polarized tip development, experimenting with bulk Fe [39], and coatings of $Cr0_2$ [40], Fe [41], Gd [41], and Cr [41].

Integral to spin-polarized STM measurements is the choice of tip and resulting density of states for spin majority and minority electrons. The magnitude of this imbalance between the two populations can be quantified by the polarization P_t, which is defined as

$$P_t(E) = \frac{N_{t\uparrow}(E) - N_{t\downarrow}(E)}{N_{t\uparrow}(E) + N_{t\downarrow}(E)}, \tag{2.5}$$

where $N_{t\uparrow,\downarrow}$(E) indicates the density of states in the tip at energy E for spin majority ($\uparrow$) or spin minority ($\downarrow$) electrons. The polarization will be 0 for completely unpolarized current, and 1 for

complete polarization. Spin polarization of the tip can always be estimated from band structure calculations of the material for thin films or in bulk depending on the material used, but often the tip geometry or strain effects for thin film or bulk magnetic materials complicates the resultant density of states. It is also difficult to accurately measurement the isolated spin polarization of the tip independent of the sample, as both polarizations factor into the measured conductance and no reference sample with a constant imbalance of spin majority and spin minority states with respect to energy exists. Morever, the changing population of spin majority and minority states with energy necessitates modeling of the tunnel conductance for meaningful interpretation of data.

If the sample aslo has an asymmetric spin density of states, and if the bias voltage U is low enough so that elastic tunneling processes dominate and negligible spin flipping occurs [34], for parallel magnetic orientation of tip and sample the resulting differential conductance can be described as

$$\frac{dI}{dU}(U) \propto T(eU, eU, s)N_{t\uparrow}(0)N_{s\uparrow}(eU) + T(eU, eU, s)N_{t\downarrow}(0)N_{s\downarrow}, \tag{2.6}$$

Essentially, the two spin populations operate as separate conductance channels, depending on the relative magnetic orientation of the tip and sample(Figure 2.5). In the parallel configuration, electrons in the spin majority orientation can access the spin majority states in the sample, and likewise for the spin minority electrons. In the antiparallel configuration, the tip majority electrons can only tunnel into sample spin minority states, and vice versa. This relationship can be generalized for an arbitrary angle between the tip and sample magnetic orientation θ, if α=cos(θ) and β=sin(θ), as

$$\frac{dI}{dU}(U) \propto T(eU, eU, s)N_{t\uparrow}(0)(N_{s\uparrow}(eU)\alpha + N_{s\downarrow}(eU)\beta) + T(eU, eU, s)N_{t\downarrow}(0)(N_{s\downarrow}(eU)\alpha + N_{s\uparrow}(eU)\beta), \tag{2.7}$$

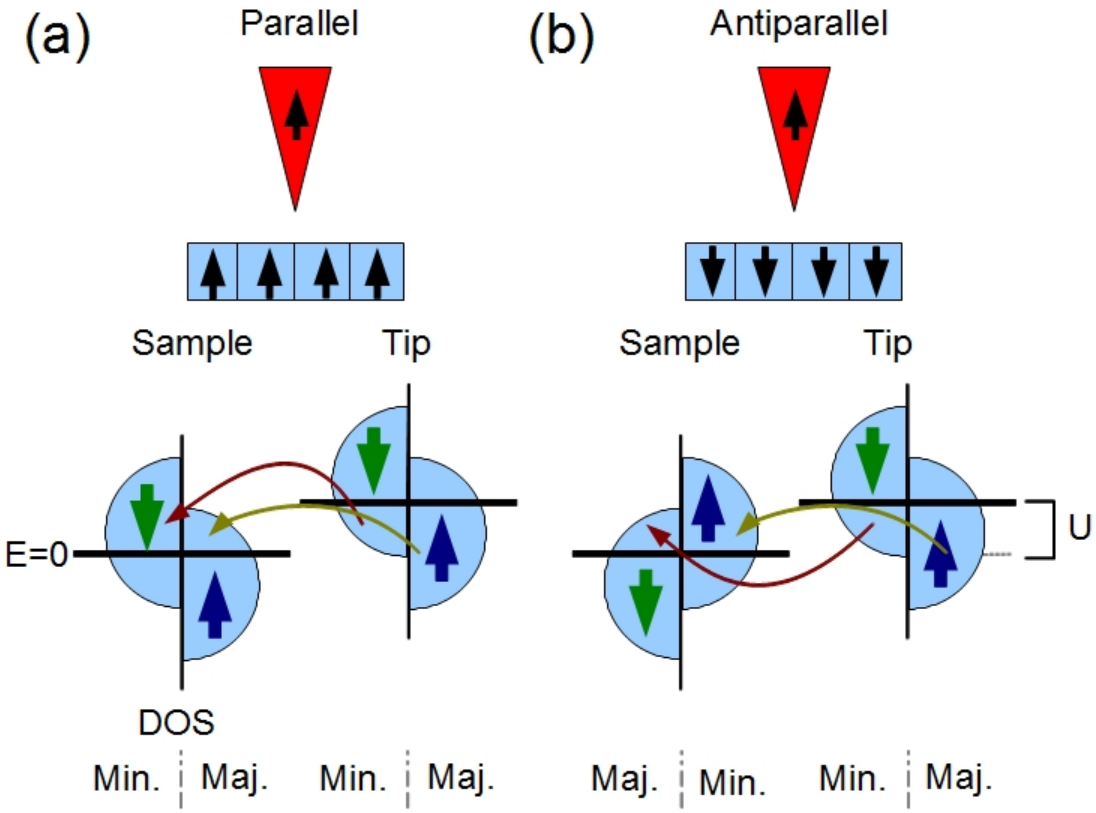

Figure 2.5: Tunnel conductance between tip and sample under a bias voltage U applied to the sample and for the condition of parallel and antiparallel magnetization configurations in (a) and (b) respectively.

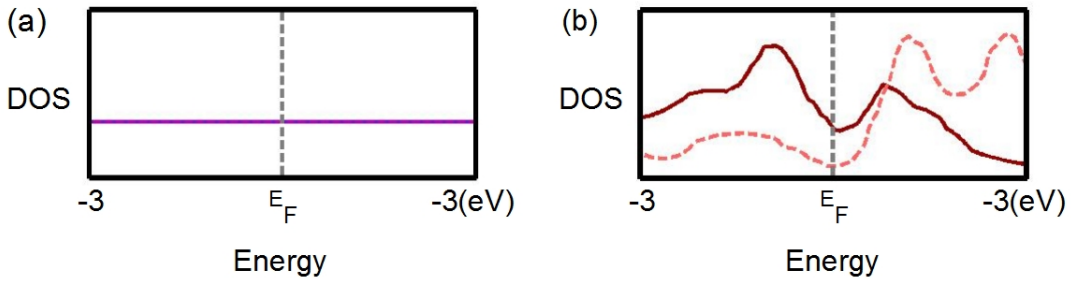

Figure 2.6: Assumed unpolarized Pt/Ir density of states (a) and calculated Cr density of states (b) for the first atomic layer for spin majority (solid line) and spin minority (dashed line) [42].

2.1.3 Conductance Modeling

In non polarized spectroscopic measurements, for typical tip materials such as a bulk Pt/Ir alloy, the density of states of the tip is taken as relatively constant in energy(Figure 2.6 (a)), allowing easy extraction of the sample density of states from the differential conductance. However, for spin-

polarized STM, the energy dependence of spin majority and spin minority density of states for both tip and sample must be explicitly considered to interpret the resulting data. For the Cr coated Pt/Ir STM tips, we have used the density of states for the first atomic layer of a Cr thin film [42](Figure 2.6 (b)). In order to model the tunneling, we must return to the full expression for the tunneling current (section 2.1), calculate the resulting currents separately for both spin populations while assuming a specific relative spin orientation between the tip and sample, and combine the two currents to determine the total current. Assuming parallel spin orientation of tip and sample magnetization, we have

$$I_T(U) = I_{\uparrow,\uparrow}(U) + I_{\downarrow,\downarrow}(U), \tag{2.8}$$

The differential conductance is then calculated by

$$\frac{dI}{dU}(U) = \frac{I_{\uparrow,\uparrow}(U+dU) + I_{\downarrow,\downarrow}(U+dU) - (I_{\uparrow,\uparrow}(U) + I_{\downarrow,\downarrow}(U))}{dU}, \tag{2.9}$$

In practice, these calculations are performed by a custom designed Matlab^{TM} program, with 25 meV resolution. A representative calculation is displayed in Figure 2.7.

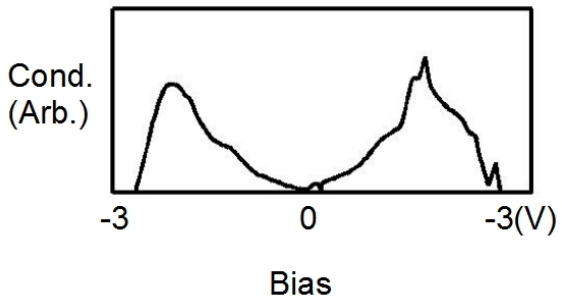

Figure 2.7: Modeled tunnel conductance for Cr tip and LCMO ferromagnetic state, assuming anti-parallel orientation of tip and sample magnetization.

2.2 Instrumentation

2.2.1 STM Probe

Scanning tunneling microscopy in practice requires, in addition to the sample and tip, multiple systems to control the tip and sample position, amplify and shield the tunneling current from electronic and vibrational noises, and to control the environment the STM operates under in terms of temperature, vacuum, and magnetic field. As these details are system depedent, we will discuss the specific STM system used to perform spin-polarized STM experiement on $La_{0.7}Ca_{0.3}MnO_3$ discussed in chapter 5, previously designed by Ching-tzu Chen and Nils Asplund [43].

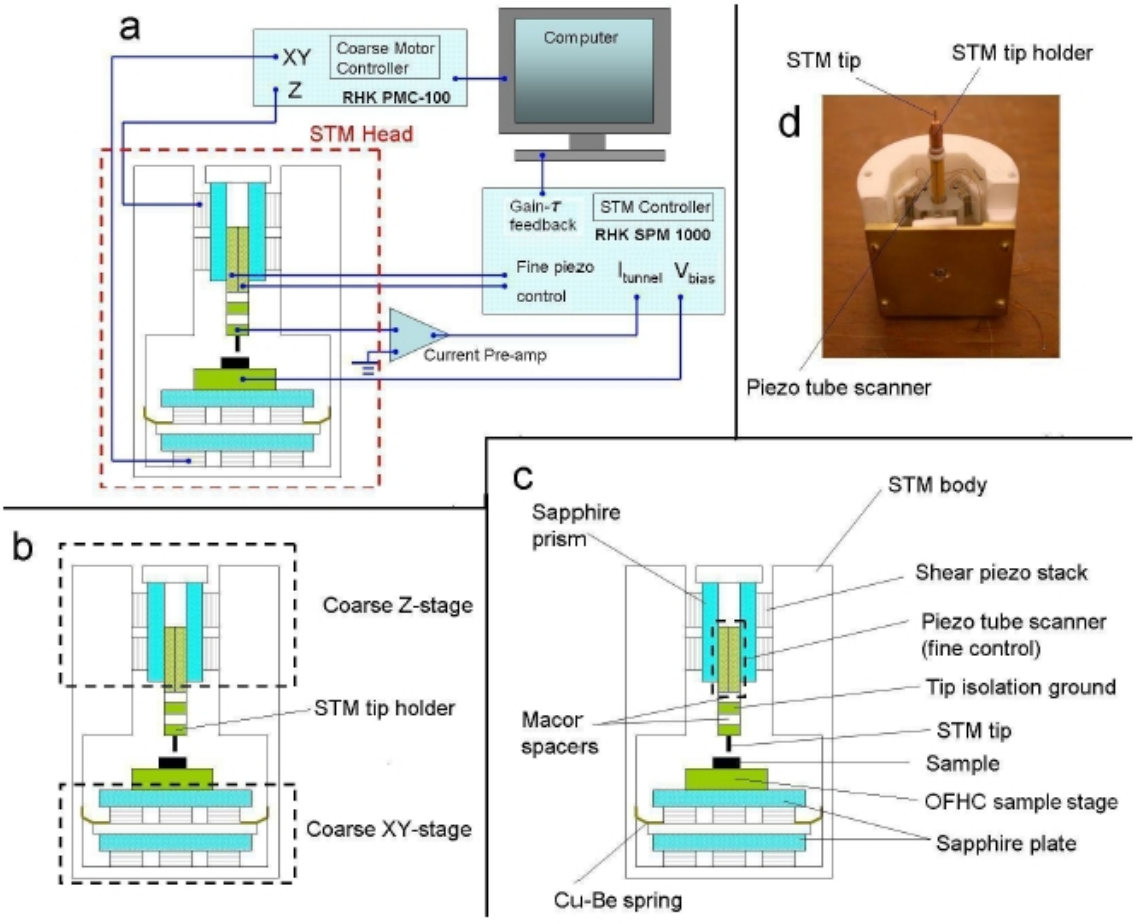

Figure 2.8: (a)A side view of the STM head and the control electronics. (b) Major components of the STM head. (c) Component details of the STM head. (d) Image of the STM z-stage. Figure adapted with permission from Beyer [44].

The core of the STM consists of the sample, tip, coarse approach z-stage, xy-sample translation

stage, and fine translation piezotube scanner (Figure 2.8 (b)), and is refered to as the STM head. The sample is mounted on an oxygen free high conductivity copper (OFHC) stage with bias voltage connection, while the tip is fixed in a copper tip holder by a brass screw. Rastering and positioning of the tip with ± 15 micrometer xy-range and 4.5 micrometer z-range at 300K is accomplished by mounting the tip holder in a piezoelectric tube, with applied bias voltages from the control electronics producing a strain in the tube to translate the tip. Tip translation is possible to less than 0.1 angstroms in the xy direction and 0.01 angstroms in the z-direction. The piezotube, tip holder, tip isolation ground, and macor and sapphire structural components make up the fine positioning stage. While loading, the tip and sample are typically separated by a distance on the order of centimeters to prevent tip and sample contact (tip crash), outside the z-range of the tube scanner. The coarse approach z-stage translates the fine positioning stage to close the gap between tip and sample until the sample surface is within range of the piezoelectric tube scanner. The coarse approach mechanism uses piezoelectric stacks pulsed with 400 V waveforms in a stick-slip fashion [43] to translate the fine positioning stage in 0.8 μm increments at 300K toward or away from the sample. The sample stage is also mounted on an xy-translation stage that employs the same stick-slip mechanism to move the sample 1-2 cm in the xy directions to locate specific features or to avoid damaged or non-stochiometric sections.

The control electronics consist of the RHK SPM-100 SPM controller, PMC-100 piezo motor, RHK preamplifer and controlling computer(Figure 2.8 (a)). The preamplifier is mounted directly on the probe that contains the STM, and serves as an initial amplification stage for the tunneling current to increase signal-to-noise ratio. The SPM-100 provides the bias voltage to the sample, collects and further amplifies the tunneling current from the preamplifier, contains the feedback circuit between bias current and tip z-position, provides the voltages to the piezotube scanner to control the fine position of the STM tip, and records data to the computer. The PMC-100 piezo motor supplies the high voltage waveforms to the z-stage and xy-stage to adjust sample and fine positioning stage position respectively.

The STM head is physically located on the end of a low temperature probe, and the probe

is placed into a stainless steel jacket once the sample and tip are loaded in the head. Vacuum is established in the jacket by a detachable turbopump, with pressures on the order of 10^{-6} mbar acheived at 300K before loading the jacket into the dewar. Additional pumping at low temperatures, including cryopumping of the jacket walls when placed in cryogens, and a charcoal pump located at the bottom of the jacket, allows acheivement of less than 10^{-9} mbar at 6K. The STM probe and jacket is mounted in an Oxford cryogenic dewar with a 7T superconducting magnet for low temperature and magnetic field measurements. The dewar holds ∼35 liter of helium, with a boil-off rate of ∼7 liters per day, allowing for 3 days of measurements with applied field with a full dewar of helium. Depending on the required temperature, the dewar is filled with ambient nitrogen gas for 300K, with liquid nitrogen for 77K, or with liquid helium for 6K and magnetic field measurements. The dewar is attached to an aluminum plate floated on four pneumatic air dampener legs to isolate the system from building vibrations, with added lead bricks and shot to balance the load on the pneumatic legs and decrease the resonance frequency of the system. In addition the dewar is housed inside a sound dampening box located in a room lined with acoustic dampening foam.

An additional STM system was designed, partially built, and used for the organic semiconductor experiments in chapter 7 for this work, with details of the design located in appendix A.

2.2.2 STM Methods

2.2.2.1 Tip Preparation

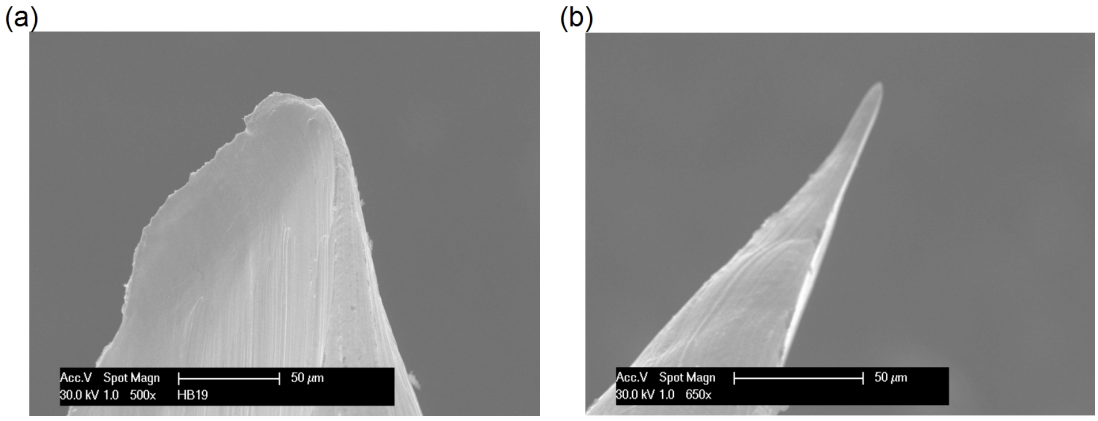

Figure 2.9: SEM Image of as cut Pt/Ir STM tips (a), and Cr coated Pt/Ir tip (b).

STM tips were cut from 80% Pt/20% Ir alloy wire in ambient atmosphere, as a Pt/Ir alloy is the most common material for STM tips for experiments which require tip preparation outside of vacuum due to the lack of oxide formation. Tips are mechanically sheared to achieve the requisite sharpness for STM measurements, with the cut tips electrochemically etched for approximately 10 seconds in a solution of $CaCl_2{\sim}2H_2O$ (35 g), deionized water (200 mL), and acetone (10 ml) at 10-15V_{AC}. The tips are then immediately loaded into the STM for unpolarized measurements, or stored for further metallic coating. The method for spin-polarized tip preparation is modeled after Professor Roland Wiesendanger's group's techniques [45], and involves evaporate deposition of magnetic Cr onto the Pt/Ir. We chose to focus on evaporatively deposited thin film Cr onto Pt/Ir bulk tips due to a minimum stray field generated by the thin film magnetic layer. This is due to the confinement of ferromagnetic ordering to the initial four Cr layers, with antiferromagnetic ordering of the remainder of the film [42]. The Cr deposition is performed in the metal evaporation chamber of Professor Harry Atwater, with three Pt/Ir tips coated at once, under a vacuum of less than 5×10^{-6} mbar. The tips are mounted in a custom built STM tip holder, with the end for STM facing the Cr evaporation source. The deposition rate of Cr is established using a quartz crystal monitor, with a typical rate of 0.4 angstroms per second. The thickness of film deposited is 8.73 nm, or 30 atomic layers of chromium. The radii of curvature from SEM tips for as cut tips vs Cr coated is 46 vs 80 nm. Whether atomic resolution is still possible with Cr coated tips has not been thoroughly investigated.

Chapter 3

Film Growth and Characterization

The choice of thin-film growth techniques depends sensitively on the nature of the material to be deposited and the intended applications of the resulting thin films. For the investigation of intrinsic physical properties of specific materials in the form of thin films, it is essential to ensure structurally ordered and stoichiometrically well-defined samples to prevent incorrect conclusions drawn from extrinsic factors such as structural disorder, growth defects, and stoichiometric inhomogeneity. The perovskite manganites, like other complex oxides, are suited for the pulsed laser deposition (PLD) techniques in their thin film fabrication. With stoichiometric targets and proper choices of substrates, substrate temperatures, oxygen partial pressures, laser fluences and sample cooling rates, the PLD growth process can produce high-quality single crystalline thin films with controlled thicknesses. On the other hand, for organic semiconductors (such as Alq_3) of relatively low sublimation temperatures, thermal evaporation is the preferred means of thin film growth. In general the growth temperature, the substrate material and the vacuum condition are also important variables that control the quality of the resulting organic thin films.

Regardless of the specific growth method, structural characterizations of both LCMO and Alq_3 thin films are critical to ensure high-quality material before further investigations of their physical properties. The specific structural characterization techniques vary for each system. In the case of LCMO thin films, the sample lattice constants were measured by x-ray diffraction to ensure epitaxial and minimally strained crystal growth. In addition, superconducting quantum interference device (SQUID) magnetometry was employed to measure the temperature and magnetic field dependence

of the sample magnetization. The magnetization vs temperature measurements under a small but constant magnetic field (typically ∼100 Oe) provided direct information about the onset of the ferromagnetic phase transition, the Curie temperature. On the other hand, the magnetization vs magnetic field measurements at a constant temperature in the ferromagnetic state yielded magnetic hysteresis curves that saturated at a characteristic field. On the other hand, the surface morphology and film thickness of both LCMO and Alq_3 thin films were monitored by atomic force microscopy (AFM).

3.1 Deposition Techniques

3.1.1 Pulsed Laser Deposition

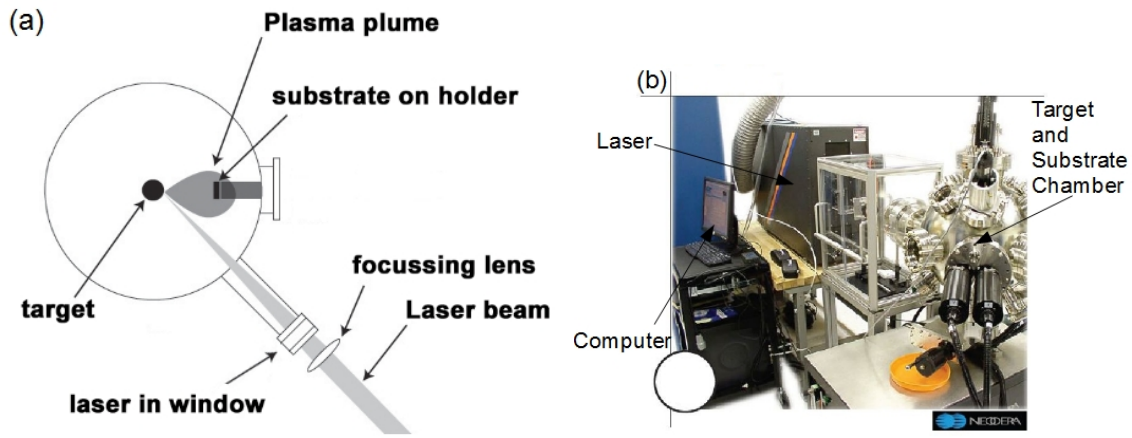

Figure 3.1: (a) PLD block diagram. (b) Picture of the PLD chamber.

The LCMO films grown in this work were deposited by PLD, where a high energy pulsed laser was used to superheat a target material into a plasma for deposition on a substrate. Among the advantages of pulsed laser deposition over competing techniques such as molecular beam epitaxy and chemical vapor deposition are the match in stoichiometry between the resulting thin film and target, the tunability of deposition rate due to the pulsed nature of the laser, and the relatively high kinetic energy imparted to the deposited material to make it sufficiently mobile across the substrate surface to prevent restructuring into clusters [46]. The basic experimental configuration is as depicted in

Figure3.1, which consists of the laser, a target of the same stoichimetry as the desired thin film, and a heated substrate in a background of reactive gas environment. The laser uses ultraviolet light with pulse duration of tens of nanoseconds, with fluence in the range of 10-500 MW/cm^2. As the pulse irradiates the target, electrons in the material absorb the energy as plasmonic excitations, which are thermalized by the lattice and superheat the target within the absorption length (typically $\sim$10 nm) [46]. The highly energetic target material forms a plasma with estimated temperature of several thousand Kelvin [46], whose diffusion to the substrate is mediated by collisions with the background gas molecules. Depending on the chemistry of the target material, the gas may be inert or chemically reactive (including O_2, N_2, or H_2). The substrate is often chosen to lattice match the film material to ensure epitaxial growth, and is at elevated temperatures during deposition to provide the arriving ions sufficient thermal energy to locate at thermodynamically sites and grow into a well-ordered thin film.

The PLD system used was a Neocera Pioneer 180 Pulsed Laser Deposition system with a 300 mJ KrF laser. The substrate used was $(LaAlO_3)_{0.3}(Sr_2AlTaO_6)_{0.7}$, chosen because the small c-axis lattice mismatch of +0.3% helped minimize the strain in the resulting films, thereby preventing significant strain-induced changes in the electronic properties of the thin film samples [47] [48]. The films were deposited with 60,000 shots in a 100 mtorr oxygen background pressure with a substrate heated to 650°C and subsequently annealed at the same temperature for 2 hours in 100 torr O_2. The resulting films were 100nm in thickness, and were stored after deposition in a dessicator to prevent degredation from gaseous H_2O. Immediately before STM measurements, the LCMO film was etched in a 0.5% dilute bromine in ethanol solution for 2 minutes to remove non-stochiometric $CaCO_3$ on the sample surface due to reaction of the Ca component in LCMO with the ambient CO_2.

3.1.2 Organic Film Sublimation

Evaporative deposition and spin coating are the two most frequent methods for deposition of organic semiconductor layers. Between the two methods, evaporative deposition is found to be superior for depositing thin films (<10 nm) of Alq_3 because of its capability of yielding better thickness uniformity

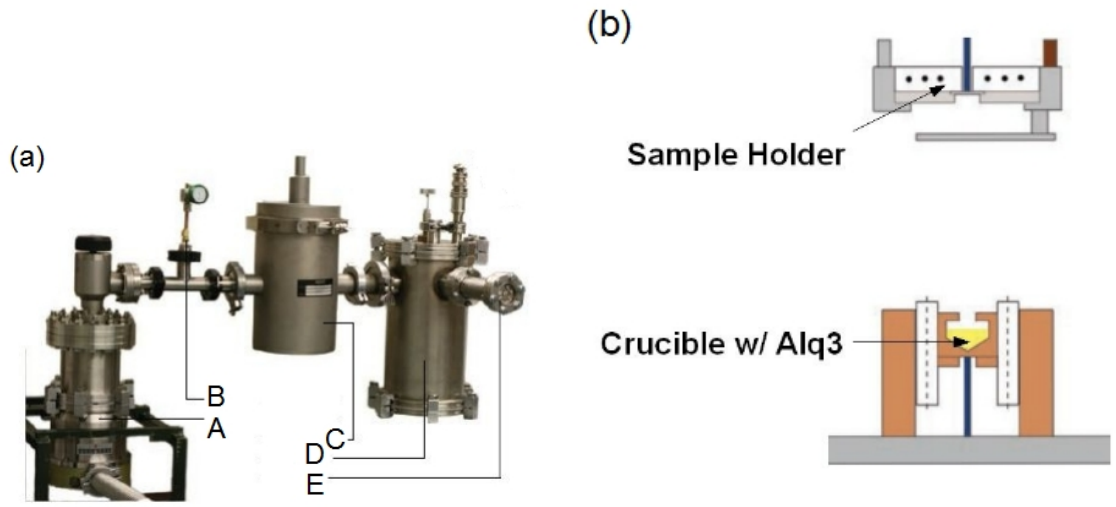

Figure 3.2: (a) Organic Deposition System: A, Turbomolecular pump. B, N_2 inlet. C, Liquid N_2 cold trap. D, Deposition chamber. E, Ion gauge. (b) Schematic of the side view of the organic deposition chamber.

and its ability to control the substrate temperature and change film morphology. Evaporative deposition, which in this case is sublimation, uses a crucible filled with organic material opposite a substrate, with the crucible heated past the sublimation temperature of the organic molecule to induce deposition on the substrate.

Depositions of Alq_3 thin films were performed in a custom designed and assembled organic deposition chamber, with Figure3.2 showing a schematic of the system and chamber. The substrate for deposition was mounted on the sample holder stage opposite the crucible with CuBe springs. Independent heaters and thermocouples allow variable crucible and substrate temperature from room temperature up to 300°C and 200°C, respectively, throughout the deposition. Vacuum was established with a turbo pump backed by a mechanical pump and a cold trap, and depositions were typically performed below 2 x 10^{-6} mbar pressure. N_2 gas filtered through a liquid N_2 cold trap is used to vent the chamber. Substrates used for the Alq3 thin film deposition were either LCMO films or bare $SrTiO_3$ (STO) substrates (used for characterization of growth parameters), and predeposition cleaning procedures included sonication of the substrates in dicholoromethane, hexane, acetone, and isopropanol before loading into the chamber. The substrate was shielded from line of sight with the crucible by a shutter, and a 10 min stabilization time was necessary once the crucible reached the

desired temperature before starting a deposition. Typical deposition parameters were the crucible and substrate temperatures of 245°C and 145°C respectively, which resulted in deposition rates in the range of 0.22-1.0 nm/min. Films were grown up to 20 nm thickness by varying deposition time. After deposition, the heterostructures of Alq3 and LCMO or the pure films of Alq3 on STO were either immediately loaded into an STM for conductance measurements, or stored in a dessicator for later AFM measurements of the film thickness or surface roughness.

3.2 Characterization Measurements

3.2.1 X-ray Diffraction

X-ray diffraction is used to confirm epitaxial crystal growth with minimized strain of LCMO on the substrate. The technique uses an incident beam of x-ray photons with varied angles of incidence relative to the substrate. Normally, each atom scatters x-rays indepedently, but a constructive scattering amplitude becomes possible if the incident angle θ of the photons and the interatomic spacing d obey Bragg's law of

$$2dsin\theta = n\lambda, \tag{3.1}$$

where λ is the wavelength of the photon and n is a integer [49]. This situation is depicted in Figure3.3.

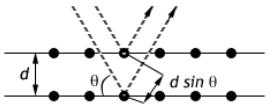

Figure 3.3: Graphical depiction of the necessary condition for constructive X-ray scattering from Bragg's law.

By varying the incident angle of the photons, it is possible to determine from peaks in the scattering amplitude the interatomic spacing of the crystal. This method allows identification of a single uniform layer spacing or multiple layers with differing lattice constants in the film. Comparison

of the lattice constants of the film with those of the bulk crystal also allows characterization of the strain in the film as compressive or expansive. The x-ray diffractometer used was a Philips X'pert PW3040 model, with a 1.54 angstroms Cu Kα x-ray source. Figure 3.4 shows a representative data set, with the 47.78° peak due to the LCMO film 3.87 angstroms c-axis lattice constant and the 47.05° peak due to the LSAT substrate 3.88 angstroms c-axis lattice constant both highlighted.

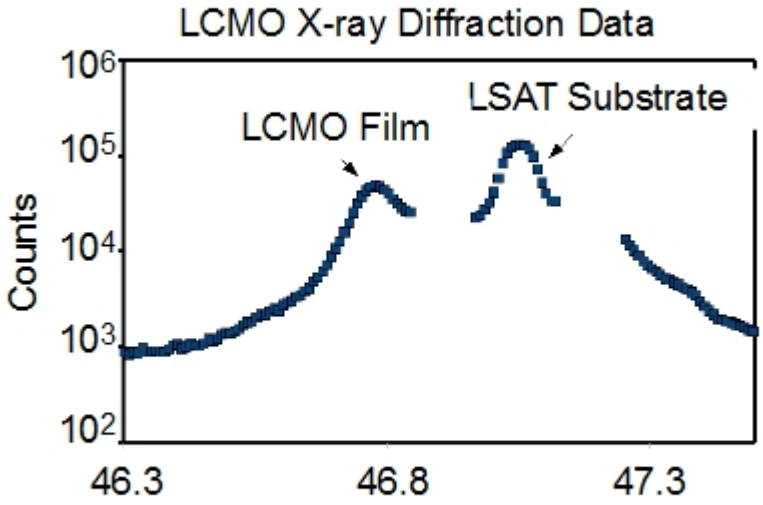

Figure 3.4: X-ray diffraction data from an LCMO on LSAT thin film, with corresponding peaks identified.

3.2.2 SQUID Magnetometry

A superconducting quantum interference device (SQUID) magnetometer was used to investigate the magnetic response of ferromagnetic thin films as a function of temperature and applied field and to determine the Curie temperature of various LCMO films. A SQUID utilizes a pair of Josephson junctions in a superconducting loop to make a device whose voltage output is a very sensitive measure of the magnetic flux enclosed by the superconducting loop [50]. The magnetometer operates by translating a magnetic sample into and out of two superconducting coils inductivelly coupled to the

SQUIDs input coil; the induced current in the superconducting coils as the result of time-dependent flux variations can be detected by the SQUID with high sensitivity [50]. The magnetometer used in this work was a Quantum Design MPMS, located in the Molecular Materials Research Center in the Beckman Institute.

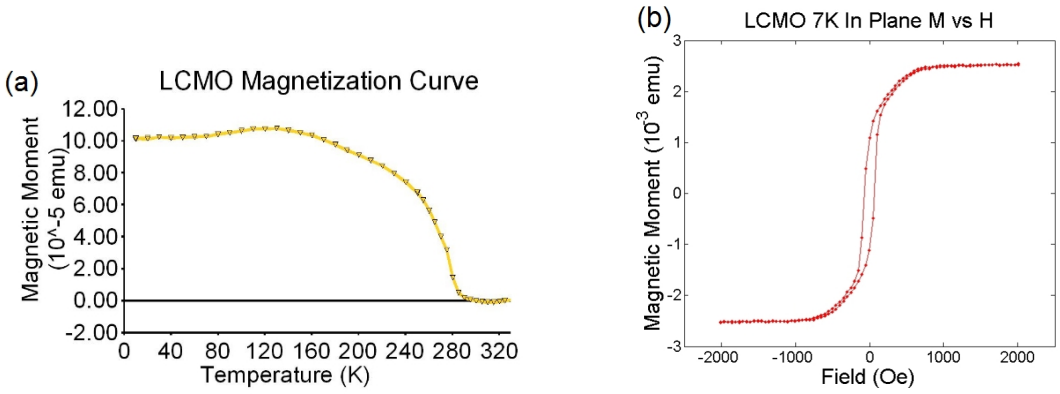

Figure 3.5: (a): Magnetization vs temperature with high temperature background removed for an LCMO film (b): Magnetization vs magnetic field for an LCMO film at 7K. Magnetic field values are in Oersteads (Oe).

Generally speaking, a Curie temperature of the film comparable to the bulk Curie temperature of 260K is suggestive of stochiometric consistency between the film and target. On the other hand, a significantly lower Curie temperature of the thin film would be an indicator of non-stoichiometric growth due to oxygen or calcium deficiency in the film. The Curie temperature was measured by applying a magnetic field of 100 Oersteads (Oe) at room temperature, cooling the sample to 5K, and then measuring the magnetization of the sample as a function of temperature while warming to 330K. The Curie temperature was identified as the temperature when the magnetic response of the sample ceased to differ significantly from the high temperature background. A typical M vs T curve illustrating the 260K Curie temperature is shown in Figure3.5 (a).

The minimum necessary applied magnetic field to change the LCMO domains from an initial state of random alignment to one of all parallel to the field and saturate the magnetization is the coercive field. This value is a function of the sample temperature, and is relevent for later spin-polarized scanning tunneling microscopy measurements where the magnetic orientation of the sample domains with respect to that of the tip must be reversed by the applied magnetic field (Figure3.6).

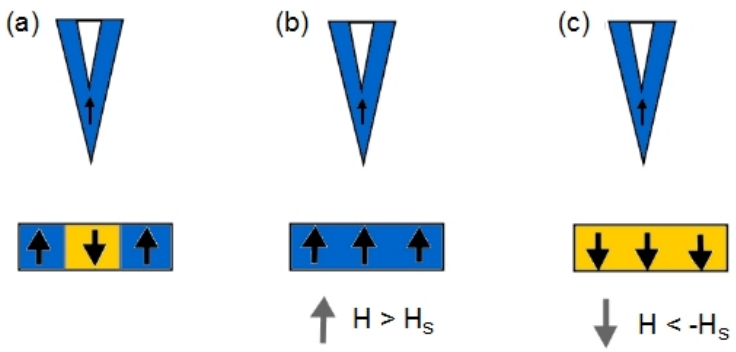

Figure 3.6: Magnetic orientation of tip and ferromagnetic sample in (a) initial 0 field, (b) positive field H>H_c, where H_c is the coercive field for the sample, and (c) negative field H<-H_c. This assumes the coercive field of the tip is greater than that of sample so that the tip magnetic orientation is unaffected by the reversed magnetic field.

The coercive field of the film at a specific temperature was measured by intially cooling the film in zero magnetic field. Once the temperature stabilized, the magnetic field was ramped from 0 Oe to +3000 Oe to -3000 to +3000 by 100 Oe steps, with the sample magnetization measured at each field. The coercive field is identified when the M vs H curve for increasing field matches the M vs H curve for decreasing field, as illustrated in Figure3.5 (b). Typical coercive field for LCMO films at 7K are 1000 Oe for in-plane magnetization, and 2500 Oe for out-of-plane magnetization.

3.2.3 Atomic Force Microscopy

Atomic force microscopy is a scanning probe technique employed to determine surface topography by monitoring the force on a vibrating cantilever tip in proximity with the sample surface, as depicted in Figure 3.7 (a). These forces are dominated by short range van der Waals interactions (with length scale of ∼nanometers) between the tip and sample in conventional atomic force microscopy [51]. In order to measure the force the cantilever experiences, one method involves a laser beam and a photodiode, with the cantilever serving as an intermediate reflective surface between the two. Dynamic atomic force microscopy oscillates the cantilever near its resonant frequency, with the change in the amplitude and the phase shift of the oscillation dependent on the force it experiences. The movement of the cantilever induces a change in the incident light onto the photodiode, providing

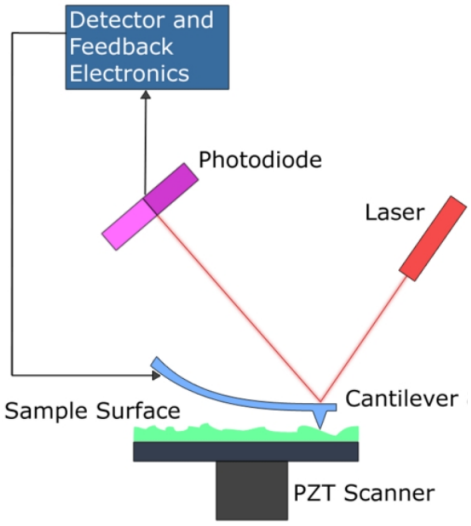

Figure 3.7: AFM schematic diagram. The laser illuminates the cantilever and tip, with the reflected light incident on a photodiode connected to a detector and feedback electronics. The sample surface beneath the AFM tip is translated by the piezoelectric (PZT) scanner, and the change in the resonant frequency of the AFM tip allows detection of the surface morphology.

a means to monitor the force on the cantilever. If the cantilever is brought within range of the van der Waals interaction with the sample surface, and a feedback loop is established to maintain the force the cantilever experiences by varying the cantilever displacement, the cantilever height will mirror that of the sample surface. The tip can then be rastered across the sample surface, and recording the tip height will give the sample topography. The cantilever tip is typically silicon in the [100] orientation, with a radius of curvature as low as 5 nm [51]. The AFM system used for the studies of LCMO and Alq_3 was a Digital Instruments Multi-Mode AFM-2 with a Nanoscope IIIa controller.

Figure 3.8(a) shows a typical topographic image of an annealed LCMO film. The staircase growth mode, where the change in film height between consecutive terraces corresponds to one c-axis lattice constant length of 3.86 angstroms, is a result of miscut of the LSAT substrate. Figure 3.8(b) and (c) shows comparative AFM scans of 10 nm thick Alq_3 films deposited on STO, with the substrate kept at temperature of (b) 20°C and (c) 145°C during deposition. The surface roughness and grain size of the Alq_3 films were reduced by fourfold with heating of the substrate.

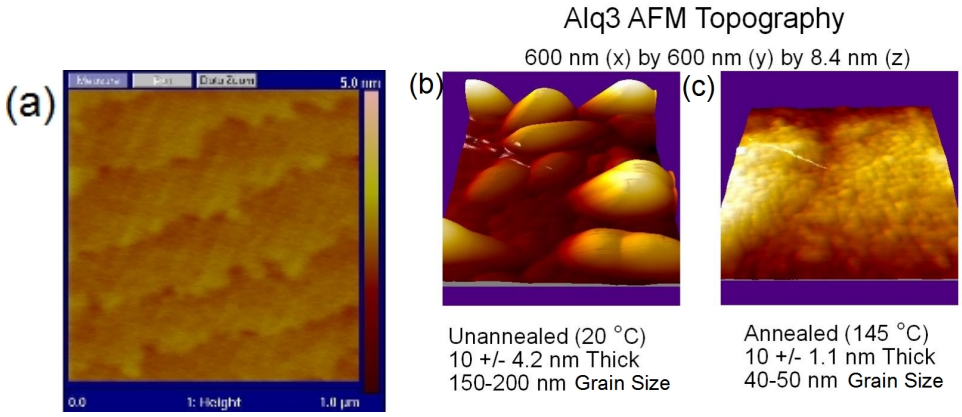

Figure 3.8: (a) AFM scan of LCMO film surface topography with 1.0 μm by 1.0 μm lateral dimensions: (b): 600 nm by 600 nm AFM scans of Alq3 films on STO with unheated substrate during deposition (left), and one heated to 145°C on the right.

Chapter 4

Manganites

4.1 Crystalline Structure and Composition

Manganites are a complex oxide material, first investagted by Jonker and van Santen in 1950 [6]. Infinite layer samples exhibit a chemical formula of $(Re_x,AE_{(1-x)})MnO_{3-y}$, where RE and AE refer to a rare earth (including La, Nd, and Pr) and alkaline earths (Ca, Sr, Be) respectively, and y refers to the oxygen content in the system. Optimal oxygen doping occurs for y=0. The crystal structure is a cubic perovskite structure, typified by the parent compound $LaMnO_3$ in Figure 4.1. Each Mn ion is located at the corner of the unit cell, and is surrounded by an O_6 octehedra, with the rare earth metal in the center of the unit cell. In the parent compound $LaMnO_3$, the valence of Mn-ions is Mn^{3+}, with 4 electrons in the 3d shell. Due to crystal field splitting and the large Hund's energy, the 3d-shell is split into lower-energy t_{2g} orbital and higher-energy e_g orbital, and the spins of all four valence electrons are parallel, with three occupying the t_{2g} orbital and one occupying the e_g orbital, as shown in Figure 4.2(a). The Mn^{3+} is known as a Jahn-Teller ion because the occupation

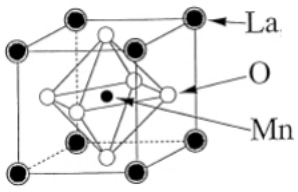

Figure 4.1: Structure of the parent compound $LaMnO_3$. Figure reproduced with permission from Dagotto et al. [12].

of one orbital in the two fold degenerate e_g orbital results in spontaneous symmetry breaking that can further lift the energy degeneracy of the e_g orbital. Upon doping the manganites with divalent alkaline metals, some of the Mn-ions are converted from Mn^{3+} to Mn^{4+}, resulting in a completely empty e_g orbital in the latter. The relevent bands for electron conduction near the Fermi surface are associated with the e_g and t_{2g} orbitals on the Mn ion, and it is sufficient to understand the electronic properties of the manganite compounds by focusing on the behavior of valence electrons located at the Mn ions [12].

Dagotto [12] broadly classifies manganite compounds into 3 types: large bandwidth, represented by $(La_{1-x}Sr_x)MnO_3$, small bandwidth such as $(Pr_{1-x}Ca_x)MnO_3$, and intermediate bandwidth compounds of $(La_{1-x}Ca_x)MnO_3$. The large bandwidth compounds exhibit ferromagnetic ordering and metallic conduction at an elevated Curie temperature T_c above or close to room temperature for appropriate rare earth doping. At the similar hole density, small bandwidth compounds show charge ordering and insulating behavior, with no ferromagnetic phase possible unless stabilized by low temperatures and an applied magnetic field. One explanation for the distinction in the phase and ordering between the two families is the greater hopping amplitude for electrons in the e_g band of the large bandwidth manganites relative to the small bandwidth compounds, due to the larger size of the rare earth ions in the former [12]. The work presented in this thesis will focus on the intermediate bandwidth system of $(La_{1-x}Ca_x)MnO_3$ (LCMO), which exhibits features from both large and small bandwidth families, including the ferromagnetic metal phase of large bandwidth manganites, and charge/orbital ordered phases of the small bandwidth. The interplay of a variety of available phases makes LCMO a system of the greatest complexity and depth of physics for investigation.

The parent compounds of LCMO are $LaMnO_3$ and $CaMnO_3$, and both show antiferromagnetic ordering, although of a different nature. Ordering is type A (ferrimagnetic) for x=0 and consists of Mn^{3+} moments with parallel alignment within the plane and antiparallel between planes (as depicted in Figure4.1), while x=1 yield a type G antiferromagnet with antiparallel spin configuration in all directions. The valency of the Mn ions are Mn^{3+} for $LaMnO_3$ and Mn^{4+} for $CaMnO_3$, and due to strong on-site Coulomb repulsion, the electrons arrange themselves in configuration ${t_{2g}}^3{e_g}^1$ and ${t_{2g}}^3$

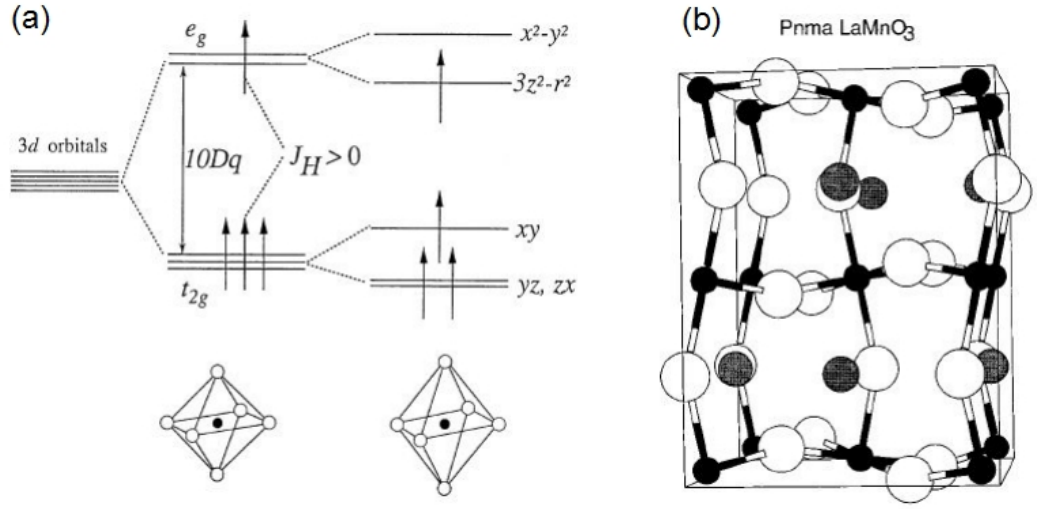

Figure 4.2: (a) Energy levels of Mn^{+3} valency prevalent in $LaMnO_3$. The figure shows from left to center the crystal field splitting of the d orbitals and the energy difference between the e_g and t_{2g} orbitals of 10 Dq. Illustrated center to right is the additional level splitting due to Jahn-Teller distortions. Note that for Mn^{+4}, the $3z^2$-r^2 level is unoccupied, and the absence of energy gain due to Jahn-Teller distortions makes them unfavorable and are not observed. Figure reproduced with permission Dagotto et al. [12]. (b) Changes in Mn-O bond length and angles in a $LaMnO_3$ crystal due to Jahn-Teller distortions. Figure reproduced with permission from Pickett and Singh [5].

respectively (Figure4.2 (a)). The occupation of a t_{2g} in the $LaMnO_3$ ion results in a spontaneous distortion of the Mn-O bond angles and length to lower the orbital energy, a phenomena refered to as the Jahn-Teller distortion (Figure4.2(b)). The Jahn-Teller distortion is absent in $CaMnO_3$ because the e_g orbitals are unfilled. On the other hand, these distortions play a role in electron transport for intermediately doped LCMO compounds.

4.2 Double Exchange Interaction and Other Models

The interplay between pairs of Mn^{+3}-Mn^{+4} ions in the compound plays an important role in electron transport due to the role of oxygen as an intermediary between the Mn ions. Conduction can be considered as two simultaneous events; first, an electron hopping from the O^{-2} ion to Mn^{+4}, and an additional electron hopping simultaneously from the Mn^{+3} to the O^{-2} ion. This effect, known as the "double exchange," was first proposed by Zener in 1951 [52]. Strong ferromagnetic Hund's coupling makes electron hopping most probable when the spins of neighboring Mn ions are parallel,

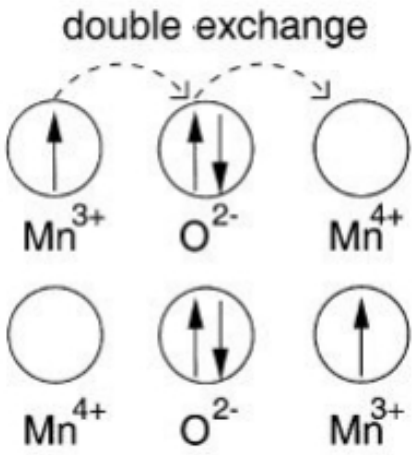

Figure 4.3: The double exchange mechanisms is the simple model for conduction in the manganites. Simulataneous hopping of electrons onto and off the oxygen ion transfers an electron from the intial Mn^{+3} ion to the initial Mn^{+4} ion while maintaining the electron spin orientation. Figure adapted with permission from Dagotto et al. [12]

.

which leads to increased conductivity with the alignment magnetic domains in the manganites. This tendency manifests itself experimentally as colossal magnetoresistance (CMR), or a sizeable reduction in the resistance of the manganites upon application of a magnetic field. Jin et al. in 1994 [7] reported colossal magnetoresistance values in x=0.33 doping LCMO thin films of -127,000% at 77K, and approximately -1300% at room temperature. Here the magnetoresistance is defined as the ratio of [R(0) - R(H)] to R(H), where R(0) and R(H) represent the sample resistance in zero and finite-field H, respectively. The magnitude of magnetoresistance of LCMO greately exceeds those of other superlattice films such as Fe-Cr (approximately -150%), or 80%Ni - 20%Fe permalloy (+3%), and hint at the potential for application of manganite thin films in spintronic devices.

Initial modeling of conduction in manganites as solely due to the double exchange phenomena was found to be inadequate in the 1990s. Estimations of resistivity by Millis et al [53] and computer modeling of resistivity by Calderon et al. [54] both showed inconsitencies in manganite resistivity either below or above T_c. A more complete description of the conduction requires investigating the complete electronic environment of the electrons. Specifically, the full Hamiltonian may be approximated by contributions from five dominant components (following Dagotto et al. [12]): H_{kin},

the kinetic energy of the electrons occupying the e_g orbitals, H_{Hund}, the Hund coupling between the e_g electon spin and the localized t_{2g}-spins, H_{AFM}, the antiferromagnetic Heisenberg coupling between nearest neighbor t_{2g} spins, H_{el-ph}, the coupling between the e_g electrons and the Jahn-Teller distortions of the Mn-O bonds, and H_{el-el}, the Coulombic interactions between the e_g electrons. In total:

$$H = H_{kin} + H_{Hund} + H_{AFM} + H_{el-ph} + H_{el-el}, \tag{4.1}$$

The full Hamiltonian itself is intractable, and necessitates simplification by way of neglecting certain interactions. For example, if the electron-phonon and Coulombic contributions are neglected, in addition to considering only spin degrees of freedom, the so-called double exchange one-orbital model results [55]. If we define s_i as

$$s_i = -t \sum_{\alpha\beta} (a^{\dagger}_{i\alpha} \sigma_{\alpha\beta} a_{i\beta}), \tag{4.2}$$

with $a^{\dagger}_{i\gamma}$ and $a_{i\gamma}$ creation and annihilation operator for an electron at with spin σ at site i, and σ as the Pauli matrices, the Hamiltonian in this "one-orbital model" is

$$H_{DE} = -t \sum_{<i,j>,\sigma} (a^{\dagger}_{i\gamma} a_{j\gamma} + h.c.) - J_H \sum_i s_i \cdot S_j + J_{AF} \sum_{<i,j>} S_i \cdot S_j, \tag{4.3}$$

with S_i the localized "core-spin" of the three electrons occupying the t_{2g} orbitals, J_H the Hund coupling between t_{2g} and e_g orbitals, the J_{AF} the antiferromagnetic Heisenburg coupling between nearest neighbor t_{2g} spins. Even this oversimplification of the physics still proves useful for study, as it is relatively simple and captures competition between ferromagnetic and antiferromagnetic phases. In particular, Monte Carlo simulations by Yunoki et al., using the one orbital model, showed that, with appropriate Hund coupling and dopin,g regions of phase separation between hole rich ferromagnetic and hole poor anitferromagnetic regions are possible [56]. This suggests phase separation in manganites may be intrinsic to the system, instead of solely disorder or defect driven.

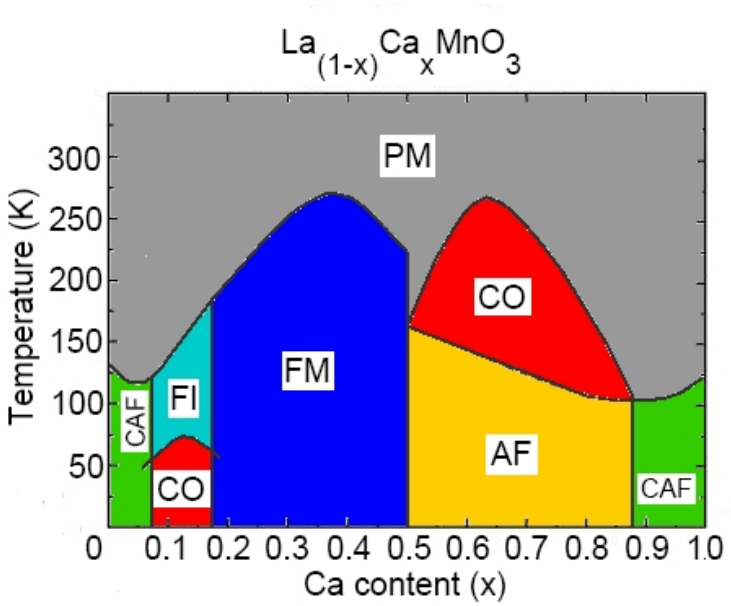

Figure 4.4: Experimental phase diagram of LCMO, plotted with respect to Ca content and temperature. PM signifies paramangetic state, FM ferromagnetic, FI ferromagnetic insulator, AF antiferromagnetic, CAF canted antiferromagnetic, and CO charge ordering. Figure adapted with permission from Dagotto et al. [12].

4.3 Magnetic Phase Diagram

Mixed valence compounds of $(La_{1-x}Ca_x)MnO_3$ show a surprising complex phase diagram (Figure4.4), including charge ordered, antiferromagnetic, spin canted and ferromagnetic metallic and insulating phases. The ferromagnetic metallic phase most studied and of particular interest for applications exists for the doping range of $0.2 \leq x \leq 0.5$. Measurements in the this work focused on x=0.3 thin films, well within the nominally bulk ferromagnetic phase. The LCMO work function for this doping is 4.8 eV [57]. One aspect of particular interest for applications is the half-metallic nature of certain manganite films (LCMO included), where near the Fermi level the density of states in the ferromagnetic phase is almost 100% spin-polarized. This phenomena was first noted theoretically in LCMO by Pickett and Singh [5], where, as we can observe in Figure4.5, the spin majority density of states is metallic, while the spin minority exhibites a band gap for negative energies. Half-metallicity was demonstrated in the manganites with spin-polarized photoemission measurements [9], in addition to STM measurements by the Yeh group [11] [58]. By comparing the spectral characteristics

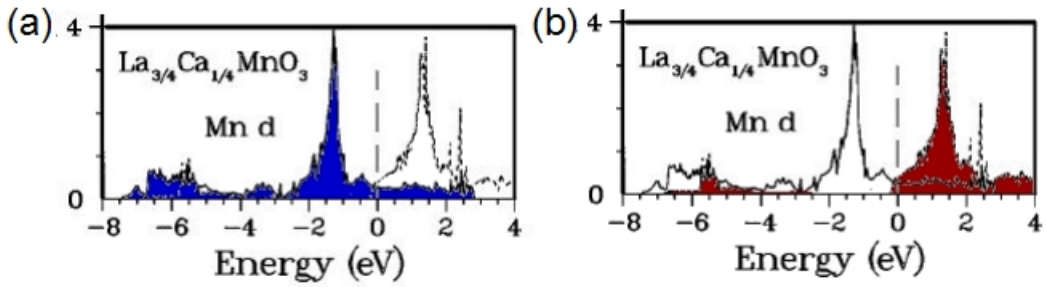

Figure 4.5: Energy-dependent density of states of LCMO with x=0.25 doping. Figure (a) highlights the available states electrons with spin majority in blue, while (b) shows the spin minority states in red. Note the gap in available states for negative energies for the spin minority and the peak in the majority density of states for approximately -1.5 eV, and in the minority density of states for approximately 1.5 eV. Figure adapted with permission from Pickett and Singh [5].

derived from the with band structure calculations for x=0 and x=0.33 [5], the doping level x associated with a LCMO spectrum that exhibits a peak in the density of states at a positive energy U_+ can be extrapolated according to the following relation:

$$x(U_+) = 0.25x(U_+ - 770mV)/(468mV), \tag{4.4}$$

Therefore, by assuming a linear dependence of U_+ on x, the value of U_+ obtained from spectroscopic measurements can be used to estimate the local doping.

Proximate to the ferromagnetic phase and corresponding to a slightly lower range of $0.08 \leq x \leq 0.175$ is the ferromagnetic insulator phase. Algarabel et al. characterized this state for x=0.1 by magnetic and magnetotransport measurements, and noted ferromagnetic behavior of the sample combined insulating conductivity even after magnetic saturation at 12T applied field [17]. This phase is particularily relevent for $La_{0.7}Ca_{0.3}MnO_3$ thin films due to the tendency for Ca to react with CO_2 to form $CaCO_3$ and Ca-deficient non-stoichiometric manganite compounds at the surface, leading to an effectively lower doping surface state than the bulk.

The doping for the LCMO surface is also effected by termination of the crystal. Surface termination has been investigated by Fang and Terakura [59] in $La_{1-x}Sr_xMnO_3$ (LSMO), where the surface termination of the top layer (either MnO_2 or (La,Sr)O planes) changed the effective doping surface layer. In the bulk crystal, one layer of Mn ions is bounded above and below by hole donating

La and/or Sr layer. MnO_2 termination leaves the top-most Mn ions underdoped compared to the bulk due to their proximity to only a single hole donating layer, while (La,Sr)O termination leads to overdoped Mn due to the top layer having only a single Mn layer to donate to. Although the aforementioned calculations were based on a different manganite system LSMO, the La and Ca in LCMO serves the same purpose as the La and Sr in LSMO, and the magnitude of the doping based on layer terminates holds. Furthermore, XPS studies on LCMO [60] suggest that the MnO_2 termination is favored in LCMO, also tending toward an underdoped surface state in proximity with the ferromagnetic insulator phase.

Doping levels that straddle multiple phases (such as x = 0.5) are particularily interesting in the mixture of resulting phases. As depicted in the electron diffraction image in Figure4.6 for x=0.5, the coexistence of metallic (dark) and insulating (light) regions correspond to ferromagnetic and charge/orbitally ordered phases respectively, corroborated by electron diffraction measurements [16]. These orders, while incompatible, exist in domains side by side on the nanoscale; this behavior suggests that at a proximate doping such as x = 0.3 similar behavior can be observed. Indeed, further evidence of inhomogeneity in LCMO in the ferromagnetic doping range is provided by neutron diffraction, NMR, and STM studies. For the x = 0.33 compound, neutron diffraction stuides showed magnetic nanoclusters of $\sim$ 12 angstroms in size to persist until 1.8 T_c [18]. Although initially interpreted as due to magnetic polarons, the authors reviewed their results and argued it implies electronic phase separation. NMR investigations for ^{55}Mn ion also show the coexistence of ferromagnetic insulator phase with the ferromagnetic metal directly below T_c and below 20K, bounding a temperature range that exhibits uniform ferromagnetic behavior for the x = 0.25 doping [19]. Fäth et al. [20] conducted STM measurements on $La_{0.7}Ca_{0.3}MnO_3$ thin films just below T_c of 260K, and in applied magnetic fields up to 9T. Maps of the conductance of the film at 3V bias show at zero field a mixture of metallic and insulating regions, whereas the application of a magnetic field increases the conducting fraction of the film. Furthermore, the authors mention upon cooling the sample has exhibits an increase in the conductivity of the film similar to that of an applied magnetic field, but some regions stay insulating deep into the nominally ferromagnetic metal phase. The phase

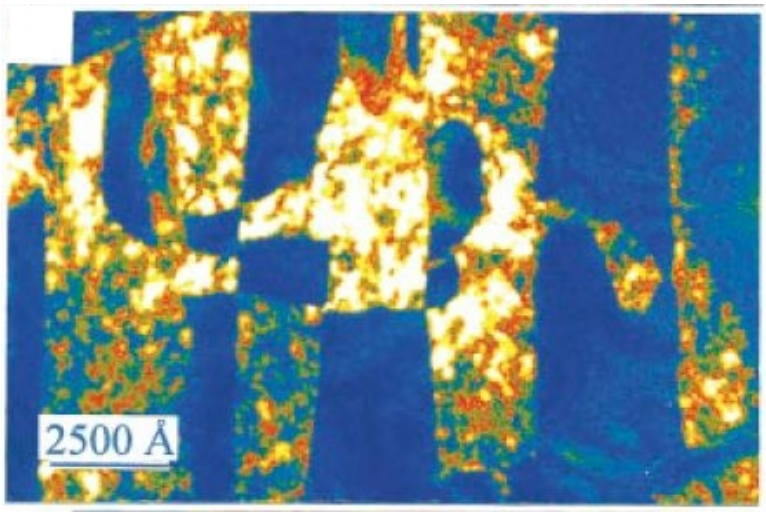

Figure 4.6: Electron diffraction image of LCMO thin film with x = 0.5. Dark regions correspond to highly conductive and ferromagnetic domains, while bright regions are insulators and charge ordered. Figure adapted with permission from Chen and Cheong [16].

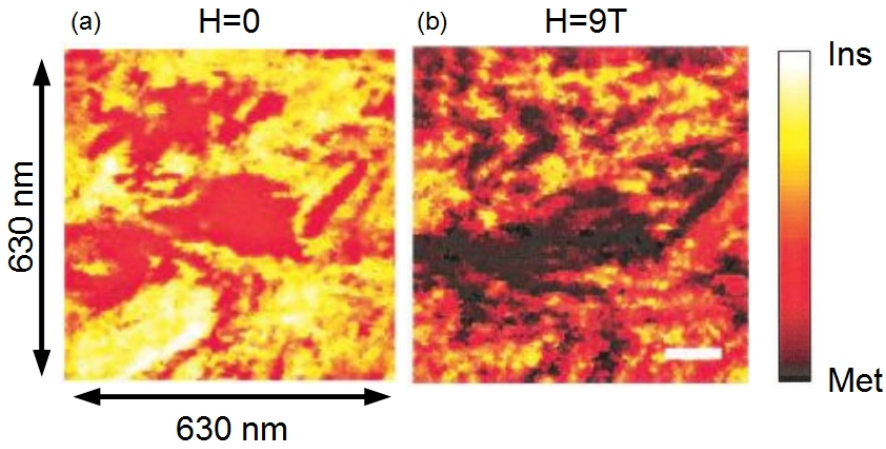

Figure 4.7: Maps of differential conductance of LCMO films at +3V, with darker regions showing higher conductance associated with metallicity under varied applied magnetic field. (a) and (b) shows scans of the same area with 0 and 9T magnetic field respectively. Figures adapted with permission from F*ä*th et al. [20].

inhomogeneity of the film even at low temperatures suggests multiple different orders in the LCMO ground state.

A consequence of mixed phase regions is the suppression of the available and filled states near the chemical potential which is termed as the "psuedo-gap" phenomenon. Moreo et al. conducted Monte-Carlo simulations with both one orbital approach [61] and more advanced models [62], and identified the presence of psuedo-gap under varied doping and temperature ranges, suggesting that the psue-

dogap phenomenon should be a common feature to the manganites. The feature arises from the competition between ferromagnetically ordered clusters and a anti-ferromagnetic or charge/orbital ordering background matrix, not unlike the ferromagnetic insulator discussed previously, and is most easily understood in one-dimensional for low electron doping, as depicted in Figure 4.8(a). The physics for the occurrence of pseudogap may be understood as follows. Due to the large on-site Coulomb repulsion, the potential energy in the ferromagnetic regions is effectively attractive to electrons (Figure 4.8(c)), which leads to a distribution of occupied states below the chemical potential μ, with the detailed distribution dependent on the specific size of the cluster and the strength of the attractive potential ("cluster band"). Likewise, the antiferromagnetic phase contribute to states at an energy above the chemical potential, leading to a suppression of the density of states at the chemical potential.

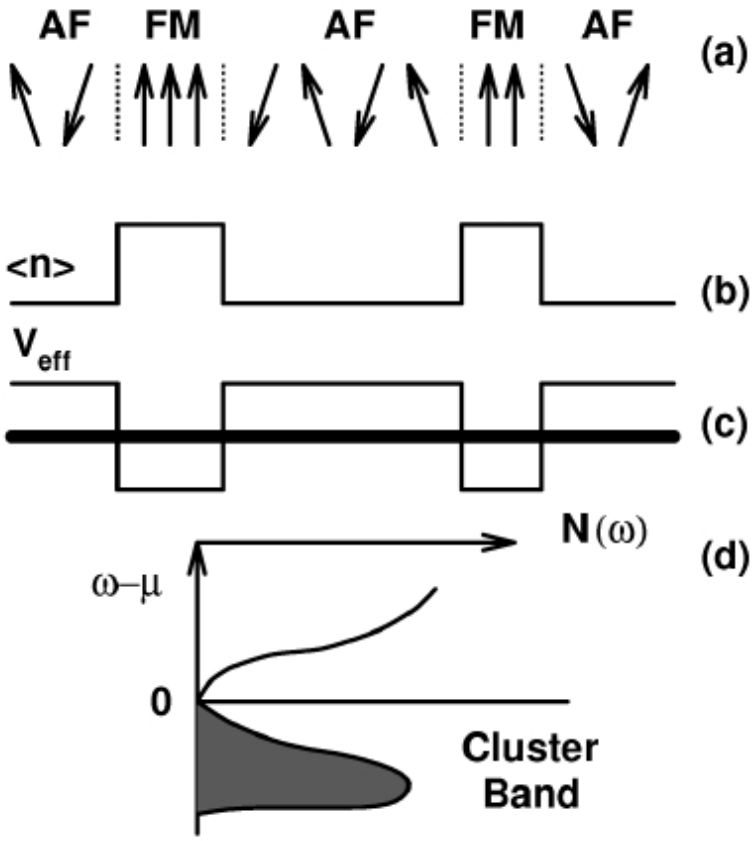

Figure 4.8: (a) The mix of antiferromagnetic and ferromagnetic regions in a quasi-one dimensional manganite. (b) Electron density and (c) effective potential as a function of position. d) Density of states illustrating the cluster band. Image adapted with permission from Moreo et al. [61].

4.3.1 STM Measurments on LCMO

Previous STM measurements on LCMO films predominantly dealt with spectral features at temperatures close to the metal to insulator transition at the Curie temperature(∼260K). For instance, the work by Fäth et al. [20] only reported differential conductance data at 3 volts bias slightly below T_c, without covering in detail the spectral characteristics deep into the nomially FM state. Seiro et al. investigated LCMO films down to liquid helium temperatures and observed a largely uniform low energy gap attributed to polarons, but with a film intentionally prepared by the choice of a substrate ($SrTiO_3$) to be uniformly strained throughout [47]. Indeed, the c-axis lattice constant shows a 1.6% change from the bulk value, with a resulting decrease in Curie temperature to 144K, making it difficult to distinguish whether the properties observed in their film is instrinic to the manganite or stabilized by the strain-induced deformation. Mitra et al. [48] studied a minimally strained x = 0.3 LCMO film and observed uniform film conductance with only a suppression of the density of states near the metal to insulator transition that disappeared upon further cooling, although a gap was observed beneath 40K. Common to all the previously mentioned investigations aside from the work by Fäth et al. is their focus on low energy features of the film, with no explanation of the underlying cause of the insulating gap in the nominally ferromagnetic metal phase or the suppression in the observed density of states.

More detailed STM measurments by the Yeh group [58] [11] investigated x = 0.3 LCMO thin films over a much larger energy range of -4 to +4 eV. Point spectra at 77K identified high energy peaks in the conductance corresponding to the spin majority and spin minority peaks in band structure calculations for the ferromagnetic state(Figure 4.5) [5], which disappeared above T_c. In addition, the presence of low energy insulating gap similar that observed by the aforementioned studies was found below T_c. The insulating gap was also shown to disappear above T_c, although the nature of the gap was not understood in these earlier studies. To fully understand the physical origin for the occurrence of the low-energy gap and the issue of intrinsic electronic heterogeneity in the manganites, detailed spatially resolved spectroscopic studies as functions of temperature and magnetic field are necessary. In the following chapter, elaborate STM investigations of the LCMO

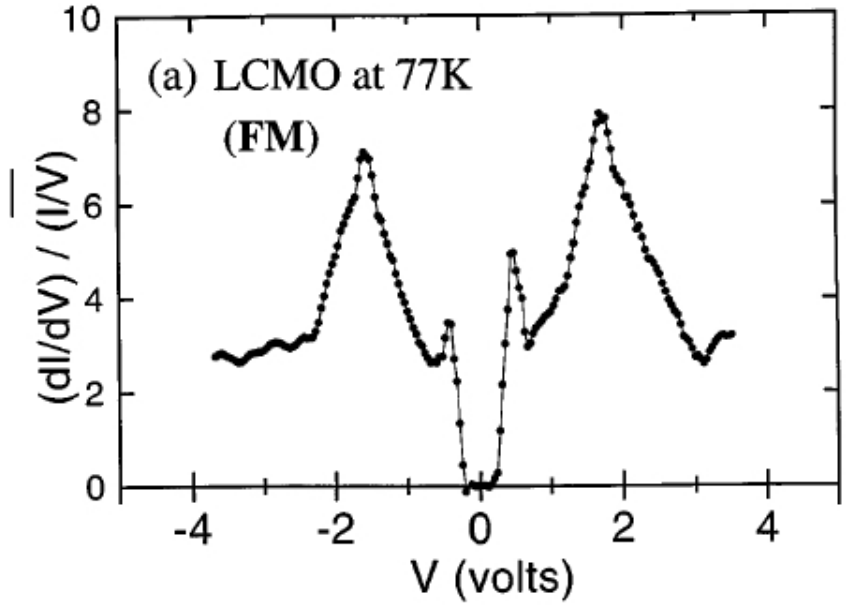

Figure 4.9: STM point spectra for an x = 0.3 LCMO thin film at 77K. Tunneling spectra exhibit both high energy peaks consistent with FM ordering in the sample, and a low energy gap. Image adapted with permission from Wei et al. [11].

system are presented, which provide new insights into better understanding of the aforementioned issues.

Chapter 5

Conductance Inhomogeneity and Competing Orders in LCMO Thin Films

The manganite compound $La_{1-x}Ca_xMnO_3$ (LCMO) with a bulk doping level x=0.3 is a ferromagnetic metal with a relatively high Curie temperature T_c = 270K. This system is promising for spintronic device applications, and may be used as a spin current injector because of the gapped band structure for minority spins, a property known as half-metallicity [5]. On the other hand, as stated in the previous chapter, even in this bulk ferromagnetic metallic phase, inherent electronic inhomogeneity at microscopic scales is expected. To further study this effect, we have investigated x = 0.3 LCMO thin films using scanning tunneling spectroscopy under varied temperature, magnetic field and spin polarization of the tunneling current. Spatially resolved maps of tunneling conductance taken with non polarized Pt/Ir tip show variations on the scale of a few hundred nanometers in size in the bulk ferromagnetic state, which are believed to be the result of intrinsic inhomogeneity of the manganites due to their tendency toward phase separation. Maps of tunneling conductance taken with spin polarized Cr coated tips are consistent with the convolution of the LCMO and Cr density of states, and below the T_c of LCMO the spin polarized tunnel junction can be described as a spin valve configuration. The electronic homogeneity in the material increases above the magnetic ordering temperature, or with application of magnetic field in the bulk ferromagnetic state. We identified gaps in the conductance at two separate characteristic energies. The first gap of energy $\sim$0.6 eV is believed to arise from a ferromagnetic insulator (FI) surface phase due to its disappear-

ance above the Curie temperature (T_c) and the dependence of gap energy on relative tip and sample magnetic orientation. The surface phase may be stabilized by Ca deficiency at the LCMO surface, corroborated by x-ray photoemission spectroscopy (XPS) [63]. Second, we observe a nearly temperature independent and spatially varying gap of ∼0.4 eV for all zero-field tunneling spectra, which is believed to be associated with psuedogap (PG) phenomena discussed in Chapter 4. Application of a magnetic field converts the regions of PG phenomena to FI, in conjunction with an increase in the homogeneity of the film conductance. These findings suggest that the PG phenomena arise from electronic inhomogeneity in the manganite film, in agreement with theoretical investigations [61], and that the vertical and lateral electronic inhomogeneity, along with its dependence on temperature and applied magnetic field, has important implications for use of these materials in high density nanoscale spintronic devices.

5.1 Introduction

"Spintronics" is a new class of electronics incorporating spin dependence in charge transport in magnetic heterostructures [64, 65]. It has emerged as an active research area in recent years because of the potential advantages of non-volatility, faster processing speed, small power dissipation for high device integration densities as opposed to conventional semiconducting devices [64], and better coherence for quantum information technology [65].

In spintronics, it is particularily important to understand spin-polarized quantum tunneling and transport at interfaces and throughout bulk materials for developing high performance and highly reproducible spintronic devices. Ideal candidate materials for use in spintronic devices are ferromagnets with a high degree of spin polarization and higher than ambient Curie temperatures. In this context, the manganese oxides $Ln_{1-x}A_xMnO_3$ (Ln: trivalent rare earth ions, A: divalent alkaline earth ions), also widely known as manganites that exhibit colossal magnetoresistance (CMR) effects, [66, 67, 7, 68, 69, 70] appear to be promising spintronic materials because of their half-metallicity in the ferromagnetic state so that the degree of spin polarization near the Fermi level is nearly 100%. Nonetheless, experimental data and theoretical calculations have suggested that the

ground states of the manganites tend to be intrinsically inhomogeneous as the result of their strong tendencies toward phase separation, and the phase separation may involve domains of ferromagnetic metals, ferromagnetic insulators, and antiferromagnetic charge and orbital ordered insulators [12, 20, 71, 15]. The intrinsic electronic inhomogeneity is relevant to high areal densities fabrication of reproducible miniaturized spintronic devices.

In addition to the tendency toward phase separation in the bulk of the manganites, a number of experimental findings have highlighted differing physics on the surfaces of manganites compared to the bulk characteristics [15], which could be a concern in the fabrication of spintronic devices based on layered heterostructures. For instance, scanning tunneling spectroscopic (STS) studies of the manganite epitaxial thin films [11, 58, 47] and single crystals [71] have revealed a small energy gap near the Fermi surface of the manganites with nominally metallic bulk compositions. Although the occurrence of an energy gap does not appear in either band structure calculations [5] or the bulk electrical transport measurements that revealed metallic behavior in $La_{0.67}Ca_{0.33}MnO_3$ [72, 73], the tunneling spectra over a large energy range except near the Fermi level were in agreement with theoretical calculations of the bulk electronic density of states [11, 58]. Hence, it is reasonable to conjecture that the surface of manganites may consist of a thin insulating layer with regions of differing chemical compositions from those of the bulk. Thus, low-energy ballistic electrons from the STM tip could detect a small surface insulating gap while high-energy ballistic electrons that penetrate further into the bulk could reveal spectroscopic characteristics consistent with the bulk density of states. This conjecture is consistent with x-ray photoemssion spectroscopic (XPS) studies of $La_{0.67}Ca_{0.33}MnO_3$ that suggested surface termination is favored by an insulating layer of MnO_2 [60]. Additionally, XPS studies also revealed that the surface of manganites generally exhibits Ca deficiency compared to its bulk Ca doping level x [63].

Another intriguing feature occuring in manganites is the appearance of the pseudogap (PG) phenomena [12]. Theoretical studies based on Monte Carlo simulations [61, 62] suggest that the density of states (DOS) in the manganites should exhibit PG characteristics that are manifested by a significant spectral depletion at the chemical potential and the presence of DOS peaks with large

linewidths above and below the chemical potential. These theoretical findings have indeed been observed in photoemission experiments for bilayer manganites above magnetic ordering temperatures [74]. Theoretically, the occurrence of PG may be regarded as a precursor of phase separations in forms of magnetic clusters, [61, 62] which is analogous to the widely studied PG phenomena in cuprate superconductors where the appearance of PG has been attributed to the onset of preformed pairs and competing orders [75]. However, the commonality of PG phenomena among different types of manganites and whether the physical origin of PG in the manganites is associated with the onset of mixed phases have not been extensively probed by experiments.

To address the aforementioned issues of phase separations, non-stoichiometry in surface layers and the PG phenomena in the manganites, we report spatially resolved tunneling spectroscopic studies of $La_{0.7}Ca_{0.3}MnO_3$ (LCMO) epitaxial films by means of both regular and spin-polarized scanning tunneling microscopy (STM and SP-STM [45]). The chosen calcium doping level of x=0.3 lies deep within the nominally ferromagnetic phase, with nearly the highest Curie temperature ($T_c \sim 270$ K) and the most spatial homogeneity among the Ca-doped manganites. The evolution of the spatially resolved tunneling spectra was studied systematically with temperature, magnetic field and with the presence and absence of spin polarization, which investigated the spatial scales of both the stoichiometric inhomogeneity and the average size of ferromagnetic domains. Additionally, comparison with band structure calculations suggested that the spectral characteristics taken with regular STM were consistent with those of the density of states of the manganite in the ferromagnetic phase, whereas data taken with SP-STM must be understood in terms of the product of a spin-dependent tunneling matrix and the joint density of states between the SP-STM tip material and the manganite. Moreover, the modification of the surface energy gap with temperature, magnetic field and the amount of spin-polarization was consistent with the spin-filtering effect of a surface ferromagnetic insulating (FI) phase with a Curie temperature closely matching that of the bulk ferromagnetic manganite. The surface phase may originated from a Ca-underdoped surface that yielded a spatially varying ferromagnetic insulating phase for $x < 0.125$ [12, 17]. Finally, PG phenomena were found to continue at temperatures above all magnetic ordering temperatures of the manganites without the

presence of external magnetic fields, and the PG features were suppressed by moderate magnetic fields at low temperatures when the tunneling conductance of LCMO becomes considerably homogeneous. The results presented here therefore provide quantitative experimental accounts at the microscopic scales for the presence of phase separations, surface states and PG phenomena in the manganites. Comparing with other STM studies on manganites, while earlier investigations have demonstrated spatial inhomogeneity in the tunneling spectra spectra in manganites with different doping levels, [20, 71] this work provides the first report of high magnetic field SP-STM studies on the manganites. This work also demonstrates a potentially useful combination of SP-STM techniques and high-field capabilities to the study additional of spatially heterogeneous magnetic materials.

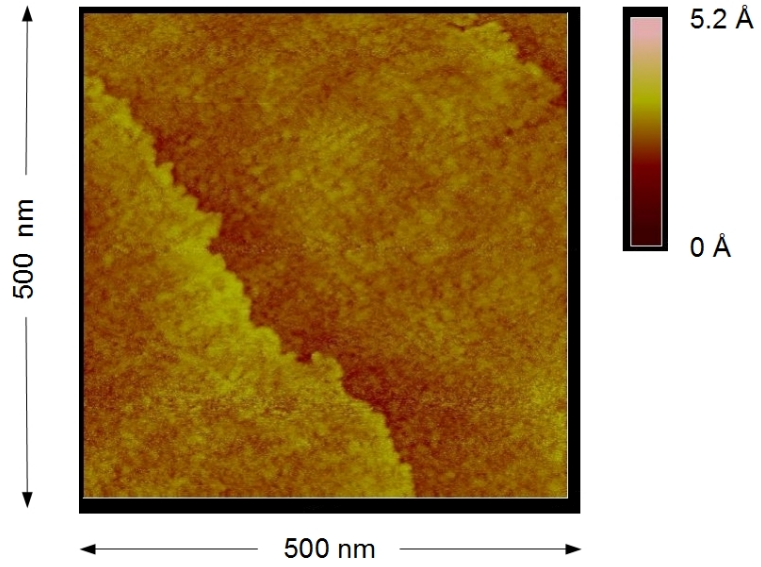

Figure 5.1: Typical STM topography of the LCMO epitaxial film on $(LaAlO_3)_{0.3}(Sr_2AlTaO_6)_{0.7}$ substrate over a (500×500) nm^2 sample area, showing atomically flat surfaces and steps of one lattice constant height.

5.2 Experimental

Detailed accounts of film growth and characterization are discussed in further detail in Chapter 3. The $La_{0.7}Ca_{0.3}MnO_3$ (LCMO) films used in this study were epitaxially grown on $(LaAlO_3)_{0.3}(Sr_2AlTaO_6)_{0.7}$ substrates by means of pulsed laser deposition (PLD) techniques. The substrates were chosen be-

cause of their relatively small lattice mismatch (about 0.3%) with the bulk LCMO, which ensures minimized strain in the resulting films. The films were deposited in a 100 mTorr oxygen background pressure to a thickness of (110 ± 10) nm with the substrate temperature kept at 650°C, and were subsequently annealed at the same temperature for 2 hours in 100 Torr O_2 and then cooled slowly to room temperature. The epitaxy of these films was confirmed by x-ray diffraction, and the film quality was further verified by atomic force microscopy and scanning tunneling microscopy (STM) measurements, showing terraced growth with step heights corresponding to one c-axis lattice constant of the bulk LCMO, as exemplified in Figure 5.1. Further characterizations were conducted using the Superconducting-Quantum-Interference-Device (SQUID) magnetometry measurments, indicating a Curie temperature of 270 ± 10 K. Additionally, the fields required to saturate the magnetization of the LCMO films with magnetic fields perpendicular to the plane of films were determined by the SQUID magnetometer, and were found to range from $H_C^{\mathrm{LCMO}} = 0.05$ T to 0.2 T. We note that similar growth conditions for LCMO films had been shown to yield high-quality epitaxy via high-resolution x-ray diffraction studies, magnetization and transport measurements [72, 73]. Immediately prior to being loaded into the cryogenic STM system, the sample was etched in a 0.5% bromine in pure ethanol solution and then rinsed in pure ethanol to remove surface carbonates. During the STM loading process, the etched sample was kept under excess pressure of helium gas to minimize surface carbonate formation.

The tunneling studies were conducted with our homemade cryogenic UHV scanning tunneling microscope with a base temperature $T = 6$ K and a superconducting magnet capable of magnetic fields up to $H = 7$ T (discussed further in Chapter 2). At $T = 6$ K the STM system was under ultra-high vacuum with a base pressure approximately 10^{-10} mbar. Regular tunneling spectroscopic studies were conducted with atomically sharp Pt/Ir tips, while spin-polarized studies were made by means of Pt/Ir tips evaporatively coated with 30 monolayers of Cr metal prepared in a separate evaporation system, following the procedures reported previously in Chapter 2.9. The magnetic ordering temperature (T_c^{Cr}) of the Cr-coated tip was much higher than room temperature, such that we are justified to assume that electrical currents from the Cr-coated tip was always spin-polarized.

This assumption was indepedently verified by the field dependence of the tunneling conductance, along with estimation of the degree of spin polarization, as elaborated in Section 5.3. The coercive field (H_c^{Cr}) of the Cr-coated tips was experimentally measured to be larger than that of the LCMO samples so that $H_c^{LCMO} \ll H_c^{Cr} < 3.0$ T for all Cr-coated tips.

In the reported studies, the STM system was operated at a temperature of $T = 6$ K for $H = 0$, -0.3 T, and 3.0 T, and also at $T = 77$ K and 300 K for $H = 0$. Both Pt/Ir and Cr-coated tips were employed in the studies, and the field-dependent studies were conducted at below the T_c of both materials and under three magnetic conditions: $H = 0$, $H_C^{LCMO} < |H| < H_C^{Cr}$ with $H < 0$, and $|H| > H_C^{Cr}$ with $H > 0$. These values ensured that the effects of spin-polarized currents were investigated for three different relative tip and sample magnetic orientations: namely, in LCMO, randomly oriented magnetic domains, magnetic domain alignment anti-parallel to the tip magnetic orientation, and magnetic domain alignment parallel to the tip magnetic orientation.

The spectroscopic measurements consisted of a conductance measurement of current I taken from V = -3 V to 3 V at each pixel on a (128 × 128) pixel grid located over a (500 × 500) nm^2 area for the zero-field studies made at 77 K and 300 K. The sample scan area for field-dependent measurements at 6 K was reduced to (90 × 250) nm^2 due to the reduced scanning range of the piezoelectric material at liquid helium temperatures and the experimenters preference to conduct a complete series of three spectroscopic scans without interruptions by liquid helium transfer. Typical junction resistance for all measurements was maintained at $\sim 100M\Omega$. Both tunneling spectroscopy and topography were shown to be independent of alterations of the tip sample separation under this range of junction resistance. For comparison of spectroscopic data taken under different conditions on multiple samples, the conductance to be discussed below were all processed into normalized differential conductance, $(dI/dV)/(I/V) \equiv \bar{G}$, as the effect of variations in the tunnel junction is minimized for this quantity, allowing clearer investigations of material properties.

It was only possible experimentally to keep to an identical sample area for field dependent measurements that were made with a specific STM tip and at a constant temperature, while 300K and 77K measurments were conducted on differing sample areas. Given the intrinsic inhomogeneity

of LCMO, meaningful comparison among the data sets taken under differing experimental conditions could only be made if statistical consistency in the spectral characteristics could be established among data taken from different areas of the same sample or from different samples prepared under the same fabrication conditions. This premise was indeed verified in our investigation, as elaborated further in Section 5.3.

5.3 Results and Analysis

Following the methods outlined in Section 5.2, systematic studies of the tunneling spectral evolution with temperature, magnetic field and spin polarization were carried out to investigate issues of phase separation, surface state and the PG phenomena in the nominally ferromagnetic manganite epitaxial thin films of $La_{0.7}Ca_{0.3}MnO_3$ (LCMO) on $(LaAlO_3)_{0.3}(Sr_2AlTaO_6)_{0.7}$.

5.3.1 Spectral Characteristics

Detailed inspection of the LCMO tunneling spectra over relatively large sample areas and multiple samples with both Pt/Ir and Cr-coated tips at $T = 77$ K ($\ll T_c^{LCMO} \ll T_c^{Cr}$) and $H = 0$ revealed three types of representative tunneling spectra, which we label as α, β, and γ-types. Examples of the α-and β-types of spectra taken with a Pt/Ir tip are shown respectively in Figures 5.2(a) and 5.2(b), and representative spectra of the α-and γ-types taken with a Cr-coated tip are illustrated in Figures 5.2(e) and 5.2(f). We note that all three type of spectra occur for both Pt/Ir and Cr-coated tips.

The dominant α-type of spectra is characterized by four primary features, including two high conductance peaks at opposite energies of $\omega = U_+$ and $-U_-$, and the presence of a low energy insulating gap at the Fermi level bounded by shoulders in the DOS. The α-type of spectra is consistent with previous observations in single-point spectroscopy [11].

In constrast, the β-type spectra as indicated in Figure 5.2(b) shows one pair of peak features at $\omega = U_+$ and $-U_-$ merging with the low energy gap, leading to a higher observed gap value for this type. The γ-type spectra are similar to the β-type spectra except that the corresponding energies

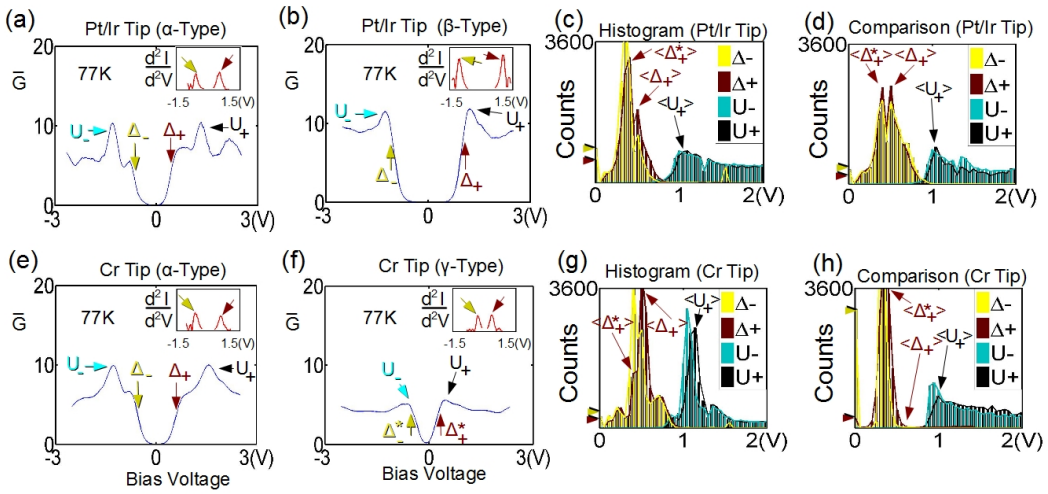

Figure 5.2: Characteristic features in the non-polarized Pt/Ir and spin-polarized Cr tunneling spectra of LCMO taken at $T = 77$ K and $H = 0$: (a) A normalized "α-type" tunneling conductance ($\bar{G}$) spectrum taken with a Pt/Ir tip, showing maximal conductance at $\omega = -U_-$ and $\omega = U_+$ that corresponds to a peak in the density of states associated with the majority and minority bands of LCMO, respectively [5]. Observation of additional features reflecting an insulating energy gap at $\omega = -\Delta_-$ and $\omega = \Delta_+$ is also possible. In all spectra, the values of $\Delta\pm$ are determined by identifying the energies where the second derivatives of the tunneling current I relative to the bias voltage V reach maxima, as indicated in the insets. (b) A normalized "β-type" tunneling conductance spectrum taken with a Pt/Ir tip, showing one set of conductance peaks at $\omega = -U_-$ and $\omega = U_+$ merging with the Δ_- and Δ_+ features. (c) The histograms of the $U_\pm$ and $\Delta_\pm$ energies derived from the each individual tunneling spectra taken with a Pt/Ir tip over a (500×500) nm^2 sample area. Here $\langle U_+ \rangle$ refers to the energy associated with the peak in the LCMO DOS showing the largest count, while Δ_+^* refers to the positive pseudogap energy observed in the γ-type spectra. (d) Energy histograms of $U_\pm$ and $\Delta_\pm$ derived similarily to (c) with a Pt/Ir tip over a same sized area, but from a different sample section, showing statistically similar results. (e) A normalized α-type tunneling conductance spectrum taken with a Cr-coated tip, showing largely similar features to the spectra taken with a Pt/Ir tip with slightly different $U_\pm$ and $\Delta_\pm$ values. (f) A normalized "γ-type" tunneling conductance spectrum taken with a Cr-coated tip, showing pseudogap-like behavior with one pair of relatively low conductance peaks at $\omega = -U_-^*$ and $\omega = U_+^*$ and greately suppressed density of states near $\omega = 0$. Here we use the notation $*$ to represent features associated with the pseudogap-like spectra. (g) Energy histograms of $U_\pm$ and $\Delta_\pm$ derived from the tunneling spectra taken with a Cr-coated tip over a (500×500) nm^2 sample area. (h) Energy histograms of $U_\pm$ and $\Delta_\pm$ derived similarily to (c) with a Cr over a same sized area, but from a different sample section, showing statistically similar results.

$U_{\pm}^{*}$ associated with the peak features and the tunneling gap are much smaller than those found in the β-type, as shown in Figure 5.2(f). We find that the tunneling gap in the γ-type spectra is essentially a pseudogap, showing a suppressed DOS at low energies which only vanishes at the Fermi level.

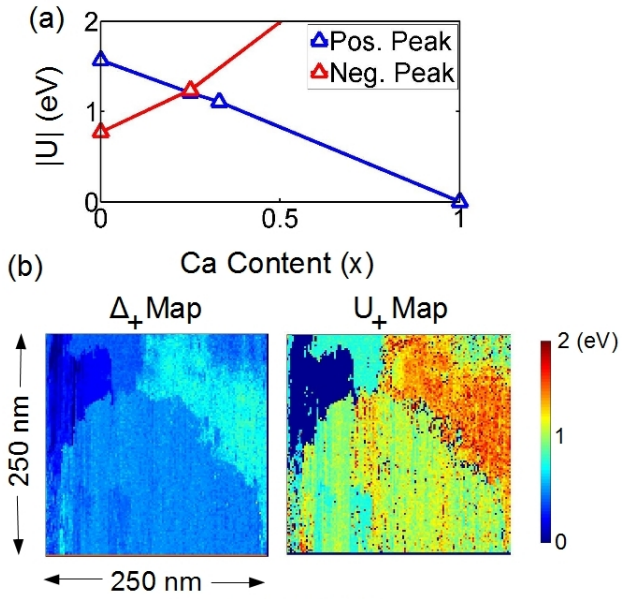

Figure 5.3: (a) Doping (x) dependence of the DOS peak energies $U_{\pm}$ based on a series of band structure calculations [5], showing increasing U_{-} and decreasing U_{+} with increasing Ca doping. (b) The correlation between U_{+} and Δ_{+} values is revealed by simulataneous comparison of the spatial distribution of the DOS peak energy U_{+} and of the positive gap Δ_{+} over the same (500×500) nm^2 77K Cr tip sample area.

For consistent comparison of tunneling gap values among the three types of spectra, we associate $\Delta_{\pm}$ with the energies where the derivative of the tunneling conductance reach a maximum, as shown in the insets of Figures 5.2(a), 5.2(b), 5.2(e) and 5.2(f). The histograms for all four characteristic energies are displayed in Figures 5.2(c) and 5.2(d) for spectra taken with Pt/Ir-tips over two different (500×500) nm^2 areas, and in Figures 5.2(g) and 5.2(h) for spectra taken with Cr-coated tips over two different (500×500) nm^2 areas. The observed spatial variations in the characteristic energies are reflections of the intrinsic inhomogeneity of the manganites, even at the most metallic and uniform LCMO doping considered in this work. Additionally, for each spectral type shown in Figure 5.2, the energies of maximal peak counts, denoted by $\langle U_{\pm} \rangle$, appears to correlate well with the gap values of maximal counts, $\langle \Delta_{\pm} \rangle$. Such correlation suggests that the spatial variations in $U_{\pm}$ and $\Delta_{\pm}$ have

a similar physical origin. In contrast, while the features of each spectral type taken with Pt/Ir and Cr-coated tips were qualitatively similar, as exemplified in Figures 5.2(a) and 5.2(e) and also manifested by the histograms shown in Figures 5.2(c) and 5.2(g), and Figures 5.2(d) and 5.2(h), careful inspections of the distribution of spectral features reveals quantitative differences. These differences may be traced to the band structure of Cr, which will be discussed further in Section 5.3.3.

According to band structure calculations [5], the values of $U_{\pm}$ in the bulk DOS of LCMO extrapolate linearly with the Ca doping level, making them well defined for a given x, as illustrated in Figure 5.3(a). Therefore, the broad range of $U_{\pm}$ values displayed in the histograms in Figures 5.2(c), 5.2(d), 5.2(g) and 5.2(h) suggest spatial variation in Ca doping levels, with two dominate values of local Ca doping corresponding to $x \sim 0.25$ and $x \sim 0.2$. Here we have estimated the Ca doping level by considering the linear extrapolations of $U_{\pm}$ values from band structure calculations. Additionally, the apparent correlation between the maps of U_{+} and Δ_{+} over the same (500×500) nm^2 77K Cr sample area, as shown in Figure 5.3(b), suggests a common physical origin for the spatial variations in the two energies. Essentially, intrinsic electronic inhomogeneity in the manganites leads to observations of spectral variations in the ferromagnetic bulk state in zero field.

It should be noted that the sample areas are not identical when investigated with different STM tips and at different temperatures. This is not an issue for measurements taken with a specific STM tip at the same temperature and under different magnetic fields, as the sampling area may be kept constant. Thus, for consistent comparison of the spectral evolution with temperature and spin polarization, it is necessary to establish the statistical consistency of the spectral characteristics obtained from one (500×500) nm^2 as compared to another area of the same sample. Additionally, it is also necessary to establish the similarity of the statistical distributions across multiple samples prepared under similar fabrication conditions. In this context, we show in Figures 5.2(c), 5.2(d), 5.2(g) and 5.2(h) the histograms of $U_{\pm}$ and $\Delta_{\pm}$ obtained from the tunneling spectra on different sample areas at 77 K with Pt/Ir and Cr-coated tips. The similarities of Figure 5.2(c) to Figure 5.2(d) and Figure 5.2(g) to Figure 5.2(h) establish that the spectral characteristics over a (500×500) nm^2

area appear to be statistically consistent for data taken with the same type of STM tips and at the same temperature, even though the sample areas may differ.

5.3.2 Temperature Dependence

At 300K, the LCMO epitaxial thin films studied are above T_c and exist in the paramagnetic phase, leading to significantly different spectral characteristics from those observed in the bulk ferromagnetic state at $T = 77$ K. This is reflected in Figures 5.4(a)-(b) and 5.4(d)-(e) for exemplified spectra taken at 300 K and with Pt/Ir and Cr-coated tips, respectively. Comparison of Figures 5.4(a)-(b) and 5.4(d)-(e) with Figures 5.4(a)-(b) and 5.4(e)-(f) indicate several important developments with the change in temperature. First, the large $U_{\pm}$ peaks in the DOS for ferromagnetic LCMO became much suppressed in the paramagnetic state. Second, the surface insulating gap found around the Fermi level at 77 K either evolved into a pseudogap (Figures 5.4(a) and 5.4(d)) or completely disappeared (Figures 5.4(b) and 5.4(e)). These observation are corroborated by the histograms of the insulating gap $\Delta_{\pm}$ in Figures 5.4(c) and 5.4(f), where the large number of counts at both zero and the pseudogap energies $\langle \Delta_{+}^{*} \rangle$ are shown. The disappearing insulating gaps at 300 K for selected spectra cannot be accounted for by thermal smearing, and are therefore suggestive of a magnetic phase transition occurring at a mean transition temperature between 77 K and 300 K. In contrast, the nearly temperature independent pseudogap energies are suggestive of a completely separate physical origin for the pseudogap. Third, slight variations in the spectra were found between those taken with the Pt/Ir tip and those taken with the Cr-coated tip at 300 K, as manifested in Figures 5.4(a)-(b) and 5.4(d)-(e). The spectral differences between different tip types can be accounted for because spectra taken with the Pt/Ir were representative of the DOS of LCMO in the paramagnetic phase, whereas those taken with Cr coated consisted of convoluted DOS of paramagnetic LCMO and magnetic Cr-coated tip.

Spatial variations in the characteristics of the spectra with temperature were also accompanied by the temperature-dependent evolution of the spatial variation in the tunneling conductance. The tunneling conductance in the paramagnetic state was generally more homogeneous than that in

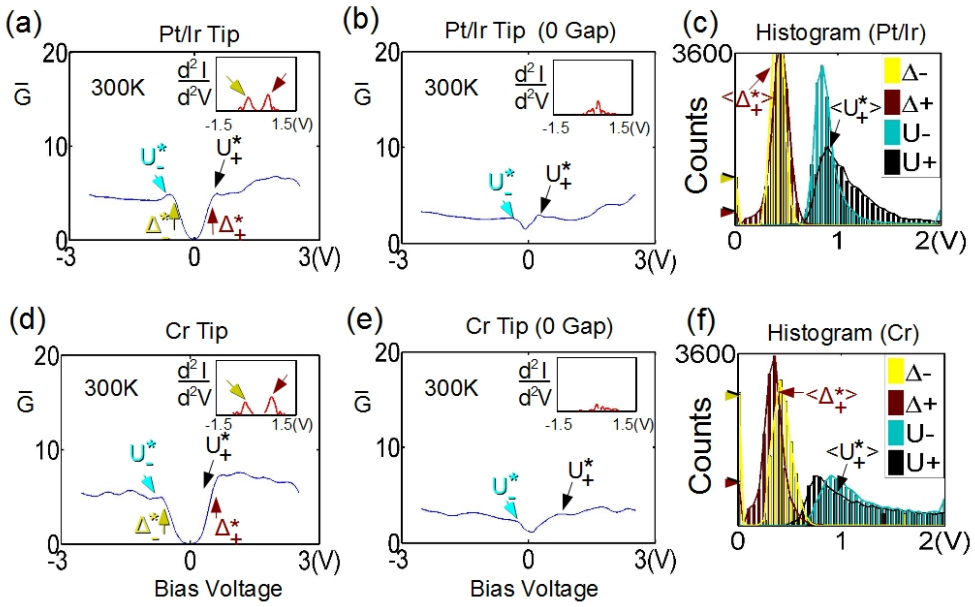

Figure 5.4: Comparison of the normalized tunnel conductance ($\bar{G}$) spectral characteristics taken with Pt/Ir and Cr-coated tips at $T = 300$ K and $H = 0$. (a) A psuedogap-like spectrum taken with a Pt/Ir tip, showing greately suppressed $U^*_\pm$ values relative to the peak energies $U_\pm$ found in the spectrum of Figure 5.2(a). The psuedogap values $\Delta^*_\pm$ are determined from the maximum of the (d^2I/dV^2)-vs.-V spectrum, as displayed in the inset. (b) Another spectral type taken with a Pt/Ir tip, showing a non zero conductance at the Fermi level and vanishing insulating gap, as shown in the inset. (c) Histograms of the insulating gap values $\Delta_\pm$ and the peak energies $U^*_\pm$ obtained by using a Pt/Ir tip over a (500×500) nm^2 area at 300 K, showing greately decreased $U^*_\pm$ values relative to the $U_\pm$ values found at 77 K, as well as large population of vanishing insulating gaps (shown by the arrows at $\omega = 0$) and pseudogaps at $\omega = \langle\Delta^*_\pm\rangle$. (d) A typical pseudogap-like spectrum taken with a Cr-coated tip, showing greately decreased $U^*_\pm$ values relative to the peak energies $U_\pm$ found in the spectrum of Figure 5.2(e). The pseudogap values $\Delta^*_\pm$ are determined from the maximum of the (d^2I/dV^2)-vs.-V spectrum. (e) An additional typical type of spectra taken with a Cr tip, showing vanishing insulating gaps as detailed in the inset. (f) Histograms of the insulating gap values $\Delta_\pm$ and the characteristic energies $U^*_\pm$ obtained by using a Cr-coated tip over a (500×500) nm^2 area at 300 K, showing decreased $U^*_\pm$ values relative to the $U_\pm$ values found at 77 K, as well as a large population of vanishing insulating gaps (shown by the arrows at $\omega = 0$) and pseudogaps at $\omega = \langle\Delta^*_\pm\rangle$.

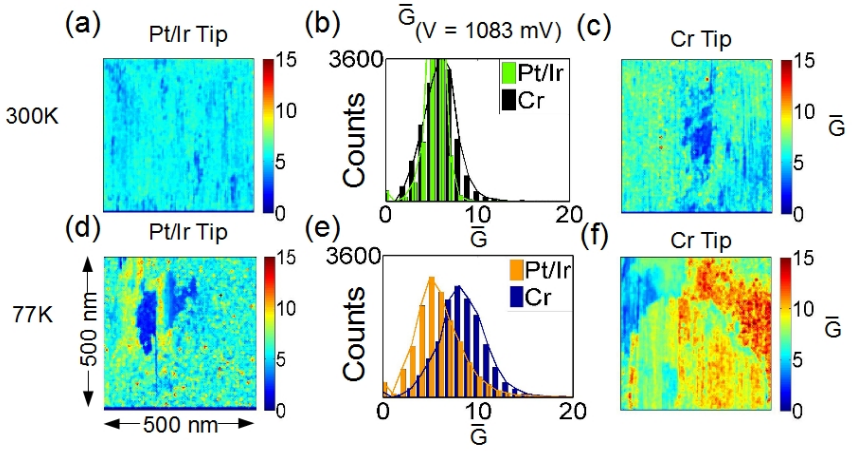

Figure 5.5: Comparison of the high-bias normalized tunnel conductance ($\bar{G}$) spectral characteristics taken with Pt/Ir and Cr-coated tips at $H = 0$ for T=77K and 300K: (a) A (500×500) nm^2 tunneling conductance map taken with a Pt/Ir tip at $\omega = \langle U_+ \rangle$ and 300 K. (b) Histograms of the tunneling conductance obtained by using a Pt/Ir tip and a Cr-coated tip at 300 K and evaluated for $\omega = \langle U_+ \rangle$. (c) A (500×500) nm^2 tunneling conductance map taken with a Cr-coated tip at $\omega = \langle U_+ \rangle$ and 300 K. (d) A (500×500) nm^2 tunneling conductance map taken over a different sample area as (a) with a Pt/Ir tip at $\omega = \langle U_+ \rangle$ and 77 K. (e) Histograms of the tunneling conductance obtained by using a Pt/Ir tip and a Cr-coated tip at 77 K and for $\omega = \langle U_+ \rangle$.(f) A (500×500) nm^2 tunneling conductance map taken over a different sample area as in (b) with a Cr-coated tip at the characteristic energy $\omega = \langle U_+ \rangle$ and 77 K.

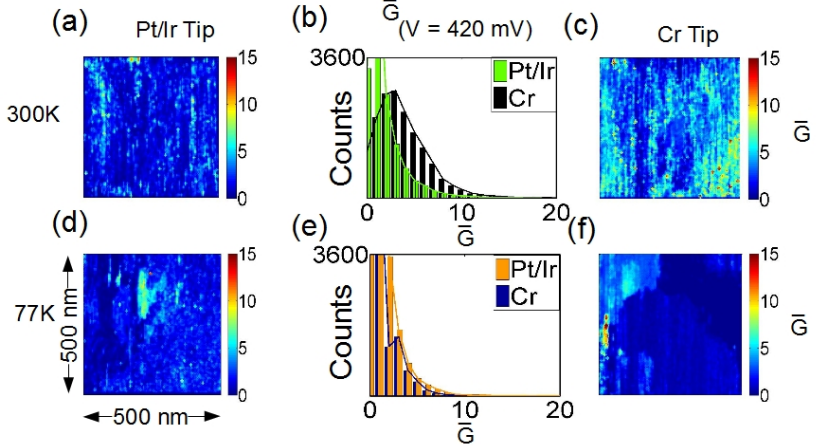

Figure 5.6: Comparison of the low-bias normalized tunnel conductance ($\bar{G}$) spectral characteristics taken with Pt/Ir and Cr-coated tips at $H = 0$: (a) A (500×500) nm^2 tunneling conductance map taken with a Pt/Ir tip at $\omega = \langle \Delta_+^* \rangle$ and 300 K. (b) Histograms of the tunneling conductance obtained by using a Pt/Ir tip and a Cr-coated tip at 300 K for $\omega = \langle \Delta_+^* \rangle$. (c) A (500×500) nm^2 tunneling conductance map taken with a Pt/Ir tip at $\omega = \langle \Delta_+^* \rangle$ and for $T = 77$ K. (d) Histograms of the tunneling conductance obtained by using a Pt/Ir tip and a Cr-coated tip at 77 K and for $\omega = \langle \Delta_+ \rangle$. (e) A (500×500) nm^2 tunneling conductance map taken with a Cr-coated tip at the characteristic energy $\omega = \langle \Delta_+ \rangle$ and for $T = 77$ K.

the ferromagnetic state due to the tendency toward phase separation in the ferromagnetic state of LCMO, as reflected by the constant-bias tunneling conductance maps in Figures 5.5(a) and 5.5(c) for room temperature spectra taken at $\omega = \langle U_+ \rangle$ with the Pt/Ir and Cr-coated tips, respectively. In contrast, the tunneling conductance upon cooling the sample into the ferromagnetic state developed significantly more heterogenity, as shown in Figures 5.5(d) and 5.5(f) for tunneling conductance taken at 77 K and for $\omega = \langle U_+ \rangle$. Here $\langle U_\pm \rangle$ are defined as the most prevalent $U_\pm$ value observed in the histograms in Figures 5.2(c)-(d) and 5.2(g)-(h). The statistical distributions of the conductance at $\omega = \langle U_\pm \rangle$ for 77 K and 300 K are summarized by the histograms in Figures 5.5(b) and 5.5(e) respectively for spectra taken with both the Pt/Ir and Cr-coated tips. While the histograms at 300 K showed statistical similarity between spectra taken with Pt/Ir and Cr-coated tips as demonstrated in Figure 5.6(b), at 77 K the tunneling conductance distributions shift to higher values for spectra taken with the Cr-coated tip as compared with those measured with the Pt/Ir tip. The apparent differences between the histograms obtained with Pt/Ir and Cr-coated tips from LCMO at 77 K can be accounted for by the spin-polarized nature of the tunnel current from the Cr tip into spatially inhomogeneous LCMO in its ferromagnetic phase vs the non-polarized Pt/Ir tip tunnel current.

Similarly, the tunneling conductance maps for $\omega = \langle \Delta_+ \rangle$ taken at 300 K with Pt/Ir and Cr-coated tips are shown in Figures 5.6(a) and 5.6(c), respectively, whereas those for $\omega = \langle \Delta_+ \rangle$ taken at 77 K with Pt/Ir and Cr-coated tips are shown in Figures 5.6(d) and 5.6(f). These maps again reveal more spatial inhomogeneity in the tunneling conductance in the ferromagnetic state as compared to the paramagnetic state. For completeness, the statistical distributions of the tunneling conductance at $\omega = \langle \Delta_+^* \rangle$ for $T = 300$ K and $\omega = \langle \Delta_+ \rangle$ for $T = 77$ K are summarized by the histograms in Figures 5.6(b) and 5.6(e). Here $\langle \Delta_+ \rangle$ denotes the most commonly occurring insulating gap value at positive bias from Figures 5.2(c)-(d) and 5.2(g)-(h) for $T = 77$ K, and $\langle \Delta_+^* \rangle$ represents the most commonly found pseudogap values from Figures 5.4(c) and 5.4(f) for $T = 300$ K.

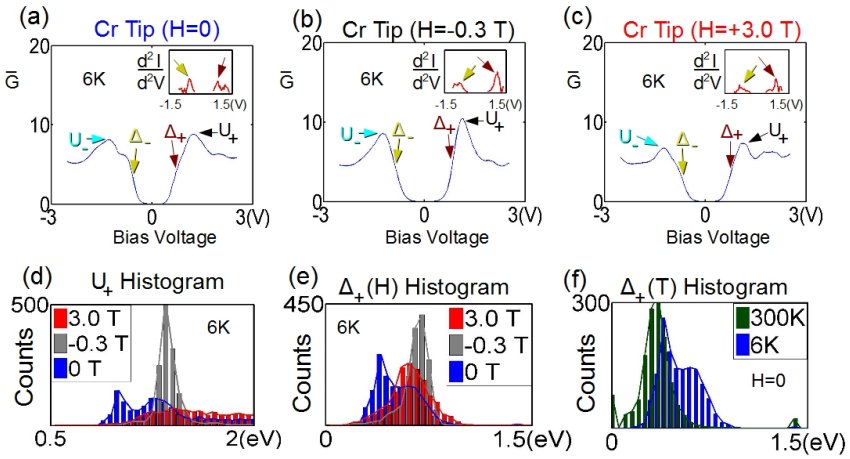

Figure 5.7: Comparison of magnetic field-dependent spectral characteristics taken over the same sample area with a Cr-coated tip at $T = 6$ K: (a) Normalized conductance $(dI/dV)/(I/V)$ $(\bar{G})$ vs. energy for $H = 0$. (b) Normalized conductance vs. energy for $H = -0.3$ T. (c) Normalized conductance vs. energy for $H = 3.0$ T. (d) Histograms of the characteristic energy U_+ over the same (90×250) nm^2 sample area for $H = 0$, -0.3 T and 3.0 T. (e) Histograms of Δ_+ over the same (90×250) nm^2 sample area at $H = 0$, -0.3 T and 3.0 T. (f) Temperature evolution of the histograms of Δ_+ over a (90×250) nm^2 sample area at $H = 0$, showing shift of insulating gap values downward with increasing temperature. In particular, two types of gap values at 6 K may be attributed to an insulating surface gap and a pseudogap, while only the psuedogap persists at 300 K.

5.3.3 Magnetic Field Dependence

Although differences between the tunneling spectra taken with Pt/Ir tips and those taken with Cr-coated tips are readily visible at $H = 0$ and for $T < T_c^{LCMO} < T_c^{Cr}$, additional magnetic field dependent investigations are necessary to further investigate the spin-polarized tunneling into LCMO. As described previously, the degree of spin polarization may be controlled by keeping $T < T_C^{LCMO}$ and by applying magnetic fields of opposite direction with magnitudes satisfying either the condition $H_c^{LCMO} < |H| < H_c^{Cr}$ or $|H| > H_c^{Cr}$. The applied fields $H = -0.3$ T and $H = 3.0$ T chosen satisfy these conditions.

In Figures 5.7(a)-(c) representative normalized spectra taken with Cr-coated tip and at $T = 6$ K are shown for $H = 0$, -0.3 T and 3.0 T. The magnetic field-induced evolution in the tunneling spectra is easily identified, and is reflected in the statistical field-dependent spectral evolution for a (90×250) nm^2 sample area summarized by the histograms of the characteristic energies $U_\pm$ and $\Delta_\pm$ in Figures 5.7(d)-(e). Furthermore, the normalized tunneling conductance map also exhibited

significant alteration with applied field, as exemplified in Figures 5.8(a)-(c) and in Figures 5.9(a)-(c) for spatially resolved tunneling conductance maps at the characteristic energies U_+ and Δ_+, respectively, and for $H = 0$, -0.3 T and 3.0 T over the same (90×250) nm^2 sample area. Specifically, the application of magnetic field converts the spatially inhomogeneous conductance map at $H = 0$ and for $\omega = \langle U_+ \rangle$ to a greater homogeneity map in finite fields, reaching the overall highest conductance for $H = -0.3$ T, as reflected statistically by the histograms of conductance in Figures 5.8(a)-(c) for $H = 0$, -0.3 T and 3.0 T. Additionally, all conductance maps taken at $\omega = \langle U_+ \rangle$ appear to correlate with those at $\omega = \langle \Delta_+ \rangle$ when we compare Figures 5.8(a)-(c) with Figures 5.9(a)-(c).

To further understand the effect of a spin-polarized tunneling current for spectra taken with a Cr-coated tip, similar magnetic field-dependent spectroscopic studies were conducted under the same experimental conditions using a Pt/Ir tip. The representative tunneling spectra taken with a Pt/Ir tip at $T = 6$ K and for $H = 0$, -0.3 T and 3.0 T are shown in Figures 5.10(a)-(c). In comparison with the Cr tip case, the Pt/Ir tunneling spectra exhibited an fundamentally different field-dependent evolution, as demonstrated statistical by the histograms of the characteristic energies U_+ and Δ_+ in Figures 5.10(d)-(e). In particular, we note that the histograms of U_+ showed a monotonic shift to higher energies with increasing applied magnetic field. The insulating gap values Δ_+ showed a similar shift monotonically to higher energies accompanied by sharpened distributions with the magnitude of increasing magnetic field. The spectral characteristics obtained with Pt/Ir tips are then independent of the direction of the applied magnetic field, and solely dependent on the magnitude of applied fields. This findings contrasted sharply with the Cr-coated tip case, which, due to the spin polarization of the tunneling current, showed strong dependence on the direction of the applied magnetic field. Additionally, the tunneling conductance taken with Pt/Ir tips at $\omega = \langle U_+ \rangle$ generally increases with increasing magnetic field, as exemplified by the conductance maps in Figures 5.11(a)-(c) for $H = 0$, -0.3 T and 3.0 T and also summarized by the conductance histograms in Figure 5.11(d). The combination of overall increasing conductance and spatial homogeneity at $\omega = \langle U_+ \rangle$ with increasing magnetic field is consistent with the colossal magnetoresistive effect in the manganites, as increased mobility and alignment of magnetic domains with application of magnetic fields enhances

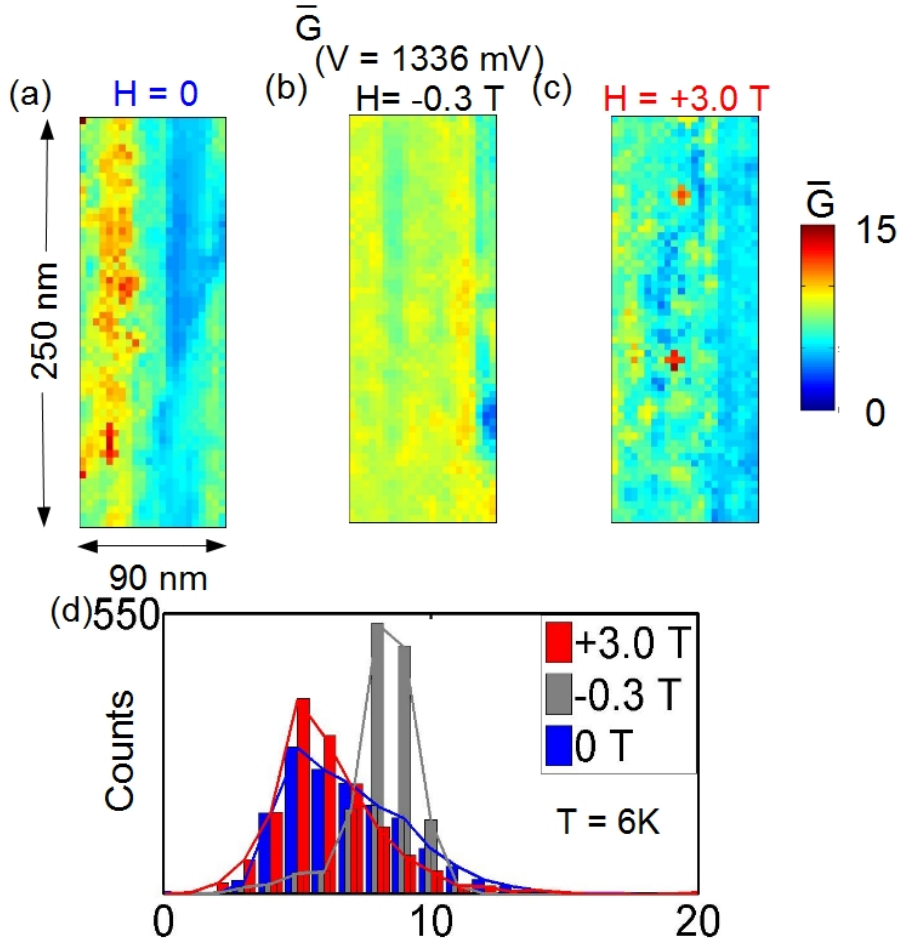

Figure 5.8: Comparison of magnetic field-dependent high-bias normalized conductance ($\bar{G}$) maps taken over a (90×250) nm^2 sample area with a Cr-coated tip at $T = 6$ K: (a) Normalized conductance map taken at $\omega = \langle U_+ \rangle$ and for $H = 0$. (b) Normalized conductance map taken at $\omega = \langle U_+ \rangle$ and for $H = -0.3$ T. (c) Normalized conductance map taken at $\omega = \langle U_+ \rangle$ and for $H = 3.0$ T. (d) Histograms of the normalized conductance at $\omega = \langle U_+ \rangle$ and for $H = 0$, -0.3 T and 3.0 T, showing the overal highest mean conductance at $H = -0.3$ T when the spin-polarization of the Cr tip and the tunneling current is antiparallel to the magnetization of LCMO.

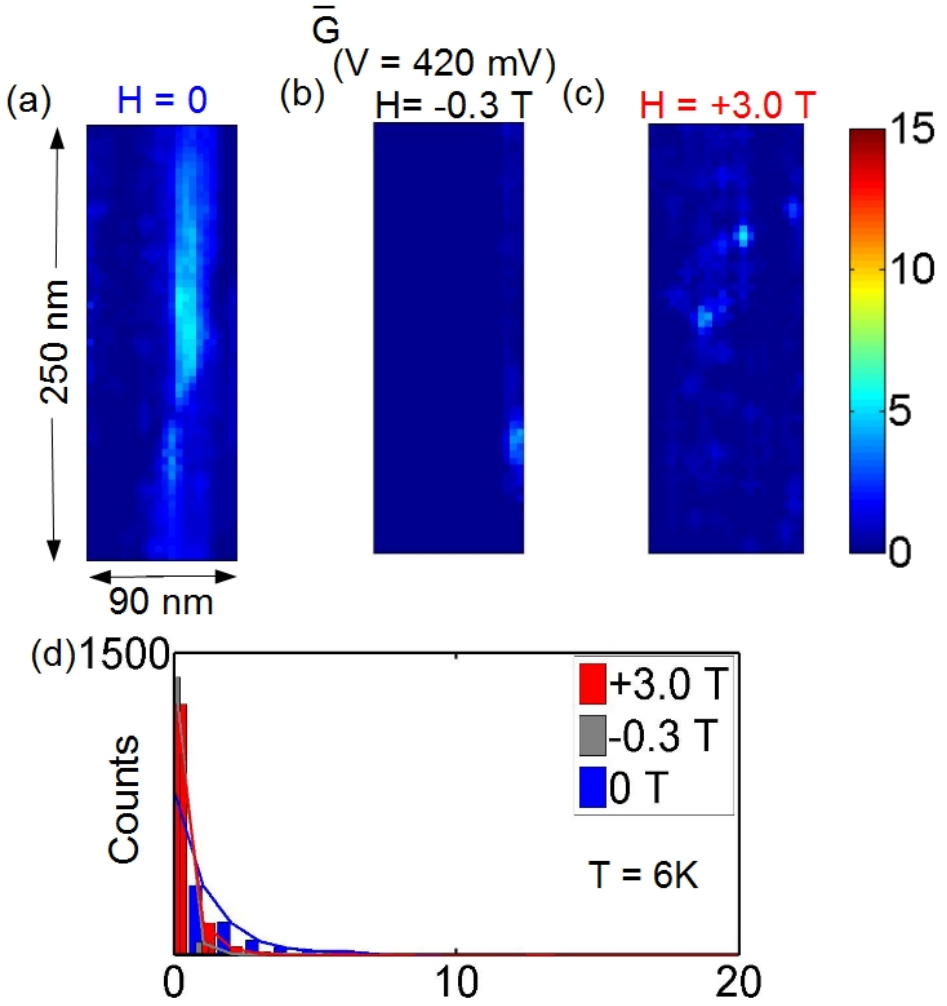

Figure 5.9: Comparison of magnetic field-dependent low-bias normalized conductance ($\bar{G}$) maps taken over a (90×250) nm^2 sample area with a Cr-coated tip at $T = 6$ K: (a) Normalized conductance map taken at $\omega = \langle\Delta_+\rangle$ and for $H = 0$. (b) Normalized conductance map taken at $\omega = \langle\Delta_+\rangle$ and for $H = -0.3$ T. (c) Normalized conductance map taken at $\omega = \langle\Delta_+\rangle$ and for $H = 3.0$ T. (d) Histograms of the normalized conductance at $\langle\Delta_+\rangle$ at $H = 0$, -0.3 T and 3.0 T, showing lowest mean conductance at $H = -0.3$ T when the spin-polarization of the Cr tip and tunneling currents is antiparallel to the magnetization of LCMO.

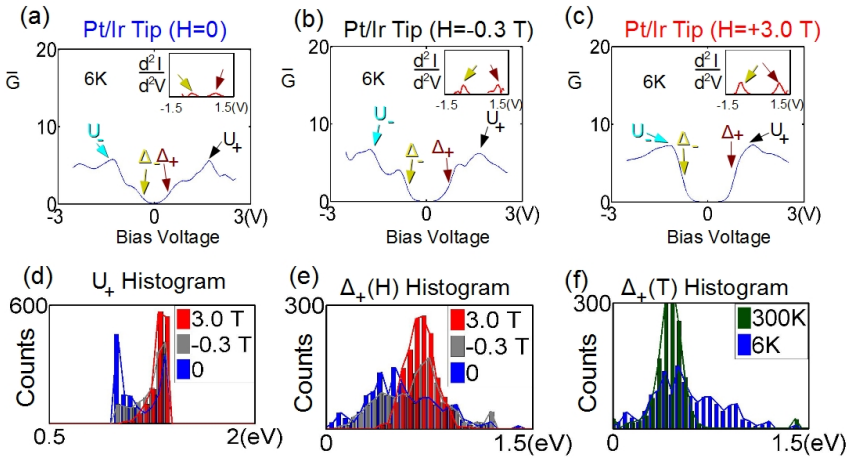

Figure 5.10: Comparison of magnetic field-dependent spectral characteristics taken with a Pt/Ir tip at $T = 6$ K: (a) Normalized conductance $\bar{G} \equiv (dI/dV)/(I/V)$ vs. energy (ω) spectrum for (a) $H = 0$, (b) $H = -0.3$ T and (c) $H = 3.0$ T. (d) Histograms of the characteristic energies $U_{\pm}$ obtained from the same (90×250) nm^2 sample area under $H = 0$, -0.3 T and 3.0 T. (e) Histograms of surface gap energies $\Delta_{\pm}$ obtained from the same (90×250) nm^2 sample area under $H = 0$, -0.3 T and 3.0 T.

electrical conductance across different magnetic domains of the manganites. The increasing spatial homogeneity in the conductance observed with increasing magnetic field also agrees with previous STS reports on LCMO, [20] although previous reports focused on tunneling conductance studies at alternate bias voltages much closer to the sample Curie temperature.

In addition to the evolution of the ferromagnetic bulk tunneling conductance, examination of the change in surface gap energies in spectra taken with a Pt/Ir tip with application of magnetic field also provides insight into the origin of the gap. As depicted in Figures 5.12(a)-(c), the tunneling conductance maps for $H = 0$, -0.3 T and 3.0 T over the same (28×250) nm^2 sample area at $\omega = \Delta_+$ exhibit field-dependent spatial evolution similar to that found in Figures 5.14(a)-(c). Again, the histograms of Δ_+ show the same monotomic field dependence as observed in the tunnel conductance, and in contrast to the findings with a Cr-coated tip. In summation, the differences between aforementioned field-dependent spectra taken at 6 K with Cr-coated tips and those taken with Pt/Ir tips, as shown in Figures 5.7- 5.12, are all consistent with and serve to establish spin-polarization tunneling in the former case. To further investigate spin-polarized tunneling in the manganite, we consider in the following subsection numerical simulations of the tunneling spectra under different

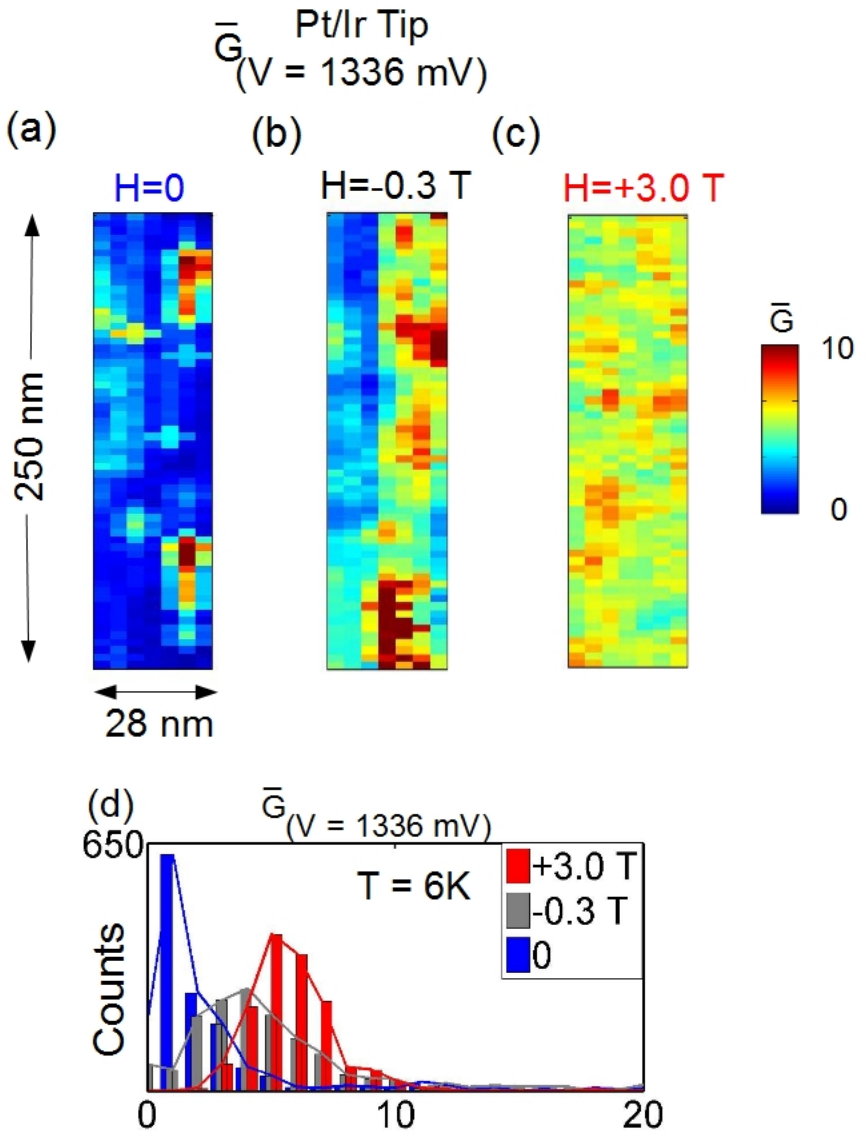

Figure 5.11: Comparison of magnetic field-dependent high-bias tunneling conductance maps taken at $\omega = \langle U_+ \rangle \sim 1336$ meV over a (28×250) sample area with a Pt/Ir tip at $T = 6$ K and for (a) $H = 0$, (b) $H = -0.3$ T, and (c) $H = 3.0$ T. (d) Histograms of the normalized tunneling conductance $\bar{G}$ at $\omega = \langle U_+ \rangle$ at $H = 0$, -0.3 T and 3.0 T.

conditions.

5.3.4 Simulations of the Tunneling Spectra

To aid in understanding the evolution of tunneling spectra with magnetic fields and spin polarization, we must consider the theoretically calculated DOS of both LCMO and Cr. Specifically, the tunneling current (I) from Cr to LCMO as a function of the bias voltage (V) may be expressed by the following:

$$\begin{aligned} I(V) &= G\sum_{\sigma,\sigma'=\alpha,\beta}\int dE N^{\sigma}_{\mathrm{Cr}}(E-eV)N^{\sigma'}_{\mathrm{LCMO}}(E) \\ &\quad \times T(E,H,\theta)[f_{\sigma}(E-eV)-f_{\sigma'}(E)], \end{aligned} \tag{5.1}$$

where E denotes the energy relative to the Fermi level, G is the conductance, σ and σ' refer to the spin-dependent energy bands (majority band: α, minority band: β) of Cr and LCMO, respectively, $f_{\sigma}(E) = 1/[\exp(E/k_BT)+1]$ is the Fermi-Dirac distribution function for σ-band, $\mathrm{N}^{\sigma}_{\mathrm{Cr}}(E)$ and $\mathrm{N}^{\sigma'}_{\mathrm{LCMO}}(E)$ are the spin-dependent density of states of Cr and LCMO, respectively, and $\mathrm{T}(E,H,\theta)$ represents the tunneling matrix of the STM junction that depends on the relative magnetization angle (θ) between the Cr and LCMO. Thus, the normalized conductance $(dI/dV)(V/I)$ can be determined from Equation 5.1 for given $\mathrm{N}^{\sigma}_{\mathrm{Cr}}(E)$ and $\mathrm{N}^{\sigma'}_{\mathrm{LCMO}}(E)$, provided that the relative spin configurations of Cr and LCMO are known and that the tunneling matrix is nearly independent of energy.

For thin film Cr coated tips, it is reasonable that the geometry of the tip will determine magnetization axis of the magnetic layer for all temperatures of the experiments and is thus fixed and can be approximated as perpendicular to the plane of the LCMO sample. Therefore, at $H = 0$ the angle θ will follow the spatial variation of the magnetization direction of the LCMO sample from one magnetic domain to another. On the other hand, application of a magnetic field opposing the spin polarization of the Cr tip with the magnitude in the range of $H_c^{\mathrm{LCMO}} < |H| < H_c^{\mathrm{Cr}}$ will force the alignment of the LCMO magnetic domain antiparallel to the Cr tip. As the selection rules for spins result in a tunnel matrix $\mathrm{T}(E,H,\theta=0)=0$, the spin-polarized tunneling current involves

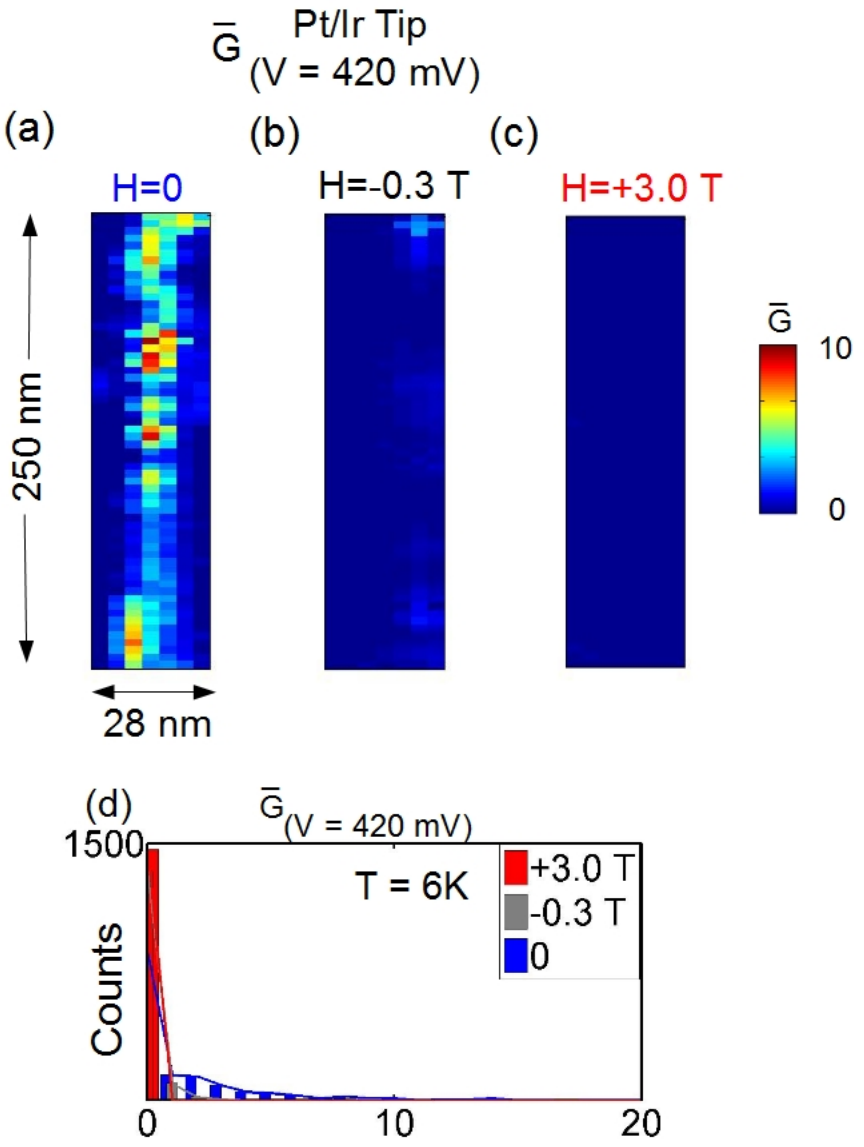

Figure 5.12: Comparison of magnetic field-dependent low-bias tunneling conductance maps taken at $\omega = \langle \Delta_+ \rangle \sim 420$ meV over the same sample area as in Figure 5.11 with a Pt/Ir tip at $T = 6$ K and for (a) $H = 0$, (b) for $H = -0.3$ T and (c) $H = 3.0$ T. (d) Histograms of the normalized conductance $\bar{G}$ at $\omega = \langle \Delta_+ \rangle$ and for $H = 0$, -0.3 T, and 3.0 T.

only tunneling of electrons from occupied Cr-majority band to empty LCMO-minority band and tunneling of holes from empty Cr-minority band to occupied LCMO-majority band. Hence, for anti-parallel Cr and LCMO magnetizations, the normalized tunneling conductance $g_{\uparrow\downarrow}(V)$ may be approximated by the following joint density of states:

$$g_{\uparrow\downarrow}(V) \sim N^{\alpha}_{\mathrm{Cr}}(0)N^{\beta}_{\mathrm{LCMO}}(eV) + N^{\beta}_{\mathrm{Cr}}(0)N^{\alpha}_{\mathrm{LCMO}}(eV). \tag{5.2}$$

A similar logic applied to the parallel magnetic orientation between Cr tip and LCMO sample magnet domains results in the normalized tunneling conductance involving tunneling of electrons from occupied Cr-majority band to the empty LCMO-majority band and holes from empty Cr-minority band to occupied LCMO-minority band. Therefore, $\mathrm{T}(E, H, \theta = \pm\pi\beta) = 0$, and the normalized tunneling conductance $g_{\uparrow\uparrow}(V)$ becomes

$$g_{\uparrow\uparrow}(V) \sim N^{\alpha}_{\mathrm{Cr}}(0)N^{\alpha}_{\mathrm{LCMO}}(eV) + N^{\beta}_{\mathrm{Cr}}(0)N^{\beta}_{\mathrm{LCMO}}(eV). \tag{5.3}$$

Given Eqs. 5.2 and 5.3 and the band structure calculations for $\mathrm{N}^{\alpha,\beta}_{Cr}(E)$ and$\mathrm{N}^{\alpha,\beta}_{LCMO}(E)$ illustrated in Figure 5.13, calculation of the energy-dependent spin-polarized tunneling conductance is possible. For various configurations under both non-polarized and spin-polarized tunneling, as schematically demonstrated in Figures 5.14(a)-(d), the resulting tunneling spectra are calculated and shown in the bottom row of Figure 5.14. The tunneling conductance at $\omega = U_+$ is maximum for the anti-parallel spin configuration between the Cr-coated tip and LCMO due to a large overlap between Cr filled spin majority electrons tunneling into LCMO empty spin minority states, and consistent with the empirical histograms of the tunneling conductance shown in Figure 5.8(b). Hence, the field-dependent tunneling spectra of LCMO obtained with a Cr-coated tip in the high-bias limit may be fully accounted for by spin-polarized tunneling in a spin-valve configuration.

In particular, the spin-valve configuration between the Cr-coated tip and the LCMO sample allows calculation of the the spin-polarization of the Cr-coated tip at $\omega = \langle U_+ \rangle$. In a typical spin-valve, the difference in the device resistance between the parallel and antiparallel magnetic

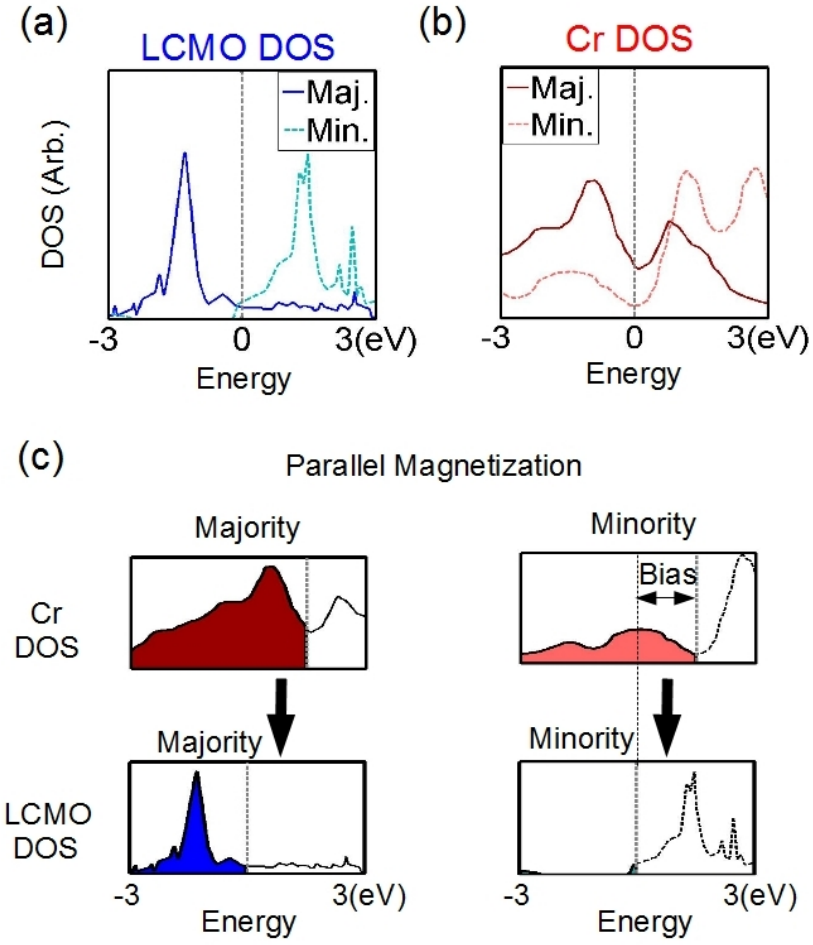

Figure 5.13: Calculated density of states (DOS) for LCMO and Cr at $T \ll T_c$ from band structure calculations: (a) Theoretical DOS for the majority and minority bands of LCMO with $x = 0.25$ [5]. (b) Theoretical DOS for the majority and minority bands of the first layer of Cr in a thin film [42]. (c) Theoretical tunneling configurations for parallel magnetization between Cr-coated tip and LCMO sample under a finite bias voltage $V = (U_+/e)$, showing tunneling of electrons from the majority band of Cr to the empty majority band of LCMO as well as tunneling of holes from the empty minority band of Cr to to the filled minority band of LCMO.

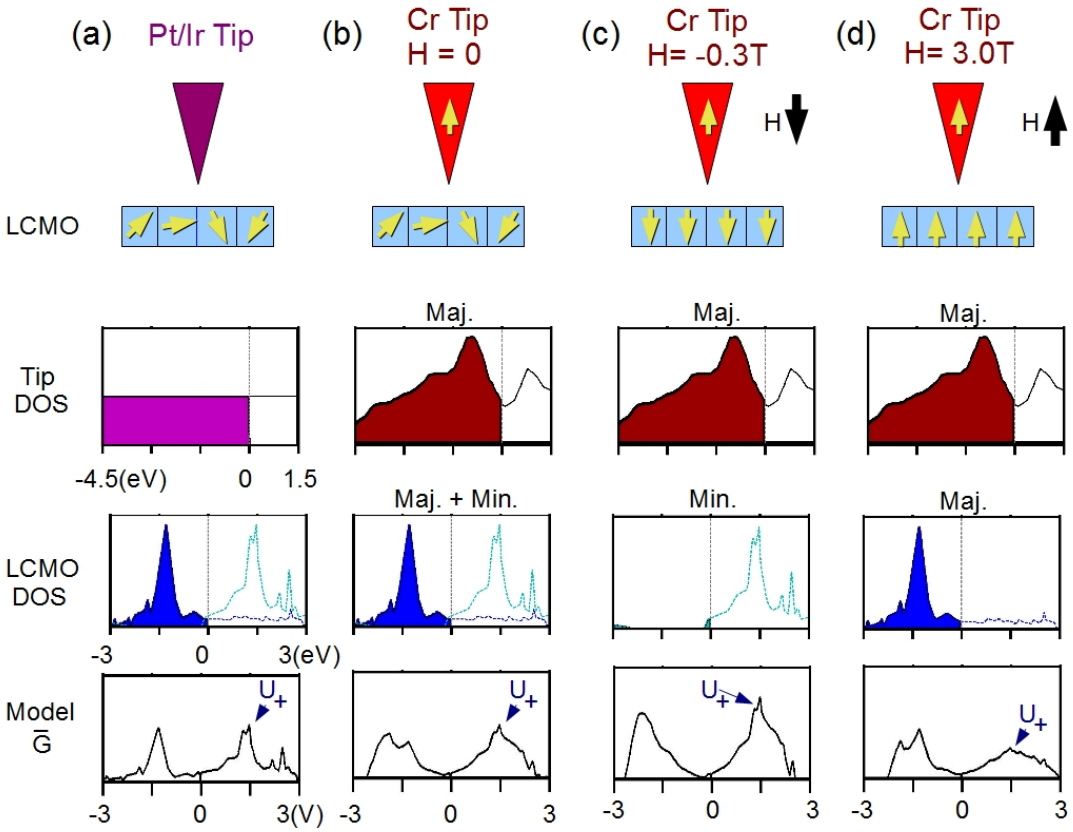

Figure 5.14: Modeling of magnetic field and spin-polarized tunneling effects on the resulting tunneling spectra at $T \ll T_C^{\mathrm{LCMO}}$: Schematic illustrations of STS measurements with (a) a Pt/Ir tip at $H = 0$, showing non-polarized tunneling currents into ferromagnetic LCMO with randomly oriented magnetic domains; (b) a Cr-coated tip at $H = 0$, showing spin-polarized tunneling currents into ferromagnetic LCMO with randomly oriented magnetic domains; (c) a Cr-coated tip at $H = -0.3$ T, showing spin-polarized tunneling currents into ferromagnetic LCMO with magnetic domains antiparallel to the spin polarization of the tunneling currents; (d) a Cr-coated tip at $H = 3.0$ T, showing spin-polarized tunneling currents into ferromagnetic LCMO with magnetic domains parallel to the spin polarization of the tunneling currents. The energy dependent DOS of the Cr-coated tip and that of the LCMO sample relevant to each spin configuration are shown in the second and third rows, respectively. Finally, the calculated tunneling conductance for each configuration is shown in the bottom row, which clearly illustrates maximum tunneling conductance $\bar{G}$ at $\omega = U_+$ for the anti-parallel spin configuration at $H = -0.3$ T.

configuration for the two ferromagnetic layers can be expressed as the conductance ratio R_G, where

$$R_G = \frac{G_{\uparrow\uparrow}(V) - G_{\uparrow\downarrow}(V)}{G_{\uparrow\downarrow}(V)}, \tag{5.4}$$

where $G_{\uparrow\uparrow}(V)$ and $G_{\uparrow\downarrow}(V)$ are the conductance of the device in parallel and antiparallel magnetic configuration at bias voltage V, respectively. The conductance ratio of the device can also be related to the spin-polarization of each individual ferromagnetic layer by [45]

$$R_{MR} = 2 \times \frac{P_1 P_2}{1 - P_1 P_2}, \tag{5.5}$$

with P_1 and P_2 the spin-polarization of each respective ferromagnetic layer. We can generalize from the case of the planar spin valve to the case of spatially resolved SP-STM conductance maps at $\omega = V$ by integrating the quantities in the numerator and denominator in section 5.4 over the entire scan area. As demonstrated in Figure 5.14, we can assign the normalized conductance values of the H = -0.3 T map to the case of antiparallel magnetic orientation between tip and sample, while associating the conductance values of the H = 3.0 T map to a parallel magnetic orientation. Substitution into Section 5.5 results in

$$\frac{\int\int (g_{(H=3.0T)}(\langle U_+ \rangle) - g_{(H=-0.3T)}(\langle U_+ \rangle))dxdy}{\int\int g_{(H=-0.3T)}(\langle U_+ \rangle)dxdy} = 2 \times \frac{P_T P_S}{1 - P_T P_S}, \tag{5.6}$$

where P_T is the spin polarization of the Cr tip, an P_S is the polarization of the LCMO sample. Polarization of the LCMO film can be estimated from band structure calculations for LCMO with x=0.25 [5] to be 61% and 93% at $\omega = \langle U_+ \rangle$ and $\omega = \langle U_- \rangle$ respectively. This leads to calculated polarization values for the Cr tip of 23% and 8% for $\omega = \langle U_+ \rangle$ and $\omega = \langle U_- \rangle$ respectively.

5.4 Discussion

The simulations described in Section 5.3.4 are based on the assumption of non-polarized and spin-polarized tunneling in bulk LCMO samples, depending on the choice of STM tip. The simulated

results are consistent with the experimental high-bias spectral behavior, showing tunneling currents from the Cr-coated tip may be considered as spin-polarized along a fixed direction for all temperatures and magnetic fields of our consideration. Next, we can consider the behavior of the low-bias gap observerd under both regular and spin-polarized tunneling at 6 K, which provides useful information concerning the nature of surface phase of LCMO. In the case of regular tunneling using Pt/Ir-tips, the histograms of the field-dependent insulating gap Δ_+ shown in Figure 5.10(e) reveal that increasing magnetic field strength leads to increasingly sharper distributions of gap values, in addition to the independence of most probable value of Δ_+ on the magnetic field direction. In contrast, histogram of gap values shown in Figure 5.7 for the Cr-coated tips shows that spin-polarized tunneling exhibits decidedly different field-dependence of the insulating gap Δ_+ as compared to Figure 5.10(e). Essentially, the zero-field Δ_+ values measured with the Cr-coated tip appear to exhibit a bimodal distribution, showing a sharper distribution peaking at the pseudogap energy Δ_+^* and a broader distribution centering around a gap value comparable to Δ_+^{P}. On application of the $H = -0.3$ T field, the distribution of Δ_+ evolves to become narrowly centering around a higher energy gap $\Delta_+^{\mathrm{AP}} > \Delta_+^{\mathrm{P}}$, and with the psuedogap features strongly suppressed. In contrast, for $H = 3.0$ T, the distribution of Δ_+ is largely concentrated around Δ_+^{P} with a linewidth broader than that for $H = -0.3$ T, with the same suppression of the pseudogap features.

The low-temperature field-dependent Δ_+ distributions shown in Figures 5.7(e) and 5.10(e) may be understood in context of a ferromagnetic insulating surface phase. Consultation of the $La_{1-x}Ca_xMnO_3$ phase diagram [12] shows at low temperatures the manganites are in a ferromagnetic insulating phase if the Ca doping level x is less than 0.2. Additionally, Ca deficiency at the surface with respect to the nominal bulk level x for the manganites has been confirmed by x-ray photoemssion spectroscopy (XPS) [63]. This leads to the possibility that the $x = 0.3$ thin films experience an underdoped surface, possibly sufficient to generate a ferromagnetic insulating surface layer. Second, the magnetization direction of the ferromagnetic insulating phase should follow that of the underlying ferromagnetic bulk domain, with a randomly oriented direction in the absence of applied magnetic field. Therefore, for spin-polarized tunneling currents from the Cr-coated tip, the effective insulating

gap values would range from the minimum gap Δ_+^{P} to the maximum gap Δ_+^{AP}, as schematically illustrated in Figure 5.15(b). Aditionally, a pseudogap at a lower energy Δ_+^* is also present for $H = 0$ due to the electronic inhomogeneity of the manganites. Similar observation of a range of insulating gap value and the psuedogap value is also expected for non-polarized tunneling at $H = 0$ although the lack of spin selectivity broadens the gap distribution. Both expected zero-field gap distributions are consistent with the empirical gap histograms shown in Figure 5.15(e). Considering the application of magnetic field, if the surface ferromagnetic insulating phase has a similar coercive field to that of the bulk ferromagnetic metal phase, the ferromagnetic insulating domains would be aligned in the same configuration as the bulk, as depicted in Figure 5.14(c) for $H = -0.3$ T. Hence, a tunneling current polarized antiparallel to the LCMO surface magnetization would result in a maximum insulating gap Δ_+^{AP} with a relatively sharp gap distribution, as indicated in Figure 5.15(c) and experimentally confirmed by the gap histogram in Figure 5.15(e). Finally, for spin-polarization of the tunneling currents being parallel to the magnetization of LCMO, as in the case of $H = 3.0$ T shown in Figure 5.14(d), the insulating gap decreases to Δ_+^{P} (see Figure 5.14(d)), which is the same as that found for non-polarized tunneling currents and is smaller than the gap Δ_+^{AP}. The larger observed energy gap for anti-parallel spin-polarized tunneling than that for parallel spin-polarized tunneling provides an effective spin-filtering effect, which has been confirmed by the empirical gap histogram shown in Figure 5.15(e).

Additionally we observe a strong suppression of the psuedogap with applied magnetic field. The presence of the pseudogap phenomenon with spin-polarized tunneling at $H = 0$ appears to be strongly suppressed rapidly with increasing field, as indicated in Figure 5.15(e). While the pseudogap energy Δ_+^* found at $H = 0$ is largely temperature independence as shown in Figures 5.7(f) and 5.10(f), the rapid suppression of pseudogap phenomena under finite magnetic fields is consistent with theoretical predictions that the pseudogap phenomenon in the manganites originates from the inherent electronic heterogeneity of the manganites [61, 62]. Consequently, increasing carrier mobility and magnetic domain alignments upon the application of magnetic fields reduces the spatially inhomogeneous electronic properties in the manganites, rapidly suppressing the pseudogap

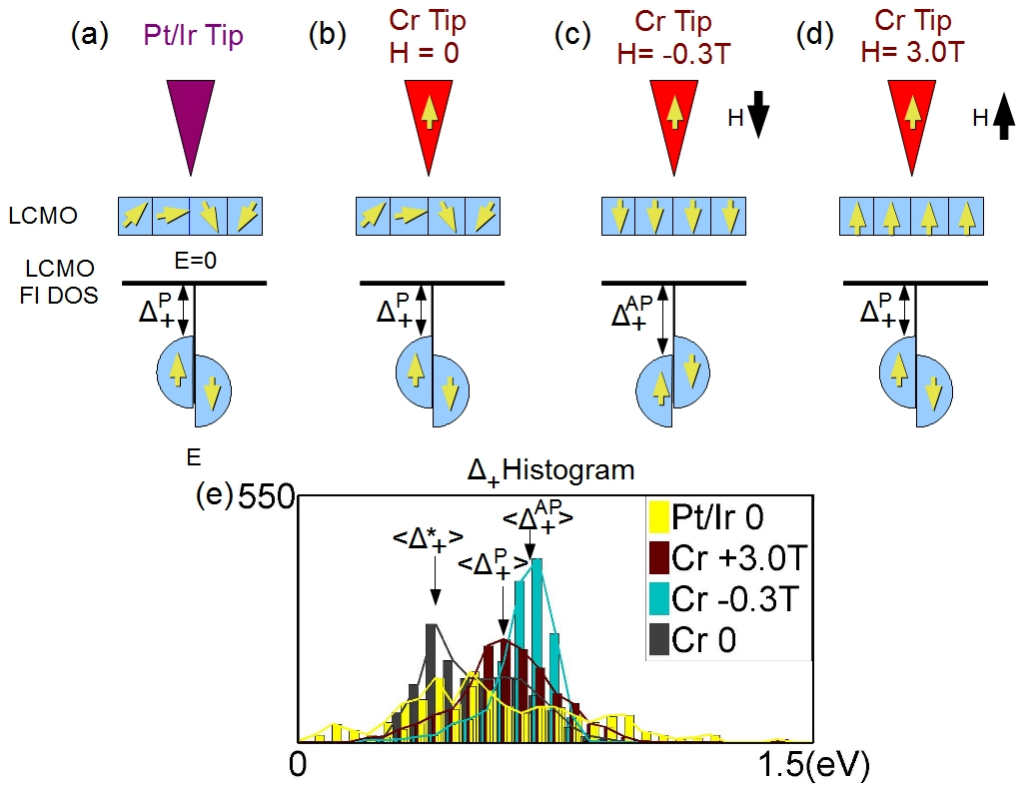

Figure 5.15: Effect of magnetic field and spin-polarized tunneling on the surface ferromagnetic insulating phase at low temperatures: Schematic energy (E) vs. density of states (DOS) plots of the surface ferromagnetic insulating phase in LCMO thin films, showing an energy gap $\Delta_+^{\rm P}$ relative to the Fermi level for the majority band and a larger energy gap $\Delta_+^{\rm AP}$ for the minority band. (a) For Pt/Ir tip at $H = 0$, the tunneling gap is detemined by the minimum gap $\Delta_+^{\rm P}$ in addition to the presence of a pseudogap at Δ_+^* due to the electronic heterogeneity in the manganites; (b) For Cr-coated tip at $H = 0$, the tunneling gap Δ satisfies $\Delta_+^{\rm P} \leq \Delta_+ \leq \Delta_+^{\rm AP}$ in addition to a pseudogap at Δ_+^*; (c) For Cr-coated tip at $H = -0.3$ T, the tunneling gap Δ_+ is largely determined by the maximum gap $\Delta_+^{\rm AP}$, with the pseudogap mostly suppressed due to the suppresion of electronic heterogeneity in the presence of finite fields; (d) For Cr-coated tip at $H = 3.0$ T, the tunneling gap Δ_+ is largely determined by the minimum gap $\Delta_+^{\rm P}$, and the pseudogap is also largely absent as in (c). The scenario described from (a) to (d) is consistent with the corresponding spin polarization- and field-dependent histograms of the gap shown in (e).

phenomenon with increasing magnetic fields.

In addition to aforementioned progress in understanding the physical origin of the surface insulating phase, apparent phase separations in the nominally metallic LCMO with $x = 0.3$ have been observed in the spatially resolved tunneling spectroscopic studies conducted here. Specifically, the separations appear to be on the scale of $\sim 10^2$ nm, and the phases seem to be associated with variations above and below the nominal Ca doping level x due to the distribution of different values of U_+ that are correlated with different Ca doping levels. This quasi-macroscopic phase separation revealed in this work differs from the droplet- or stripe-like inhomogeneous states that are primarily stabilized by long-range Coulomb interactions, suggesting that significant Coulomb screening is still present in the bulk of this nominally metallic LCMO.

5.5 Conclusion

In conclusion, non-polarized and spin-polarized spatially resolved tunneling spectra on the CMR manganite $La_{0.7}Ca_{0.3}MnO_3$ (LCMO) has been studied systematically as a function of the temperature and applied magnetic fields. Spatial variations in the tunneling conductance show apparent phase separations, and the spectral characteristics obtained under the spin-valve configurations can be quantitatively accounted for by the spin-dependent joint density of states of the LCMO and the Cr-coated STM tip, consistent with the injection of a spin-polarized tunneling current. The low-energy insulating gap at low temperatures detected only by STM studies can be explained by a surface ferromagnetic insulating phase due to Ca deficiency at the manganite surface, as this behavior is consistent with the spin filtering behavior of the phase discovered with spin polarized tunneling current. In addition, a spatially varying pseudogap (PG) phenomena with a nearly temperature independent PG value have been observed above and below the Curie temperature in zero-field tunneling spectra. Under an applied magnetic field, the PG phenomena is strongly suppressed, in conjunction with a significant increase in homogeneity of the tunneling spectra of LCMO. These results suggest the notion that the PG phenomena is related to the electronic inhomogentiy of the manganites. Finally, the quasi-macroscopic phase separations observed in the $La_{0.7}Ca_{0.3}MnO_3$ epitaxial films are

indicative of significant screening of long-range Coulomb interactions, which is consistent with the bulk metallic characteristics of the system and differs from other competing order systems near the metal-insulator transition.

Chapter 6

Organic Semiconductors

6.1 Introduction

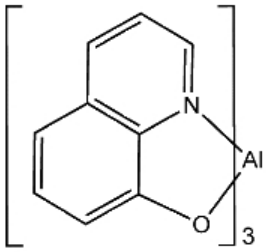

Figure 6.1: Molecular structure of Alq_3.

This work focuses on the molecular organic semiconductor 8-hydroxyquinoline aluminum, or Alq_3. The chemical formula is $C_{27}H_{18}AlN_3O_3$, with the fundamental structure of Alq_3 consisting of a central aluminum atom surrounded by three non-coplanar quinoline ligands of the chemical formula C_9H_6NO, as depicted in Figure 6.1. Alq_3 occurs in two inequivalent isomers: a facial isomer where each ligand is equivalent, and a meridional isomer were each ligand is inequivalent and must be considered separately [76]). The meridinal isomer is slightly lower in energy ($\sim$4 kcal/mol) and predominates in thin films and crystals of the material [76] but it is possible the facial isomer is stabilized at the film/substrate interface (Chapter 7). The relevance of the facial isomer for application is due to a reduction in the bandgap to 2.4 from 2.7 eV for the meridinal isomer, and the resultant change in conduction and luminescent properties [77].

Due to the complex three-dimensional asymmetric structure of the molecule, a multitude of

packing arrangement of Alq_3 are possible in crystal structures. In thin films, the temperature during deposition, chemistry, and atomic structure of substrate and predeposition processing of the Alq_3 powder for deposition will modify the packing of Alq_3 molecules in the resulting film, resulting in one of several crystalline structures or in an amorphous collection of molecules. Muccini et al. identified three separate phases of Alq_3, each with a separate photoluminescient spectrum [78], while Jian et al. noted changes in film morphology and temperature dependence of the conductivity with varied substrate temperature during deposition [79]. Modification of the optical properties of Alq_3 thin films makes them configurable for a variety of luminescient applications, while the dependence of film conductivity on substrate temperature has important implications on efficient device fabrication.

6.2 Principles of Electron Conduction in OSEs

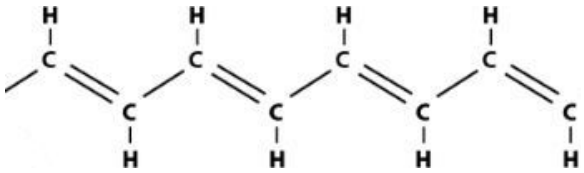

Figure 6.2: Chemical structure of trans-polyacetylene, the simplest of polymer organic semiconductors, illustrating the delocalized pi-bound electron critical to semiconducting behavior.

An appropriate question regarding organic semiconductors is why they are possible, since everyday experience with dessicated organic material has shown them to be insulators (i.e., wood, plastics). Polymers were the first organic semiconductors studied, and although Alq_3 is a molecular rather than polymeric organic semiconductor, the principles of electron or hole conduction along the hydrocarbon chains of the molecule and hopping between crystals in a film is similar across the entire organic semiconductor family. Polymeric organic semiconductors consist of a matrix of hydrocarbon chains of indeterminate length [80], with conduction electrons in delocalized π bonds. In saturated polymers, all electrons pertaining to the carbon atoms are covalently σ bonded and localized. Metallic or semiconducting states are only possible in conjugated polymers such as polyacetylene, where a single π bound electron per carbon atom is delocalized along the chain. A single electron combined with the two available states on each carbon atom would normally lead to a metallic state, but the

alteration of the carbon bond lengths (dimerization) of the polymer due to the Peierls instability leads to a bandgap [80]. In contrast with conventional inorganic semiconductors such as Silicon and Germanium, conduction in polymers is quasi one-dimensional, leading to a strong presence of excitons and polarons [81]. The presence of the excitons is significant due to their role in electroluminescience in the material (Chapter 6.3), while polarons give rise to polaronic levels within the bandgap, changing the effective threshold for hole or electron injection in the semiconductor.

To fully describe electrical transport in an Alq_3 thin film, we must additionally model conduction not just within Alq_3 molecules but between neighboring molecules as well. Both muon spin relaxation [28] and variable temperature conductivity measurements [29] have shown that mobility in Alq_3 can be described in terms of hopping transport, where the quantum tunneling between molecules is dependent on temperature, electrical field, and interatomic spacing. In particular, the activated hopping description used by Hirsch [82] shows inverse exponential dependence of the mobility μ on the separation between hopping site R, suggesting a strong dependence of conductance in the film on the molecular separation in the particular crystal structure.

Three factors in total then contribute to conduction across thin films of Alq_3: intermolecular, or transfer of electrons or holes between differing sections of an Alq_3 molecule; intergrain, or between different Alq_3 molecules in the same crystal structure; and intragrain, or between different crystalline grains. Conduction in Alq_3 is dominated by either the inter- or intragrain factors, as muon spin relaxation measurements on Alq_3 thin films has identified a 5 orders of magnitude difference in the intermolecular vs intramolecular mobility (2.3 x 10^{-1} $cm^2(Vs)^{-1}$ vs 1.2 x 10^{-5} $cm^2(Vs)^{-1}$) [28]. However, the lower bound for intergrain mobility from muon spin resonance still exceeds the value of 1.4 x 10^{-6} $cm^2V^{-1}s^{-1}$measured using time of flight measurements, where the time required for a photo generated current to travel the width of a Alq_3 layer between two metal electrodes under bias is used to estimate the mobility. The inferior mobility of Alq_3 film measured using bulk techniques highlights the importance of crystal grains in performance of devices, and the need to eliminate them for superior device performance.

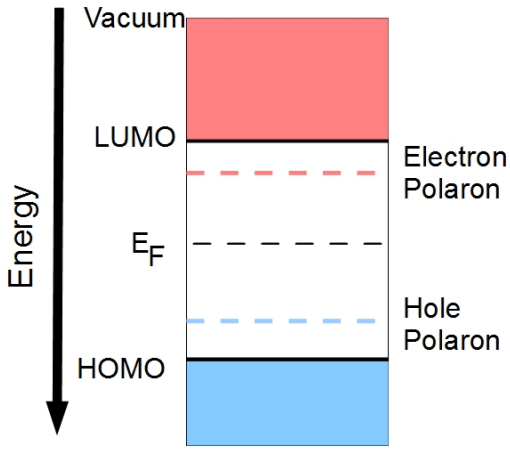

Figure 6.3: Energy level diagram common to all organic semiconductors, with the fermi energy E_F and HOMO and LUMO which are equivalent to the conventional semiconductor's conduction and valence band, respectively. Within the energy gap are electron or hole polaron states.

6.3 Semiconducting Characteristics

In organic semiconductors, the analogs the conduction and valence band bands are the highest occupied molecular orbital (HOMO) and the lowest unoccupied molecular orbital (LUMO), respectively (Figure 6.3). In organic semiconductors, the addition of electrons or holes often leads to an accompanying deformation of the surrounding bond lengths, giving rise to excitations termed polarons [81]. This mechanism leads to electron and hole polaron levels within the energy gap (Figure 6.3), possibly modifying the voltage onset for conduction, with the precise energy of the polaronic levels depending on the specific material. For the Alq_3, the LUMO and HOMO are located 2.9 and 5.7 eV from the vacuum energy level respectively [22], with polaronic states located approximately 0.2 eV into the semiconducting gap [31]. Density functional theory calculations have shown that the ring of the ligand closest to the oxygen atom, or the phenoxide portion, is the location of the HOMO orbitals, while the ring closest to the nitrogen contains the LUMO orbitals [77]. The Al center atom does not participate in the conduction. Localization of LUMO and HOMO in Alq_3 (Figure 6.4) accentuates dependence of film conductance on the crystal structure.

Organic semiconductors often exhibit electroluminescience in tandem with their semiconducting

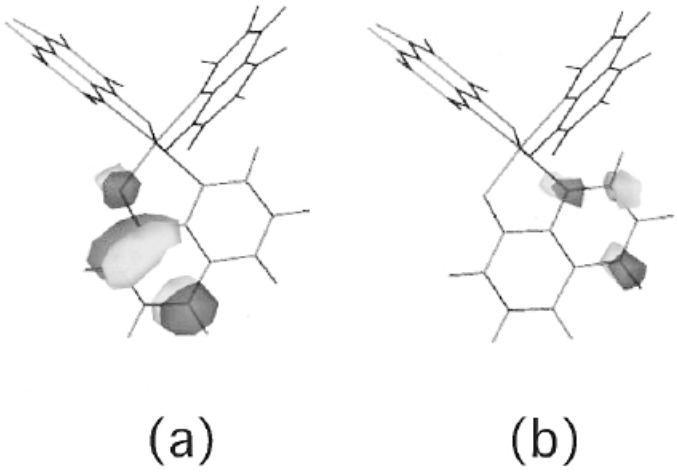

Figure 6.4: Structure of Alq_3 molecule displaying the three ligands. In (a), for a representative ligand, the location of the HOMO (filled) states are highlighted with cloud illustrations. (b) similarily indicates the location of the LUMO (unfilled) states. This localization of filled and unfilled states holds for all three ligands. Figure adapted with permission from Burrows et al. [30]

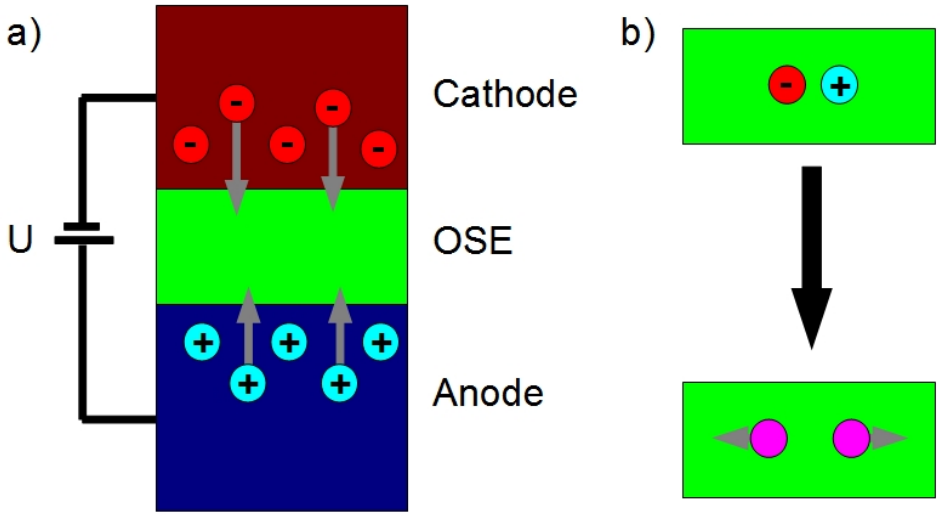

Figure 6.5: (a) A metal/organic semiconductor/metal heterostructure under a bias U will cause injections of electrons (red) and holes (blue) into the organic semiconductor from the cathode and anode respectively. (b) An electron-hole pair can form a singlet exciton state and then can decay radiatively into photons (purple).

gap. The generation of light in the organic semiconductor is accomplished by the injection of a hole and electron, the formation of an exciton, which is a bound state of a hole and electron, and then the decay of the exciton to emit photons(Figure 6.5). Assuming the electron-hole capture process to be spin indepedent, spin triplet states are formed in a 3:1 ratio vs spin singlet. As only the spin

singlet states are allowed by conservation of angular momentum to radiatively emit light, a simple estimate of device efficiency should give a maximum value of 25%. One major contribution of spin polarized LEDs is the ability to control the spin of injected electrons and holes to favor spin singlet exciton formation. The 2.8 eV bandgap leads to predicted emission of light at 459 nm wavelength, but the precise spectrum depends substantially on the Alq_3 crystalline phase [83].

6.3.1 STM on Organic Semiconductors

Alvarado et al. were the first to apply the STM technique to organic materials, studying PPV and its derivatives in 2-12 nm thick films [84]. The pioneering work focused on using the vertical tip displacement vs bias voltage measurements to determine the alignment of HOMO and LUMO of the semiconductor to the energy level of the Au(111) substrate, and combining STM measurements with optical absorption to determine the exciton binding energy in the semiconductor. By intially establishing the tunnel junction at high magnitude bias and scanning over a small area, and then reducing the bias voltage magnitude while monitoring the mean z-position of the STM tip, the voltage for onset of conduction was identified for positive and negative voltages [84]. The sum of the positive and negative voltage onsets, or single particle energy, was compared with the peak in optical absorbtion to identify the exciton binding energy. Notable is the absence of clearly resolved topographic scans, with atomic resolution or otherwise, and spectroscopic measurements; in practice, these measurements are only possible on monolayer or bilayer thickness films, such as pentacene and perfluoropentacene on Bi(0001) [85].

Alvarado's work highlights the unconventional techniques required for investigation of multi-atomic layer OSE films with STM. For Alq_3 thin films, the semiconducting bandgap necessitates a high bias voltage to enable injection of electrons or holes into the LUMO and HOMO, while the relatively low electron mobility range requires a low bias current. For these reasons, it was found necessary to use bias voltages of 3V (on the order of the bandgap), and to limit tunneling current to 20 pA to prevent charging effects and give reproducible topographic scans. Even under these conditions, the ability to resolve clusters of atoms changes over time as Alq_3 appears to easily

interact with the STM tip. Development of a technique similar to Alvarado's experiment, consisting of monitoring tip height vs bias voltage (Chapter 2.1.1), was used to elucidate the band structure of Alq_3 films on LCMO (Chapter 7).

Chapter 7

Electron Transport Properties and the Effect of Annealing in Alq_3/LCMO Heterostructures

We have successfully deposited and investigated Alq_3/LCMO heterostructures of varying thicknesses to investigate charge transport in Alq_3. Bulk Alq_3 structural properties are preserved down to 10 nm in thickness with a -0.3 eV offset in band energies. The lack of band bending between LCMO and Alq_3 is suggestive of a shift in the preferred isomer from meridinial to facial at the interface. The absence of polaron states from our STM studies implies the relative unimportance of polarons in Alq_3 for this heterostructure. In addition, the measured mobilities on the order of 10^{-5} $cm^2(Vs)^{-1}$ for electrons and holes more closely resemble values of the intrinsic mobility estimated from the muon spin relaxation measurements than those from studies of the bulk LED structures, suggesting that superior film conductivity close to the fundamental limit is possible with a heated substrate during sublimation.

7.1 Motivation

Organic semiconductors (OSE) have potential in the development of spintronic devices as the semiconducting spacer layer in the spin valve structures or as the electroluminescient layer in spin-polarized LEDs. 8-hydroxyquinoline aluminum, or Alq_3, in particular has been the focus of much experimental effort due to its high intrinsic mobility [28], tunable luminsescient spectrum as a func-

tion of crystal structure [78], and low cost and easy deposition techniques of low temperature sublimation and spin casting. Electronic transport in Alq_3 thin films has been previously investigated in bulk metal/Alq_3/metal structures, and more complicated structures, with spin-neutral [86] and-spin polarized [22] currents. Xiong et al. [22] reported a spin diffusion length in Alq_3 of 45 nm, reinforcing the promising potential for the use of Alq_3 in spintronics devices. However, the presence of an ∼100 nm thick Alq_3 layer implied that the conductive properites of the spintronic device were dominated by metallic inclusions and pinholes from the top electrode to the bottom metal. These fabrication difficulties, combined with the inherent band bending from metal/semiconductor interfaces, complicate clear investigation of the transport properties of the OSE spacer layer. In order to eliminate the pinholes and charge migration associated with the top metallic electrode in direct contact with the OSE spacer, we have chosen to replace the electrode with a scanning tunneling microscope (STM) tip separated from the OSE by a vacuum gap. In this work, we use STM to investigate the charge transport by measuring electron and hole mobility and energy level alignment of Alq_3 deposited on $La_{0.7}Ca_{0.3}MnO_3$ (LCMO), a half-metallic ferromagnet below its Curie temperatur [5] chosen for subsequent spin transport measurements.

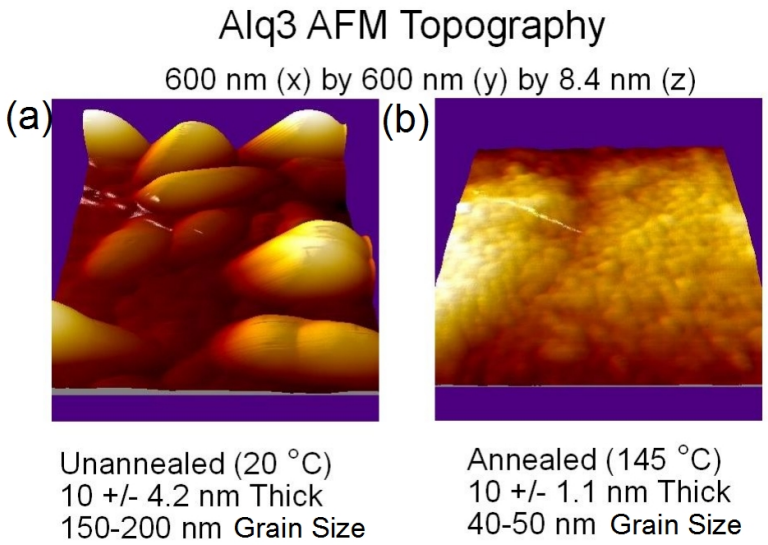

Figure 7.1: 3D presentation of AFM images of Alq_3 films deposited on LCMO films. The images are on a (600 nm x 600 nm x 8.4 nm) scale. Alq_3 films of the same thickness deposited on unannealed (left) and annealed (right) LCMO films illustrate the fourfold reduction in roughness with heating of the substrate.

7.2 Experimental Details

We have studied Alq_3 films of 20, 10, and 5 nm thicknesses deposited on 100 nm (LCMO) films. Growth details and characterization measurments for the LCMO samples were discussed in Chapter 3. Alq_3 films are deposited by thin film sublimation under a vacuum of approximately 10^{-6} mbar pressure at a rate of 1.2 nm/min (confirmed with ex situ atomic force microscope (AFM) measurements on $SrTiO_3$ substrates), with the LCMO film heated to 145°C during the deposition. Investigations of film morphology vs substrate temperature during deposition revealed Alq_3 films grown on substrates heated to 145°C showed fourfold decrease in roughness (Figure 7.1), in addition to changes in mobility to be discussed in Section 7.3. Following cooling and removal of the heterostructure from the chamber, the samples were installed in a custom built high vacuum STM system (Appendix A) loaded with a Pt/Ir STM tip, and all subsequent measurements are conducted at high vacuum (10^{-6} mbar) in a chamber protected from ambient light to preserve the sample quality.

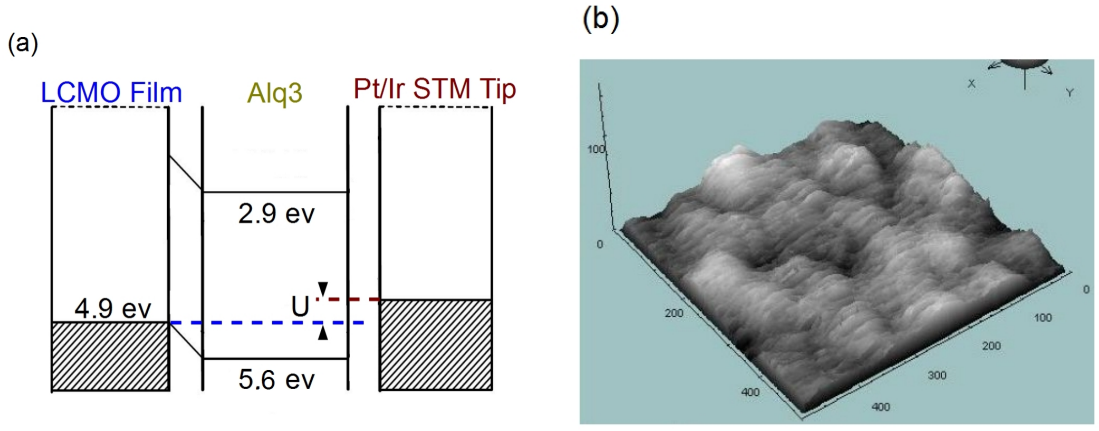

Figure 7.2: (a) Band structure of Pt/Ir Tip and LCMO/Alq_3 heterostructure, with a bias voltage U applied to the sample. Band bending exists between LCMO and Alq_3 and is absent between the semiconductor and STM tip due to the vacuum gap. (b) Representative topography of Alq_3 film taken with +3V bias voltage and 20 pA bias current. The bulk thickness of this Alq_3 film was estimated at 2 nm. The scale is 500 $\AA$ by 500 $\AA$, with a height scale of 100 $\AA$.

The energy level diagram of Alq_3 and the resulting heterostructure, including the STM tip, at negative sample bias is shown in Figure 7.2(a). The work function of LCMO is 4.8 eV [57], while those of the lowest unoccupied molecular orbital (LUMO) and highest occupied molecular orbital

(HOMO) of $Alq_3 at 2.9 eV and at 5.7 eV$ [22], *respectively. The STM image of a 2 nm thick* Alq_3 film is shown in Figure 7.2 (b), which demonstrates successful establishment of a tunnel junction between the STM tip and the heterostructure. The 3V bias voltage and 20 pA bias current is critical for reproducible imaging and tip height measurements due to the non-negligible resistance of the Alq_3 film (Section 7.3).

If the xy scanning of the STM tip is disengaged, and the bias voltage between tip and heterostructure is reduced in magnitude while the tunneling current is preserved, the height of the STM tip follows a path shown in Figure 7.3. We can identify 3 distinct voltage ranges: the tunneling mode at high magnitude bias characterized by a tunnel junction between the STM tip and the complete heterostructure (b), the point contact mode at intermediate bias magnitude where the STM tip makes direct contact with the Alq_3 film (c), and the low bias mode where the voltage is not sufficient to access the electronic states of the Alq_3, and the tip is positioned to establish direct contact with the LCMO film (d). The 3 distinct voltage ranges are common across films of varying Alq_3 thicknesses, including when an evaporatively deposited Au film is substituted for LCMO. The tip height at the transition from the point contact mode (c) to contact with LCMO (d) corresponds to the film thickness, as calculated from the deposition rate. The height of the tip, Z, in point contact with the Alq_3 film also shows a dependence of $Z \propto (V\text{-}Vo)$, where Vo is the energy difference between the LUMO and the HOMO and the LCMO work function, depending on the polarity of the bias voltage. The constant of proportionality is related to the resistance of the conduction cell through the Alq_3 layer, and is further discussed in Section 7.3. The tip height vs voltage slope in the point contact mode is consistent across films of differing thickness grown under the same conditions, and appears to be a common property of the organic semiconductor film under similar growth conditions.

7.3 Band Alignment and Mobility Measurements

The resulting tip height (Z) vs bias voltage (V) measurements for a 10 nm thick Alq_3 layer, a 5 nm thick layer, and a bare LCMO film for positive and negative bias voltages are shown in Figure 7.4((a) and 7.4(b), respectively. The two polarities were measured in separate scans. All measurements

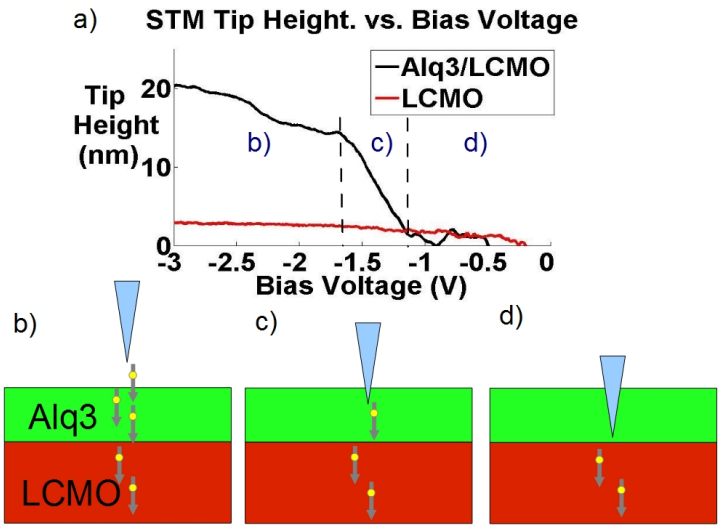

Figure 7.3: (a) Bias voltage vs tip heights measurements for a 10 nm Alq_3/LCMO heterostructure. Decreasing the magnitude of the bias voltage reveals three ranges, labeled (b), (c) and (d), with the resulting tip position in comparison with the heterostructure depicted in the corresponding section of the figure. (b) At high bias, a tunnel junction is established between the organic semiconducting film and tip. (c) At intermediate bias, the STM shifts to make point contact with the organic semiconductor. (d) At low bias voltage, within the Alq_3 bandgap, the tip is electronically insensitive to the organic semiconductor, and establishes direct contact with the underlying LCMO film.

presented were conducted on films grown with an annealed LCMO film, as similar scans on films deposited on unannealed LCMO were not reproducible, and it is believed the heated substrate increased the mobility of the resulting organic films to a level sufficient for the measurement. The measured bandgap for the 10 nm sample is 2.7 eV, consistent with values previously reported [30]. We can also note that the bias voltage marking the crossover between direct contact of the STM tip with the OSE and direct contact of the tip with the LCMO during the scan should be related to the offset of the LCMO work function and Alq_3 HOMO or LUMO, depending on the polarity of the bias voltage. In this respect, the bias voltages associated with the onset of conduction for both holes and electrons are consistent with a -0.3 eV offset for the Alq_3 LUMO and HOMO from the earlier energy level diagram. It is notable that measurements show the lack of either hole or electron type polaron states in the Alq_3 film, implying their unimportance in the organic semiconductor in this heterostructure, and also the lack of band bending between the LCMO and Alq_3 films. In contrast to the 10 nm sample, the 5 nm Alq_3 heterostructure shows the bandgap reduction from 2.7 to 2.4 eV,

the change primarily associated with the onset of hole injection. Curioni et al. analyzed Alq_3 using density functional theory and reported that facial vs. meridinal isomers show a difference in HOMO-LUMO gap magnitude of 2.4 to 2.7 eV [87]. Strain in the 5 nm film due to the closer proximity to the underlying LCMO may lead the Alq_3 facial isomer to be more energetically favorable, leading to the observed band structure. Similar V vs. Z measurements performed on a 20 nm thick Alq_3 layer were not reproducible regardless of the initial bias voltage. These results suggest that a proper tunneling junction cannot be established through a heterostructure with a Alq_3 top layer of 20 nm thickness, implying that the ballistic electron length through Alq_3 is between 10 and 20 nm. Further experiments with intermediate thickness will be necessary to confirm this finding.

To quantify the film mobility, we inspect the slope of the tip height in the contact mode. The slope is consistent across films of differing thicknesses, and the linear V vs Z dependence signifies a constant resistivity of the Alq_3 film, which allows an order of magnitude estimation of the carrier mobility μ for both holes and electrons. The mobility is calculated by $\mu = (IL)/(VqnA)$, with I = 20 pA, V the total voltage drop across the film (0.5 volts for 10 nm film at negative energies, for example), n the charge density of $1.5/nm^3$ (on the order of the Alq_3 molecular density), L the film thickness, and A the area of the conduction cell through the Alq_3 film. We estimate a range of values for A. The upper bound is calculated by the cross section of the STM tip embedded in the Alq_3 when the STM tip is in direct contact with the LCMO film, resulting in A $\sim\pi(10\text{ nm})^2$ for an average tip radius $\sim$10 nm. The lower bound given is estimated as a square cell, with side length the same as the

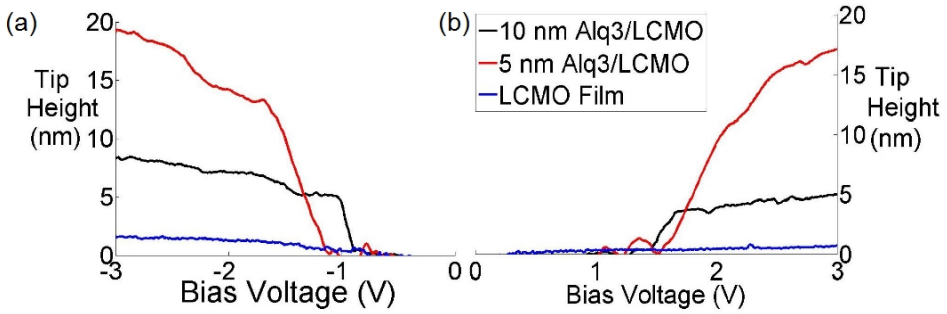

Figure 7.4: Tip height vs bias voltage measurements for a 10 nm thick Alq_3 layer on LCMO, a 5 nm layer, and a bare LCMO film for both positive (a) and negative bias (b) voltages, illustrating the reduction in bandgap with decreasing film thickness. The two polarities were measured in separate scans.

Table 7.1:

Technique	Electron Mobility (cm^2/Vs)	Hole Mobility (cm^2/Vs)
STM Measurement	8×10^{-5} to 7×10^{-6}	8×10^{-5} to 7×10^{-6}
Time of Flight [86]	1.4×10^{-6}	2×10^{-8}
Bulk LEDs [26][88]	10^{-12}–10^{-15}	-
Muon Spin Relaxation [28]	1.2×10^{-5}	-

lateral wavelength of the observed height modulations in the STM topographic image, or A $\sim(5\text{ nm})^2$, where we have conjectured that the lateral dimension of the topographic modulations are consistent with the grain size of the Alq_3 film. The resulting calculated mobilities for holes and electrons are both comparable, and in the range of 8×10^{-5} to 7×10^{-6} $cm^2(Vs)^{-1}$ in Alq_3. The measured mobility values for Alq_3 by STM more closely resemble values from muon spin relaxation than time of flight measurements or those calculated from transport in bulk LEDs taken from literature (Table 7.1). Possible reasons for the discrepancy are muon spin relaxation measurements make instrinsic estimations of the electron mobility from interchain diffusion constants, while time of flight and bulk structuces measure values from bulk structures dominated by the pinholes and interfaces issues discussed earlier. The increase in film mobility observed to a value on the same order of magnitude as the intrinsic limit with heated substrate during deposition suggests the presence of a beneficial crystalline orientation increasing conductivity of the film, with implications for device efficiency.

In conclusion, we have successfully deposited and investigated Alq_3/LCMO heterostructures of varying thicknesses to investigate charge transport in Alq_3. Bulk Alq_3 structural properties are preserved down to 10 nm in thickness with a -0.3 eV offset in band energies and a lack of band bending between LCMO and Alq_3 suggesting a shift in preferred isomer from meridinial to facial at the interface. The absence of polaron states from our STM measurements implies the unimportance of polarons in Alq_3 for this type of heterostructure. In addition, the measured mobilities on the order of 10^{-5} $cm^2(Vs)^{-1}$ for electrons and holes more closely resemble values of intrinsic mobility estimated from muon spin relaxation than those from bulk LED structures, which suggest that superior film conductivity close to the fundamental limit is possible with a heated substrate during sublimation.

Chapter 8

Conclusion

We have used spin polarized (SP) and non-polarized scanning tunneling microscopy (STM) to study spin and charge transport in the manganite $La_{0.7}Ca_{0.3}MnO_3$ (LCMO) and organic semiconductor Alq_3. STM SP-STM studies of LCMO reveal electronic inhomogeneity on the order of a couple hundred nanometer in size, which decreases above the Curie temperature T_c and with applied magnetic field. This finding gives a practical limit of one hundred nanometers in linear dimension for any reproducible and consistent devices employing LCMO in the ferromagnetic state without a stabilizing magnetic field. Using SP-STM, we observe results in agreement with a spin valve configuration between the magnetic STM tip and ferromagnetic LCMO, as determined by modeling of tunnel conductance between STM tip and LCMO film as a function of their relative magnetic orientation. We also observed the presence of a low energy gap at two distinctive energies; one at $\sim$ 0.4 eV in energy which is almost temperature indepedent and remains above T_c in the absence of magnetic field but disappears at low temperatures upon the application of a moderate magnetic field, while the second at $\sim$ 0.6 eV disappears above T_c. The former gap is consistent with a psuedogap predicted for the manganites in regions with phase separation [61] or magnetic cluster formation, as corroborated by its presence both above and below T_c in the absence of magnetic field, and by its disappearance under finite magnetic fields that lead to increasing mobility and spatial homogeneity in the manganites. The second gap is favored over the first with application of a magnetic field, and is attributed to a surface ferromagnetic insulating phase due to surface Ca deficiency based on evidences of the spin-filtering effect. This ferromagnetic insulator phase has potential for application

as a spin filter due to the differing gap value for spin majority and spin minority electrons.

We also conduct non-polarized STM studies of Alq_3/LCMO heterostructures of varying Alq_3 film thickness up to 20 nm. Bulk Alq_3 structural properties are preserved down to 10 nm in thickness with a -0.3 eV offset in band energies, with a lack of band bending between LCMO and Alq_3. The finding suggests a shift in the preferred isomer from meridinial to facial below 10 nm Alq_3 thickness. The absence of polaron states in the STM studies implies the relative unimportance of polarons in Alq_3 for this type of heterostructure. In addition, the measured mobilities on the order of 10^{-5} $cm^2(Vs)^{-1}$ for electrons and holes in Al_3 films deposited on heated LCMO substrates more closely resemble values of intrinsic mobility estimated from muon spin relaxation than those from bulk LED structures, suggesting that superior film conductivity close to the fundamental limit is possible with a heated substrate during sublimation.

Future studies of LCMO can employ conductance maps of the same area under increasing temperature to directly investigate the conversion of the ferromagnetic insulator gap to psuedogap and the disappearance of electronic inhomogeneity above T_c. Similar measurements on LCMO at bulk doping $x < 0.3$ can determine if promixity to the ferromagnetic insulating bulk phases further stabilizes the ferromagnetic insulating gap, and similar measurements in the related manganite $La_{0.7}Sr_{0.3}MnO_3$ can determine if a ferromagnetic insulating surface phase is universal to the family of compounds.

Additional non-polarized measurements on Alq_3/LCMO heterostructure with Alq_3 thickness less than 10 nm will allow further characterization of the interfacial Alq_3 layer. Spectroscopic measurements may be possible in heterostructures at cryogenic temperatures to stabilize the organic semiconductor, allowing spin-polarized and non-polarized investigations similar to those measurements performed with SP-STM to characterize of spin transport in Alq_3 thin films.

Appendix A

Low Temperature UHV STM/NSOM Design

A.1 Motivation

To investigate the exotic behavior of oxide systems, such as the interplay between ferromagnetism and the competing orders of charge order and/or antiferromagnestism in manganites and high-temperature superconductivity in cuprates, with nanoscale spatial resolution requires an STM capable of operating at cryogenic temperatures to reach the correct region of the phase diagram, ultra high vacuum to prevent sample degredation, and large applied magnetic fields to alter the sample phase. However, such an STM has never incorporated optical probes to permit simultaneous spatially resolved measurements of optical and electronic sample behavior under the above conditions. For this reason, a portion of this thesis was dedicated to design and partial assembly of an STM meeting the above specification but also incorporating a pair of far-field polished fiber optic probes for spatially averaged photonic detection and alignment of tip to specific sections of samples, and a near-field independently positioned tapered optical fiber operated in conjuction with an STM tip to allow high sensitivity, spatially resolved photonic detection.

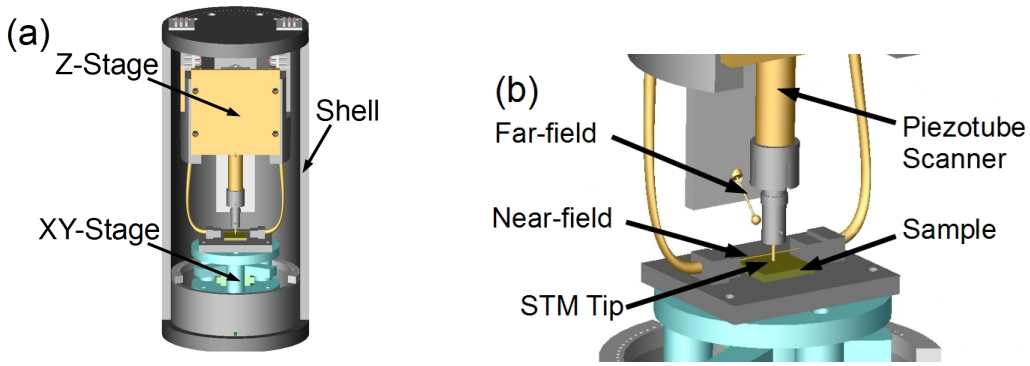

Figure A.1: (a) STM section design, consisting of a top section with STM z-stage coarse approach and bottom section with sample, xy-translation stage and optical probes mated by a cylindrical molybdenum shell. (b) Close up view of STM/NSOM, with piezotube scanner, STM tip, sample, and near field and far field optical probes labeled.

A.2 Construction and Design

A.2.1 STM Section

The STM section itself is divided seperated into two halves joined by a cylindrical shell (Figure A.1 (a)). The overall design of the STM components mimics Ching-tzu Chen's previous STM [43], discussed in Chapter 2, and uses piezoelectric stacks (piezostacks) in contact with a sapphire crystal driven in a stick/slip fashion to coarsely translate the STM into and out of tunneling range, and a piezoelectric tube (piezotube) to control tip rastering and height. The top section contains the tip, the coarse approach z-stage for translating the sample into and out of tunneling range and the piezoelectric tube scanner for fine control of the STM tip. The bottom section includes the sample holder, xy-translation stage to shift the sample position with respect to the STM tip, and far-field and near-field optical probes for imaging and photon detection (Figure A.1(b)). Roughly 95% of the machining of the STM head was performed by me, with greatly appreciated assistance from Nils Asplund for construction of the sample transfer stage.

Figure A.1 (a) shows a 3D rendering of the STM head. The materials used in construction of the head were molybdenum, Shapal©, an aluminum nitride ceramic, sapphire, and lead zirconate titanite, a piezoceramic material. All materials were chosen for their low outgassing and non-magnetic behavior, and similar coefficient of thermal expansion in the range of $\sim 5 \times 10^{-6}$ ppm to minimize

thermal drift. The main z-stage coarse approach body, sample holder, and shell surrounding the STM head were machined from molybdenum, chosen for its durability and high thermal conductivity. Shapal© was used as an insulating spacer for high voltage connections to the piezo stacks, and exhibits high thermal conductivity for a ceramic material ($\sim$ 100 W/m·K at room temperature) while retaining high machineablility. The piezostacks controling the coarse z approach of the STM stage, the xy-translation of the sample are composed of lead zirconate titanate (EBL #2, EBL Products Inc., 91 Prestige Park Circle, East Hartford, CT 06108), as is the piezotube controlling fine xyz control of the STM tip. One alteration from the previous design is a switch to a 0.200" diameter piezotube for superior durability. The total translation range in the z-direction is $\sim$3 cm, while in the xy-direction the sample can travel +/- 1 cm. Fine x,y, and z control of the tip is controlled by a piezo tube attached to an STM tip holder, with +/- 53 μm range in the xy- direction and +/- 13 μm range in the z- at 300K.

A.2.2 NSOM Probes

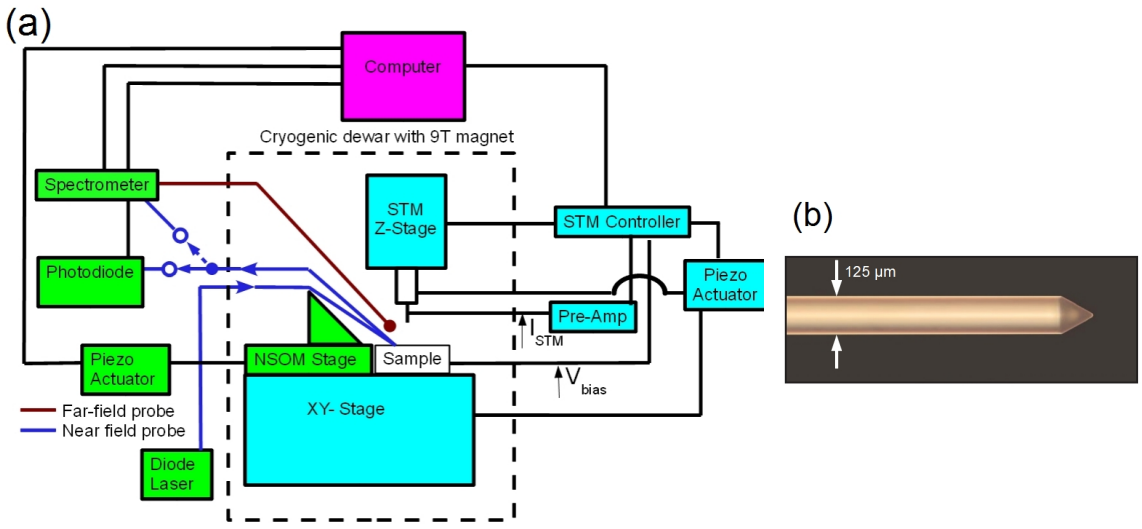

Figure A.2: (a) NSOM Block Diagram, highlighting components necessary for far field optical probe, NSOM, and STM. (b) Image of polished 125 μm diameter optical fiber [89].

Proxiamate to the sample holder are the indepedent far field polished optical fiber lenses and near field tapered optical fiber probe. The two far field probes consists of a 125 μm diameter

optical fiber with a polished lense to concentrate light into the fiber, purchased from Oz Optics (219 Westbrook Road, Ottawa, Ontario, Canada). The probe are mounted in a plate which extends from the STM head. Two such probes are paired to serve as an imaging system for the STM tip, sample, and near field probe. In this application, one tapered lense is optically coupled to a HeNe laser (HRR015, Thor Labs) located outside the UHV system and serves to illuminate the STM stage, with the second probe collects the reflected light and tranmits to a CCD camera (DCU224M, Thor Labs) for imaging. In addition, the far-field probe allows for detections of the total quantity of electroluminscient light generated by electron and hole recombination from the STM tunneling current if the magnitude is sufficiently strong. This light can be coupled to a photodiode (PDA8GS, Thor Labs) for overall intensity measurement, or to a spectrometer (CCS100) to identify the spectral weight verus wavelength of the light generated.

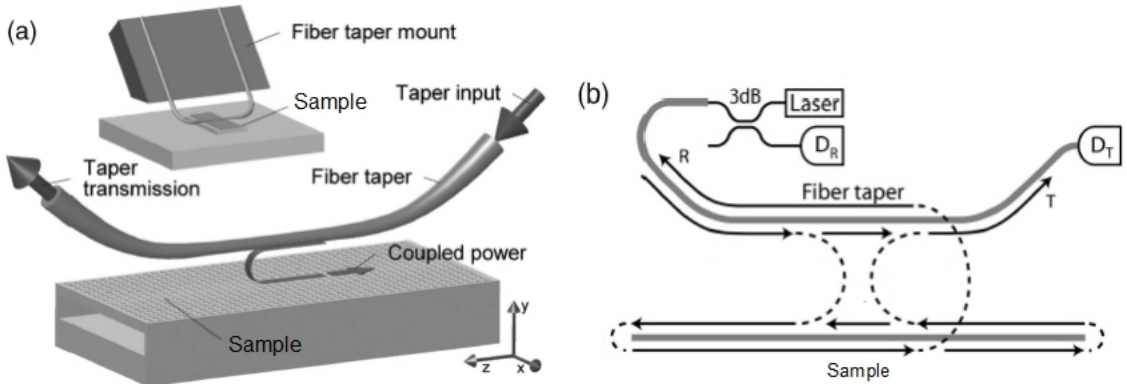

Figure A.3: (a) NSOM probe components. (b) NSOM coupling diagram. Figures adapted with permission from Barclay et al. [90]

The near field optical fiber taper is a method for highly efficient power transfer between the optical probe and sample optical structure with tunability of the coupling strength and phase matching frequency recently developed by Professor Oskar Painter's group at Caltech [90]. It consists of a single mode fiber heated and streched until it reaches a minimum of 1 μm, and brought close enough to an optically active structure to allow interaction by the evanescent tail of the fiber's fundamental mode with the structure(Figure A.3 (b)). Operated in this mode, the maximum range for evanescent coupling is on the order of approximately 1 μm [90], requiring precision placement of the tapered fiber to couple to a structure but in turn giving spatially resolved optical data with a $\sim$50 nm

resolution. In practice, a tunable frequency laser (ECL5000DT, Thor Labs) is coupled into the tapered fiber, along with photodiode at the input and output to measure reflected and transmitted light intensity respectively and thereby determine the energy transmitted to the sample structure (Figure A.3 (b)). The system can also be operated without the pump laser to detect photons emitted from the tip/sample junction. The fiber is attached to a sapphire fiber mount, sitting on Attocube ANPx51/LT/UHV and ANPz51/LT/UHV low temperature piezoelectric translation stages to control the horizontial and vertical distance of the tapered fiber from the STM/sample tunnel junction. If brought within range of the tip and sample, the tapered fiber and STM can be operated together with one tool as the pump and the alternate as the probe. If the tapered fiber is coupled to the input laser, the STM can be used in spectroscopic mode to investigate alterations in the sample DOS due to the optical pumping from the fiber, while the STM tunneling current can induce electroluminescience detectable by the tapered fiber.

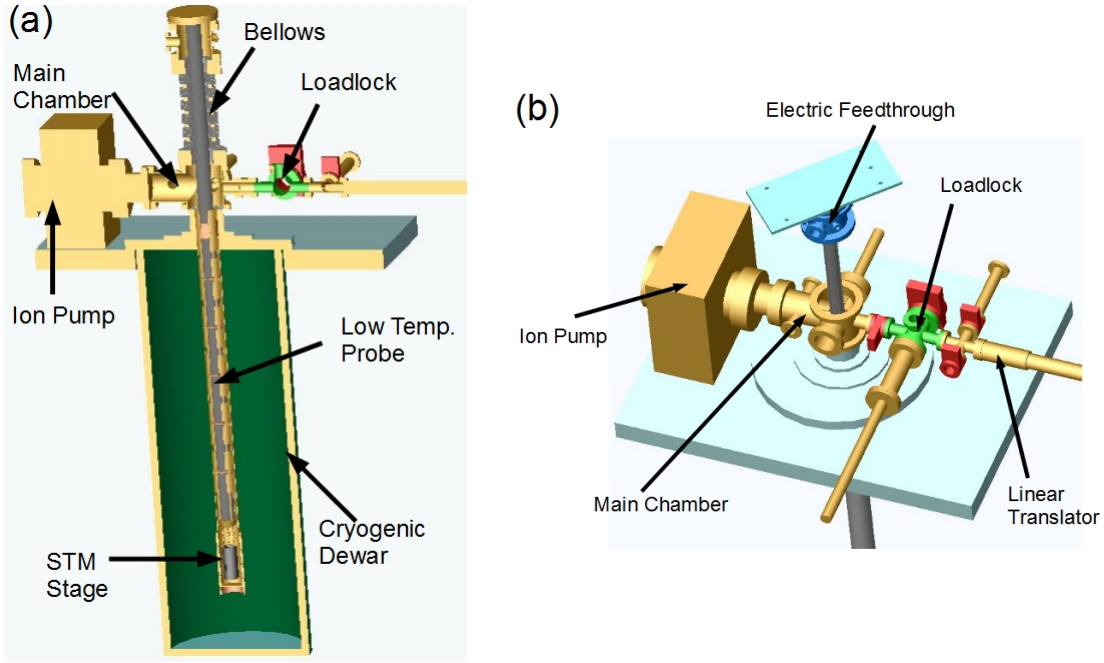

Figure A.4: STM UHV Chamber and cryogenic dewar, with STM in measurement position. (a) Cutaway view (b) Angled view (bellows omitted for clarity).

A.2.3 UHV System and Cryogenic Dewar

The design for the STM stage encloses it in a UHV system on a liquid helium dewar with superconducting magnet, as depicted in Figure A.4 (a) and (b). The UHV system is designed to keep the STM in ultra high vacuum pressure during loading of new tips, samples, or at cryogenic temperature operation. The STM stage is suspended from a stainless steel probe section, welded to a top plate attached to the a customed design bellows (Metal Flex Welded Bellows Inc., 149 Lakemont Road, Newport, VT 05855) with 60" of travel range. The bellows can extend or compress to allow adjustment of the STM stage height depending on the stage of experiment; the STM stage can be located at the height level of the center of the main chamber to allow transfer of sample or of tips, and subsequently moved into the dewar for low temperature or magnetic field measurements. The main UHV chamber is attached on the bottom port to a jacket which extends into the 9 tesla 4" bore superconducting magnet in the helium dewar, while the top port is attached to the bellows. The top flange of the probe is attached to a feedthrough chamber with connections for the probe's electrical wiring and optical fibers to exit the UHV system to the optics and control electronics. When operated, the system will require a similar set of preamplifier, STM controller, STM piezo motor, and computer discussed in Chapter 2. Separated from the main chamber by a gate valve is the loadlock system, which incorporates an additional gate valve to ambient atmosphere for loading, vacuum connection to a turbomolecular pump, and a linear translator with a spring loaded attachment to transport the sample holder onto and off of the STM stage. Vacuum is maintained in the system by a turbomolecular pump backed by a mechanical pump (not shown) connected to the loadlock and main chamber, and a Perkin-Elmer 220 L ion pump attached to the main chamber.

The STM stage is suspended from a copper cone on the bottom of the probe section by three 0.0254" diameter BeCu wire extension springs to vibrationally isolate the stage from UHV chamber and cryogenic dewar (Figure A.5). The copper cone comes into contact with a low temperature copper countercone welded to the jacket in the dewar to minimize pendulum motions from an extended probe, and to increase the cooling provided by the cryogenic liquid surrounding the jacket. The wiring and fiber optics are heat sunk at the copper cone to minimize heat delievered to the STM

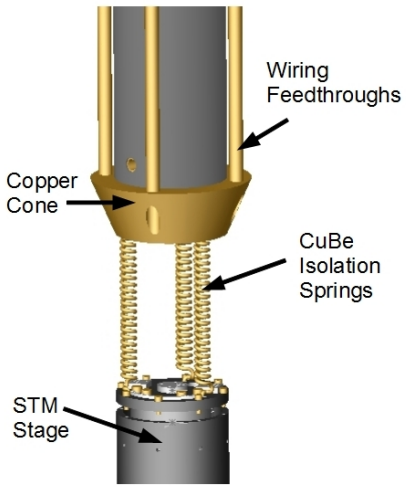

Figure A.5: STM heatsink stage, with copper cone and wiring feedthroughs.

by room temperature connections at the feedthrough chamber. Manganin wires are used from the heat sink stage to the feedthrough chamber to minimize heat transported from room temperature connections. Along the length of the probe are a series of baffles to shield the low temperature section from room temperature radiation, and a number of CuBe leaf springs to increase contact with the cold jacket walls.

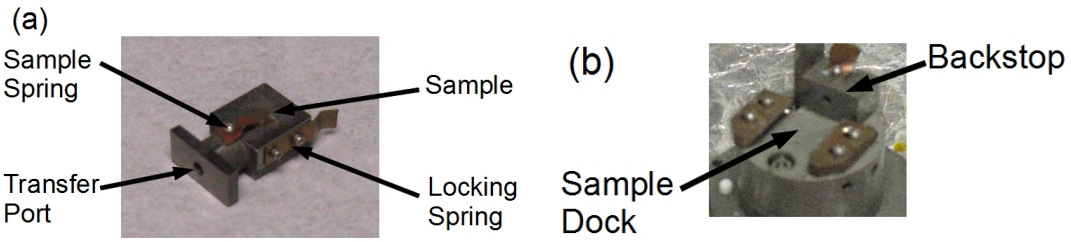

Figure A.6: (a) STM sample holder. (b) STM sample dock with the STM head.

Sample swapping in vacuum is acheived by a removable sample stage (Figure A.6 (a)). The sample is fixed onto the stage by a CuBe leaf spring (sample spring) in the loadlock chamber, with the sample stage attached to the STM stage mate on the linear translator by the transfer port (Figure A.7). The gate valve to outside atmosphere is closed, vacuum is established in the loadlock chamber, and the gate value to the main chamber is opened. The sample stage is moved toward the sample dock in the STM head (Figure A.6 (b)). The sample holder slides into the dock until it

reaches the backstop, and is held in place by an additional CuBe spring (locking spring), allowing the the sample stage mate on the linear translator to twist off and return to the loadlock chamber. The gate valve between loadlock and main chamber is closed, and the STM can translate down into the dewar for low temperature measurements.

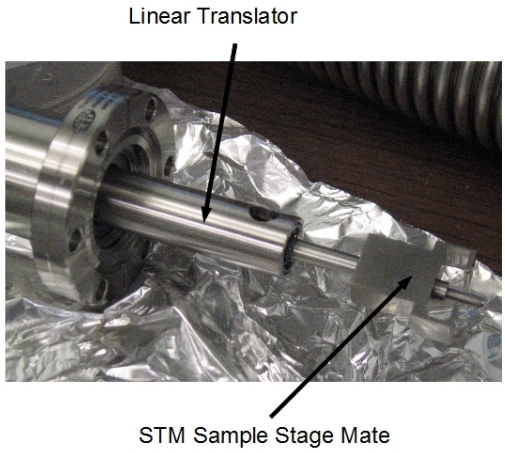

Figure A.7: STM sample holder mate attached to linear translator.

Further vibration isolation of the STM is accomplished by mounting the UHV system and dewar on a 3" aluminum plate, supported by 4 pneumatic vibration isolation legs to isolate the system from building vibrations. Additional lead shot will be added to the plate to increase the mass and decrease the resonant frequency of the system. The entire system will be installed in a room lined with sound absorbing foam.

A.2.4 Current Progress

The current progress in construction of the system at the time of writing is completion of the STM head with z approach stage, implementing the in-chamber vibration isolation system, and mounting in the UHV system. Future works will involve installing the xy-translation stage, mounting the system on the cryogenic dewar, installing far-field and NSOM optic probes, and constructing the low temperature probe for vertical translation of the STM head.

Bibliography

[1] G. E. Moore, Electronics **38**, 8 (1965).

[2] . IBM Research demonstrates path for extending current chip-making technique, IBM Research Press Release (Februrary 20th (2006).

[3] J. Hutchby, G. Bourianoff, V. Zhirnov, and J. Brewer, Circuits and Devices Magazine, IEEE **18**, 28 (2002).

[4] T. Dietl, H. Ohno, F. Matsukura, J. Cibert, and D. Ferrand, Science **287**, 1019 (2000).

[5] W. E. Pickett and D. J. Singh, Physical Review B **53**, 1146 (1996).

[6] G. Jonker and J. Van Santen, Physica **16**, 337 (1950).

[7] S. Jin, T. H. Tiefel, M. McCormack, R. A. Fastnacht, R. Ramesh, and L. H. Chen, Science **264**, 413 (1994).

[8] S. Satpathy, Z. S. Popović, and F. R. Vukajlović, Physical Review Letters **76**, 960 (1996).

[9] J. Park, E. Vescovo, H. Kim, C. Kwon, R. Ramesh, and T. Venkatesan, Nature **392**, 794 (1998).

[10] J. Soulen, R. J., J. M. Byers, M. S. Osofsky, B. Nadgorny, T. Ambrose, S. F. Cheng, P. R. Broussard, C. T. Tanaka, J. Nowak, J. S. Moodera, et al., Science **282**, 85 (1998).

[11] J. Y. T. Wei, N.-C. Yeh, and R. P. Vasquez, Physical Review Letters **79**, 5150 (1997).

[12] E. Dagotto, T. Hotta, and A. Moreo, Physics Reports **344**, 1 (2001).

[13] W. Prellier, P. Lecoeur, and B. Mercey, Journal of Physics: Condensed Matter **13**, R915 (2001).

[14] J.-H. Kim, A. M. Grishin, and V. A. Ignatova, Journal of Electronic Materials **37**, 361 (2008).

[15] C. Aruta, G. Ghiringhelli, V. Bisogni, L. Braicovich, N. B. Brookes, A. Tebano, and G. Balestrino, Physical Review B (Condensed Matter and Materials Physics) **80**, 014431 (pages 8) (2009).

[16] C. H. Chen and S.-W. Cheong, Physical Review Letters **76**, 4042 (1996).

[17] P. A. Algarabel, J. M. De Teresa, J. Blasco, M. R. Ibarra, C. Kapusta, M. Sikora, D. Zajac, P. C. Riedi, and C. Ritter, Physical Review B **67**, 134402 (2003).

[18] J. DeTeresa, M. Ibarra, P. Algarabel, C. Ritter, C. Marquina, J. Blasco, J. Garcia, A. delMoral, and Z. Arnold, Nature **386**, 256 (1997).

[19] G. Papavassiliou, M. Fardis, M. Belesi, T. G. Maris, G. Kallias, M. Pissas, D. Niarchos, C. Dimitropoulos, and J. Dolinsek, Physical Review Letters **84**, 761 (2000).

[20] M. Fä;th, S. Freisem, A. A. Menovsky, Y. Tomioka, J. Aarts, and J. A. Mydosh, Science **285**, 1540 (1999).

[21] V. I. Krinichnyi, Synthetic Metals **108**, 173 (2000), ISSN 0379-6779.

[22] Z. Xiong, D. Wu, Z. Vardeny, and J. Shi, Nature **427**, 821 (2004).

[23] C. K. Chiang, C. R. Fincher, Y. W. Park, A. J. Heeger, H. Shirakawa, E. J. Louis, S. C. Gau, and A. G. MacDiarmid, Physical Review Letters **39**, 1098 (1977).

[24] M. Pope, H. P. Kallmann, and P. Magnante, The Journal of Chemical Physics **38**, 2042 (1963).

[25] O. . . Sony Launches World's First *1 OLED TV, Sony Corporation Press Release (????).

[26] C. W. Tang and S. A. VanSlyke, Applied Physics Letters **51**, 913 (1987).

[27] E. Arisi, I. Bergenti, V. Dediu, M. A. Loi, M. Muccini, M. Murgia, G. Ruani, C. Taliani, and R. Zamboni, Journal of Applied Physics **93**, 7682 (2003).

[28] A. J. Drew, F. L. Pratt, J. Hoppler, L. Schulz, V. Malik-Kumar, N. A. Morley, P. Desai, P. Shakya, T. Kreouzis, W. P. Gillin, et al., Physical Review Letters **100**, 116601 (pages 4) (2008).

[29] L. Ke, S. J. Chua, R. C. C. Han, L. T. Ting, and C. Vijila, Journal of Applied Physics **99**, 114512 (pages 4) (2006).

[30] P. E. Burrows, S. R. Forrest, S. P. Sibley, and M. E. Thompson, Applied Physics Letters **69**, 2959 (1996).

[31] X. H. a. T. W. A. Uddin, C.B. Lee, Applied Physics A: Materials Science and Processing **78**, 401 (2004).

[32] G. Binnig, H. Rohrer, C. Gerber, and E. Weibel, Applied Physics Letters **40**, 178 (1982).

[33] I. Giaever and K. Megerle, Phys. Rev. **122**, 1101 (1961).

[34] R. Wiesandanger, *Scanning Probe Microscopy and Spectroscopy: Methods and Applications Scanning Probe Microscopy and Spectroscopy: Methods and Applications* (Cambridge, Cambridge University Press, 1994).

[35] R. M. Feenstra and J. A. Stroscio, Physica Scripta **T19A**, 55 (1987).

[36] F. Meier, L. Zhou, J. Wiebe, and R. Wiesendanger, Science **320**, 82 (2008).

[37] T. Kawagoe, Y. Iguchi, T. Miyamachi, A. Yamasaki, and S. Suga, Physical Review Letters **95**, 207205 (2005).

[38] W. J. Grande, J. E. Johnson, and C. L. Tang, Journal of Vacuum Science Technology B: Microelectronics and Nanometer Structures **8**, 1075 (1990).

[39] R. Wiesendanger, I. V. Shvets, D. Bürgler, G. Tarrach, H. J. Güntherodt, J. M. D. Coey, and S. Gräser, Science **255**, 583 (1992).

[40] R. Wiesendanger, H. J. Güntherodt, G. Güntherodt, R. J. Gambino, and R. Ruf, Physical Review Letters **65**, 247 (1990).

[41] I. K. Song, M. S. Kaba, and M. A. Barteau, Langmuir **18**, 2358 (2002).

[42] N. Hirashita, G. Yokoyama, T. Kambara, and K. I. Gondaira, Journal of Physics F: Metal Physics **11**, 2371 (1981).

[43] C. T. Chen, *Scanning Tunneling Spectroscopy Studies of High-Temperature Cuprate Superconductors*, Ph. D. Dissertation, California Institute of Technology (2006).

[44] A. D. Beyer, *Studies of the low-energy quasiparticle excitations in high temperature superconducting cuprates using scanning tunneling microscopy and magnetization measurements*, Ph. D. Dissertation, California Institute of Technology (2009).

[45] M. Bode, Reports on Progress in Physics **66**, 523 (2003).

[46] P. R. Willmott and J. R. Huber, Rev. Mod. Phys. **72**, 315 (2000).

[47] S. Seiro, Y. Fasano, I. Maggio-Aprile, E. Koller, O. Kuffer, and O. Fischer, Physical Review B (Condensed Matter and Materials Physics) **77**, 020407 (pages 4) (2008).

[48] J. Mitra, M. Paranjape, A. K. Raychaudhuri, N. D. Mathur, and M. G. Blamire, Physical Review B (Condensed Matter and Materials Physics) **71**, 094426 (pages 8) (2005).

[49] I. K. Robinson and D. J. Tweet, Reports on Progress in Physics **55**, 599 (1992).

[50] M. McElfresh, *Fundamentals of Magnetism and Magnetic Measurements*, San Diego, Quantum Design (1994).

[51] F. J. Giessibl, Rev. Mod. Phys. **75**, 949 (2003).

[52] C. Zener, Phys. Rev. **81**, 440 (1951).

[53] A. J. Millis, P. B. Littlewood, and B. I. Shraiman, Physical Review Letters **74**, 5144 (1995).

[54] M. J. Calderón, J. A. Vergés, and L. Brey, Physical Review B **59**, 4170 (1999).

[55] N. Furukawa, Journal of the Physical Society of Japan **63**, 3214 (1994).

[56] S. Yunoki, J. Hu, A. L. Malvezzi, A. Moreo, N. Furukawa, and E. Dagotto, Physical Review Letters **80**, 845 (1998).

[57] D. W. Reagor, S. Y. Lee, Y. Li, and Q. X. Jia, Journal of Applied Physics **95**, 7971 (2004).

[58] J. Y. T. Wei, N.-C. Yeh, R. P. Vasquez, and A. Gupta, The 7th joint MMM-intermag conference on magnetism and magnetic materials **83**, 7366 (1998).

[59] Z. Fang and K. Terakura, Journal of the Physical Society of Japan **70**, 3356 (2001).

[60] P. R. Broussard, S. B. Qadri, V. M. Browning, and V. C. Cestone, Applied Surface Science **115**, 80 (1997), ISSN 0169-4332.

[61] A. Moreo, S. Yunoki, and E. Dagotto, Physical Review Letters **83**, 2773 (1999).

[62] A. Moreo, M. Mayr, A. Feiguin, S. Yunoki, and E. Dagotto, Physical Review Letters **84**, 5568 (2000).

[63] R. P. Vasquez, Physical Review B **54**, 14938 (1996).

[64] S. A. Wolf, D. D. Awschalom, R. A. Buhrman, J. M. Daughton, S. von Molnar, M. L. Roukes, A. Y. Chtchelkanova, and D. M. Treger, Science **294**, 1488 (2001).

[65] J. A. Gupta, R. Knobel, N. Samarth, and D. D. Awschalom, Science **292**, 2458 (2001).

[66] R. Kusters, J. Singleton, D. Keen, R. McGreevy, and W. Hayes, Physica B: Condensed Matter **155**, 362 (1989), ISSN 0921-4526.

[67] R. von Helmolt, J. Wecker, B. Holzapfel, L. Schultz, and K. Samwer, Physical Review Letters **71**, 2331 (1993).

[68] G. C. Xiong, Q. Li, H. L. Ju, S. N. Mao, L. Senapati, X. X. Xi, R. L. Greene, and T. Venkatesan, Applied Physics Letters **66**, 1427 (1995).

[69] A. P. Ramirez, Journal of Physics: Condensed Matter **9**, 8171 (1997).

[70] V. M. Coey, J. M. D. and S. von Molnar, Advances in Physics **48**, 167 (1999).

[71] A. G. K. B.-G. S. Y.-A. C. S.-W. Renner, Ch., Nature **416**, 518 (2002).

[72] N.-C. Yeh, R. P. Vasquez, D. A. Beam, C.-C. Fu, J. Huynh, and G. Beach, Journal of Physics: Condensed Matter **9**, 3713 (1997).

[73] N.-C. Yeh, C.-C. Fu, J. Y. T. Wei, R. P. Vasquez, J. Huynh, S. M. Maurer, G. Beach, and D. A. Beam, The 41st annual conference on magnetism and magnetic materials **81**, 5499 (1997).

[74] D. S. Dessau, T. Saitoh, C.-H. Park, Z.-X. Shen, P. Villella, N. Hamada, Y. Moritomo, and Y. Tokura, Physical Review Letters **81**, 192 (1998).

[75] N.-C. Yeh and A. D. Beyer, International Journal of Modern Physics B **23**, 4543 (2009).

[76] M. Cölle and W. Brutting, Physica Status Solidi A-Applied Research **201**, 1095 (2004).

[77] A. Curioni, W. Andreoni, R. Treusch, F. J. Himpsel, E. Haskal, P. Seidler, C. Heske, S. Kakar, T. van Buuren, and L. J. Terminello, Applied Physics Letters **72**, 1575 (1998).

[78] M. Muccini, M. Brinkmann, G. Gadret, C. Taliani, N. Masciocchi, and A. Sironi, Synthetic Metals **122**, 31 (2001), ISSN 0379-6779, proceedings of the E-MRS 2000 Spring Meeting, Symposium I.

[79] Z.-A. Jian, Y.-Z. Luo, J.-M. Chung, S.-J. Tang, M.-C. Kuo, J.-L. Shen, K.-C. Chiu, C.-S. Yang, W.-C. Chou, C.-F. Dai, et al., Journal of Applied Physics **101**, 123708 (pages 6) (2007).

[80] A. J. Heeger, *Semiconducting and Metallic Polymers:The Fourth Generation of Polymeric Materials*, Nobel Lecture (2000).

[81] A. J. Heeger, S. Kivelson, J. R. Schrieffer, and W. P. Su, Rev. Mod. Phys. **60**, 781 (1988).

[82] J. Hirsch, Journal of Physics C: Solid State Physics **12**, 321 (1979).

[83] W. M.-H. H. M. Cölle, J. Gmeiner and W. Brtting, Advanced Functional Materials **13**, 108 (2003).

[84] S. F. Alvarado, P. F. Seidler, D. G. Lidzey, and D. D. C. Bradley, Physical Review Letters **81**, 1082 (1998).

[85] J.-Z. Wang, J. T. Sadowski, Z.-H. Xiong, Y. Fujikawa, Q. K. Xue, and T. Sakurai, Nanotechnology **20**, 095704 (2009).

[86] R. G. Kepler, P. M. Beeson, S. J. Jacobs, R. A. Anderson, M. B. Sinclair, V. S. Valencia, and P. A. Cahill, Applied Physics Letters **66**, 3618 (1995).

[87] A. Curioni, M. Boero, and W. Andreoni, Chemical Physics Letters **294**, 263 (1998), ISSN 0009-2614.

[88] C. Lee, A. Uddin, X. Hu, and T. Andersson, Materials Science and Engineering B **112**, 14 (2004), ISSN 0921-5107.

[89] *Tapered Fiber Catalog*, Oz Optics, 219 Westbrook Road, Ottawa, Ontario, Canada (2010).

[90] P. E. Barclay, K. Srinivasan, M. Borselli, and O. Painter, Opt. Lett. **29**, 697 (2004).